Experimental and numerical research into propeller thrust breakdown due to ventilation

Thesis Report

M. van der Leij

Technische Universiteit Delft

TU Delft

MARIN

Experimental and numerical research into propeller thrust breakdown due to ventilation

Thesis Report

by

M. van der Leij

Student number:	4297490	
Submission date:	June 12, 2019	
Thesis committee:	Prof. dr. ir. T. C. J. van Terwisga,	TU Delft & MARIN
	ir. L.J.G. Huijgens,	TU Delft
	dr.ir I. Akkerman,	TU Delft
	ir. B. Schuiling,	MARIN
	ing. G.H.J. Hagesteijn	MARIN

TU Delft MARIN

Abstract

When propellers are operating near the free surface, a phenomenon called ventilation might occur. Due to insufficient immersion and high thrust loading, the propeller draws air, resulting in a reduced thrust. Reduced thrust may have consequences such as loss of propulsive power, control and steerability, and may therefore be leading to safety issues. Long time exposure to ventilation's unsteady torque loading can also lead to propulsive unit malfunctioning. As propeller diameters tend to grow bigger to increase the efficiency, free surface clearance decreases and room is left for air to be drawn. To increase understanding of the phenomenon, the research question *"What is the influence of major parameters on thrust breakdown due to propeller ventilation and (how) can it be predicted?"* was set.

Experimental and numerical research were conducted to answer the question. The used propeller was a Wageningen C4.55-propeller, an in design condition lightly-loaded propeller with low blade area, fitting to the trend of increasing diameters. The research was bound by perfect conditions to capture ventilation in the purest form; no influences of wake, waves and ship motions were taken into account. It is however expected that the obtained knowledge can be applied to more complex situations as well.

Ventilation is captured in three regimes. Close to the free surface, so-called free surface ventilation occurs. Inception takes place by breaking through the free surface and air is drawn due to direct contact with the atmosphere. More deeply immersed, vortex ventilation in found. In this regime, a ventilating vortex to the free surface is the source of air. Inbetween, mixed ventilation is found, where air provision is a combination of free surface breaking and ventilating vortices.

Experimental research showed that free surface ventilation appeared to be the most stable and predictable ventilation regime. Inception through free surface breaking mainly depends on the pressure gradient between the propeller tip and free surface (parametrized by the ventilation number σ_v, depending on thrust loading coefficient C_T and tip immersion h_{tip}), the tip immersion rate I and the ability to draw the free surface (parametrized by the Froude number Fr). Increased ventilation thrust breakdown showed to be influenced by the local velocity on the blade, which mainly depends on the propeller rotation rate N. Ventilation thrust breakdown is therefore captured depending on N. As only one propeller was studied, a conclusion on the influence of the pitch ratio was not yield, but an influence is expected. Immersion at which free surface ventilation occurs may be found in ballast conditions. Also ship motions and waves increase the likeliness of free surface ventilation. Vortex ventilation was the most unstable regime in the experiments. Inception seems to be independent of the propeller loading, but influenced by local flow phenomena in the area above the propeller, (such as low advance velocity in behind conditions found as a result of the ships wake and recirculation) and on propeller characteristics (such as the tip vortex strength and circulation around the blade of the propeller). Even more than $1D$ immersed, inception was found. It is believed that vortex inception, shape and wash-out resembles the appearance of the cavitating propeller-hull vortex. Vortex ventilation showed a bistability effect; inception and wash-out thrust loading appeared to be unequal. Thrust breakdown seems to be independent of the thrust loading and immersion depth. The regime inbetween, mixed ventilation, showed the largest variations in thrust breakdown and is therefore the most limiting ventilation regime w.r.t. propulsive unit breakdown. As mixed ventilation was only found for a small immersion bandwidth, it is expected not to be found continuously in ship application due to ship motions. On the other side, ship motions might resemble a state of mixed ventilation due to varying immersion.

Experimental results were obtained using a statistical research planning, such that polynomial models could be constructed. The propeller specific and generic model fitted the data well, demonstrated by the fitting coefficient r^2 exceeding 0.9. Structural shortcomings were however found in capturing the highly unsteady vortex ventilation, variations in mixed ventilation and increased thrust breakdown in free surface ventilating.

Numerically, ventilation was simulated using the MARINs in-house and open-usage, two-phase volume-of-fluid incompressible flow solver `ReFRESCO`. All three ventilation regimes were tested on their thrust breakdown prediction with different settings. The start-up procedure of B. Schuiling was applied to start the sim-

ulation efficiently and without early inception. L_∞-residuals were at most around 10^{-2}, except for the ω-equation and during the start-up procedure. Within one timestep, 100 outerloops were not sufficient for force and iterative convergence. In grid interface interpolation, strange behaviour was found, but it did not seem to harm the results. Timesteps corresponding to 0.5°propeller rotation increment and implicit second order backward timestepping were applied. All convective quantities were discretized using Van Leer's TVD limiter. ReFRICS [36] was used in the free surface equation, as it showed to be the least diffusive in preliminary tests.

Vortex ventilation inception was not found, even when a scale resolving simulation ($k-\omega TNT-XLES$ model of Kok et al. [41]) was conducted. This is ascribed to insufficient application of the $k-\omega TNT-XLES$ model in the near blade area, due to insufficient convergence of the ω-equation. Also application of Boussinesqs assumption in the k-equation, which leads to production of turbulence in regions of high velocity gradient such as the vortex core, might be stringent. Free surface ventilation inception was accurately found, both in simulations with a for ventilation adapted actuator disk model and with the propeller. For the propeller simulation, $k-\omega TNT$ turbulence model of Kok [40] was applied. Thrust breakdown was underestimated by CFD. Only breakdown due to surface piercing was found. Underestimation is ascribed to the absence of air entrainment. Application of the $TNT-EARSM$-model of Dol et al. [14] (which is not using Boussinesqs assumption) and application of free-slip boundary conditions did not improve the shortcoming. As in literature, other free surface discretization schemes showed the same lack of air engtrainment, the origin might be in the VoF-assumption, being the increased interpolated density used in the momentum equation which prevents air to be convected.

Acknowledgements

This work is the result of my graduation project. In this project, I tested and applied the abilities learned during my time the university and expanded my knowlegde in fluid dynamics, as well computational as experimental. I enjoyed working on this topic and improved in multiple areas. Several people and institutions needs to be thanked.

I would like to thank prof. dr. ir. Tom Van Terwisga, who first of all introduced me in the interesting topic of fluid dynamics and propellers and secondly gave me the opportunity to execute this thesis work at MARIN. I am indepted to the company for providing me the necessary and excessive computational resources and for the possibility to execute experiments. I also want to thank ir. Bart Schuiling, my daily supervisor who always and also unsolicitedly provided feedback to inprove my work and habits and who learned me around in CFD. His helpfullness and dedication in this project encouraged me to strive for the optimal result. Furthermore others at MARIN, a.o. Gerco Hagesteijn, Reint Dallinga, Joost Moulijn, Guilherme Vaz and many more, needs to be thanked for their collaboration and contribution to this ventilation research. A special acknowledgeneemt needs to go to Arno Bons, for saving me hours of travelling time and listening to "*Deutsche Donnerstag*".

Last but not least I want to thank friends and collegue-students, at MARIN and still in Delft for their interest in this project and random brainstorms about random topics. And of course I must thank my parents, who gave me a warm welcome back home during this thesis period and provided me the possibility to study.

Maarten van der Leij
June 2019

Contents

Nomenclature

Quanti1ties		
α	Scale factor	-
Γ	Vorticity	$1/s$
λ	Wave length	m
Φ	Value of any quantity in cell	–
$_f$	Full scale	s
$_m$	Model scale	s
F	Force	N, kgm/s^2
L	Length	m
m	Mass	kg
p	Pressure	N/m^2
p_0	Reference pressure	N/m^2
Q	Arbitrary quantity	-
t	Time	s
u	Velocity	m/s
V	Volume	m^3
Constants		
μ	Dynamic viscosity	$Pa \cdot s = kg/ms^2$
ν	Kinematic viscosity	m^2/s
ρ_w, ρ_a	Density of water, air	kg/m^3
σ	Surface tension coefficient of water to air	N/m
c_w, c_a	Speed of sound in water, air	m/s
g	Gravitational acceleration	m/s^2
Propeller		
A_e	Propeller expanded area	m^2
c	Chord length	m
D	Propeller diameter	m
h_{shaft}	Immersion of propeller defined according shaft immersion	m
h_{tip}	Immersion of propeller defined according tip clearance	m
N	Propeller revolution rate	$1/s$
P	Propeller pitch	m
Q	Torque	Nm
r	Propeller radius	m
T	Thrust	N
v_a	Inflow velocity	m/s
v_d	Velocity through propeller disk	m/s
Propeller Derived Quantities		
α	Angle of attack of propeller blade, $\theta - \beta$	rad
β	Hydrodynamic propeller pitch angle, $arctan\left(\frac{\pi nD}{v_a}\right)$	rad
β_Q	Torque breakdown ratio, $\frac{(k)Q}{(k)Q_0}$	-
β_T	Thrust breakdown ratio, $\frac{(k)T}{(k)T_0}$	-
$\hat{C_T}$	Thrust loading coefficient used in polynomial model	-

$\hat{Fr_{ND}}$	Froude number based on rotational velocity used in polynomial model	-
$\hat{I}$	Immersion rate used in polynomial model	-
$\hat{J}$	Advance ratio used in polynomial model	-
$\hat{N}$	Propeller revolution rate used in polynomial model	-
σ_v	Ventilation inception number	-
A, A_0	Propeller disk area, πr^2	m^2
C_T	Thrust loading coefficient, $\frac{T}{0.5\rho A v_a^2}$	-
$EAR, \frac{A_e}{A_0}$	Expanded area coefficient of propeller	-
Fr, Fr_{va}	Froude number based on inflow velocity, $\frac{v_a}{\sqrt{(gD}}$	-
Fr_{ND}	Froude number based on rotational velocity, $\frac{nD}{\sqrt{(gD}}$	-
I	Immersion rate, $\frac{h_{tip}}{D}$	-
J	Advance ratio, $\frac{v_a}{nD}$	-
K_Q	Non-dimensional torque coefficient, $\frac{Q}{\rho n^2 D^5}$	-
K_T	Non-dimensional thrust coefficient, $\frac{T}{\rho n^2 D^4}$	-
P/D	Pitch ratio of propeller	-
Re	Reynolds number, $\frac{\rho u L}{\mu}$	-
v_∞	Velocity at propeller blade, $\sqrt{v_a^2 + (\pi n D)^2}$	-
We	Weber number, $\frac{\rho L u^2}{\sigma}$	-
CFD		
α	Air-volume fraction	-
Δ	LES-filter width	m
$\frac{d}{dt}, \frac{D}{Dt}$	Time derivative, Material derivative	$1/s$
κ	Variable in second order flux discretisation	-
κ	Von Kárman constant	[-]
$\nabla, \nabla\cdot, \nabla x$	Gradient, Divergence and Curl operator	$1/m$
ν_t	Eddy viscosity	m^2/s
ω	Relaxation factor	-
ω	Turbulent dissipation	m^2/s^2
ϕ	Fit function in grid refinement study	-
ϕ	Limiter function in flux discretisation	-
ε	Error	-
ε	Turbulent dissipation rate	m^2/s^3
ASF	α-shape factor as used in ventilating actuator disk	-
C_1, C_2, β_k	Various constants in $k-\omega$ turbulence model	[-]
dt	Timestep	-
$h, \Delta x$	Grid cell size	m
k	Iteration number	-
k	Turbulent kinetic energy	m^2/s^2
L_∞, L_2	Norm of the error	-
N	Number of iterations	-
r	Ratio between upstream and downstream flux	-
r_i, d_i	Refinement and diffusion factor in grid i	-
U	Uncertainty	-
y^+	Non-dimensional first cell height	-

Acronyms

Acronym	Meaning
AFM	Absolute Formulation Method
BC	Boundary Condition
CDS	Central Differencing Scheme
CFD	Computational Fluid Dynamics
CFL	Courant-Friedrich-Levy
CPP	Controllable Pitch Propeller
DoE	Design of Experiments
DoF	Degree-of-Freedom
exp	experimental
(EA)RSM	(Explicit Algebraic) Reynolds Stress Model
EFD	Experimental Fluid Dynamics
FOU	First Order Upwind
HRIC	High Resolution Interface Capturing
(I(D))DES	(Improved (Delayed)) Detached Eddy Simulation
ITTC	International Towing Tank Conference
LES	Large Eddy Simulation
MARIN	MARitiem Instituut Nederland / Maritime Research Institute Netherlands
MRF	Multiple Reference Frame
MVG	Moving Grid
NTNU	Norwegian University of Science and Technology
num	numerical
OL	Outerloops
OWD	Open Water (Propeller) Diagram
QUICK	Quadratic Upstream Interpolation for Convective Kinematics
RaNS	Reynolds Averaged Navier-Stokes
ReFRESCO	Reliable and Fast RaNS-Equations (solver for) Ships and Constructions Offshore
SIMPLE	Semi Implicit Method for Pressure Linked Equations
SRS	Scale Resolving Simulation
TNT	Turbulent/Non-Turbulent
TV(D)	Total Variation (Diminishing)
UD	Upwind Differencing
Wag.B/C	Wageningen B/C-serie
VoF	Volume-of-Fluids
XLES	Extra Large Eddy Simulation

1 Introduction

The entrainment of atmospheric air in a low pressure zone is called ventilation. These low pressure zones exist on lifting foil sections such as sailboat dagger boards and propellers, which makes them prone to ventilation. During such an event, which mostly occur suddenly and unintentional, induced forces can decrease by 80% [6], leading to substantial safety risks; for example loss of steering capabilities or propulsive power. Furthermore, it is known that long term exposure to propeller ventilation can lead to malfunctioning of propulsive units due to ventilation's dynamic loading characteristic [6]. However, as propeller diameters tend to grow bigger, propeller clearance decreases and room is left for air to be drawn into the propeller plane, leading to higher chance of occurence.

1.1. Objective

The goal of this research is to increase the understanding of ventilation. First of all, important parameters, dimensionless quantities and relations are to be found, which can be used in an experimentally prediction of ventilation thrust breakdown. Furthermore, an assessment to what extent it is possible to numerically predict ventilation is of interest. These goals can be captured in the main research question:

"What is the influence of major parameters on thrust breakdown due to propeller ventilation and (how) can it be predicted?"

, which consists of three subquestions:

1. What are the major parameters in propeller ventilation and how do those parameters influence the inception and thrust breakdown?
2. To what extend is it possible to predict thrust breakdown experimentally?
3. To what extend is it possible to predict thrust breakdown numerically?

1.2. Scope and methodology

The ventilation phenomenon is complex and not fully understood. Ventilation is expected to be influenced by ship motions, waves, and local flow phenomena as dead water areas. However, to decrease complexity and to capture ventilation in its purest form, only ventilation in an open water set-up will be researched. It is expected that in an open water set-up, valuable results can be obtained which are also valid for ventilation in more restrictive set-ups.

Furthermore propeller characteristrics may be of influence. It is decided to use only one propeller from the Wageningen C-series. The Wageningen C-series are controllable pitch propellers (CPPs) with a modern blade design, designed to conduct experiments and add knowledge to off-design performance of CPPs. This is of interest as more and more vessels are being equipped with CPPs to coop with the off-design conditions they encounter [12]. Since increasing diameters and lower propeller loadings are expected to improve efficiency, it is decided to investigate the ventilation characteristics of a (in design operation) lightly-loaded propeller.

Table 1.1: Propeller section characteristics of Wag C4.55 P/D=0.8

r/R	c/D	P/D	s/D	Rake/D	f/D	t/D
0.249	0.136	0.676	-0.008	0.007	0.006	0.045
0.3	0.172	0.708	-0.017	0.008	0.009	0.031
0.35	0.207	0.735	-0.026	0.006	0.010	0.028
0.4	0.240	0.757	-0.033	0.003	0.010	0.026
0.5	0.299	0.789	-0.042	-0.005	0.011	0.021
0.6	0.344	0.803	-0.036	-0.013	0.010	0.016
0.7	0.368	0.800	-0.010	-0.018	0.009	0.012
0.8	0.361	0.779	0.041	-0.019	0.007	0.009
0.85	0.340	0.762	0.076	-0.017	0.006	0.008
0.9	0.302	0.741	0.119	-0.013	0.004	0.006
0.95	0.234	0.715	0.169	-0.007	0.002	0.005
0.975	0.174	0.701	0.196	-0.004	0.001	0.004
1	0.000	0.685	0.226	0.001	0.000	0.004

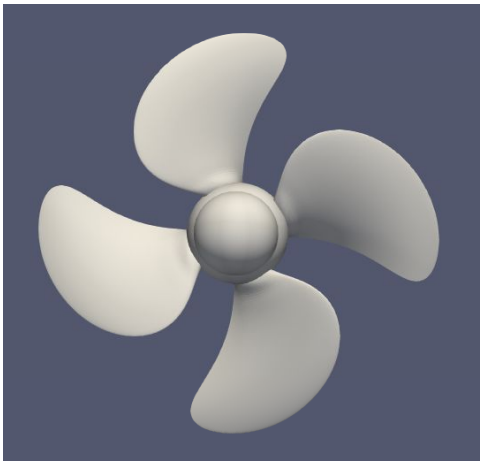

Figure 1.1: Wageningen C4.55 P/D=0.8

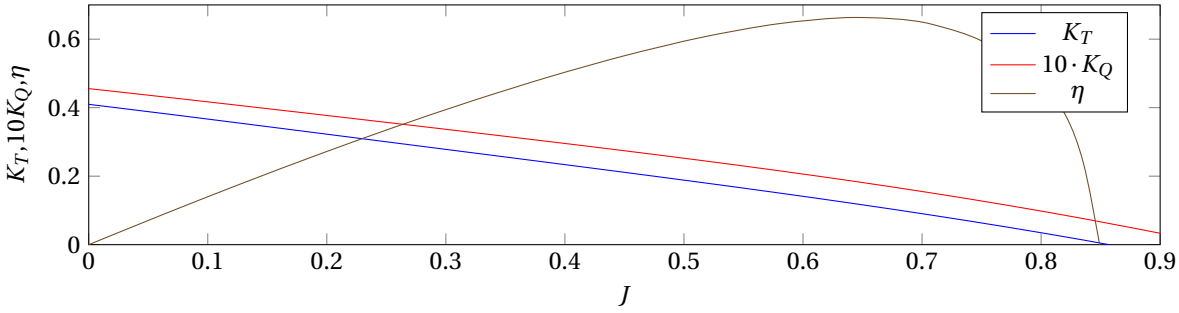

Figure 1.2: Open water diagram for Wageningen C4.55 propeller

Within the C-series, the C4.55 propeller is such a propeller, with a reduced expanded area, used in internal projects. The pitch ratio at $0.7R$ of the propeller is 0.8. The propeller diameter is 0.23294 m.
To answer the research (sub)questions, a literature study, computational and experimental fluid dynamics were applied. Goal and subquestion 1 is answered by the use of literature and application of (simplified) CFD and experiments. Literature is used in obtaining first knowlegde about the phenomenon, while CFD is used for the indication and derivation of important parameters and relations. Experiments provide data for cases and parameters which could not be modeled in CFD. After answering this question, the principle of ventilation is known and parameters of interest are quantified. These results are of interest in the second subquestion. To answer subquestion 2, literature is used to provide necesarry basic understanding of (computational) fluid dynamics. Experiments are conducted to make a prediction model and obtain validation data for CFD. Various CFD calculations are executed to answer to what extend numerical predictions are sufficient. All computational results are being obtained using CFD-code `ReFRESCO`, the in-house and open-usage viscous fluid code of MARIN. Experiments were conducted at the Depressurised Wave Basin.

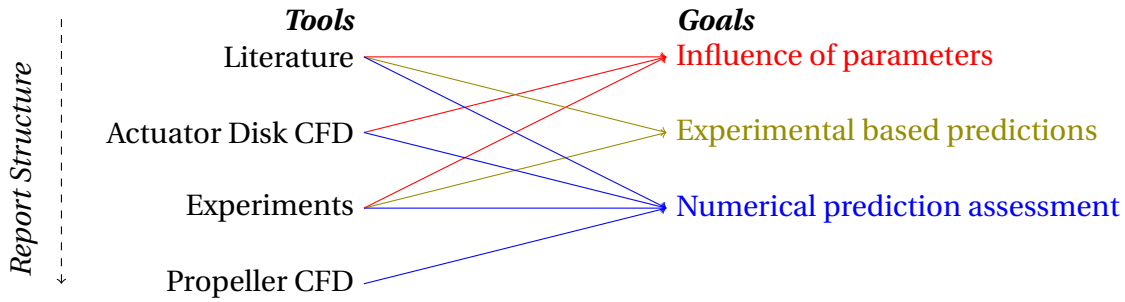

Figure 1.3: Application of different tools in the answering of research questions.

1.3. Report structure

This report follows the in fig. 1.3 listed tools for answering the research questions. The literature review can be found in chapter 2, where one can find useful information about ventilation. Also information about comparable phenonena, such as cavitation, propeller-hull vortex, surface piercing hydrofoils and surface piercing propellers can be found in that chapter. Parameters dependencies and conclusions found in literature are presenter thereafter, ended by an elaboration about scaling of the phenomenon. Brief information about the basics of fluid dynamics and computational applications can be found in chapter 3. Also CFD-research in propeller ventilation is found there. The literature study is followed by preliminary computational research in chapter 6. First of all, preliminary ventilation research using an actuator disk is presented and parameter dependencies found using CFD are shown. After this, results of a propeller grid study can be found. Lastly, the choice for turbulence model and assessment of the application of moving grids can be found. Chapter 5 briefly eloborates about the preperation and parameter choice of the physical experiments. Thereafter, experimental results and the polynomial model are presented, followed by further noticable effects found in the experiments. In chapter 6, computational results are shown and compared with experiments, to answer in what extend CFD is a proper tool for ventilation prediction. Conclusion and recommendations are found in chapter 7.

2

Physical phenomenon

2.1. Working principle of a propeller

Regular propellers are the most used ship propulsors. It outperformed the waterwheel from its development and is in the power-velocity area of regular shipping unbeatable compared to water jets, surface piercing propellers and air propellers. The largest contribution to the outperformance of the waterwheel was the application of the lift principle, instead of drag. Lift is the induced force due to a change of the flow velocity direction, leading to a low pressure area on the suction side and pressure difference between the suction and pressure side of a blade section, see fig. 2.1. Drag is the force due to oppression of the flow. The equations for lift and drag can be found in eq. (2.1) and 2.2. An object changing the flow direction is inducing lift. The amount of lift is dependent on the angle of incidence α. This is the angle between the inflow velocity direction and direction of the foil, see fig. 2.2. Dependent on α and the foil's shape, a certain lift and drag coefficient is found. For symmetical profiles, the lift coefficient can be linearized in $2\pi\alpha$. Lift is defined to act perpendicular to the inflow velocity direction, drag parallel to it.

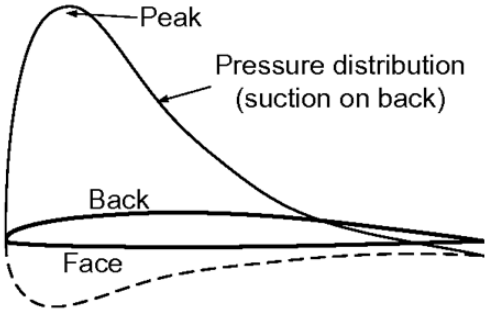

Figure 2.1: Negatieve peak pressure distribution over a foil section, from [59]

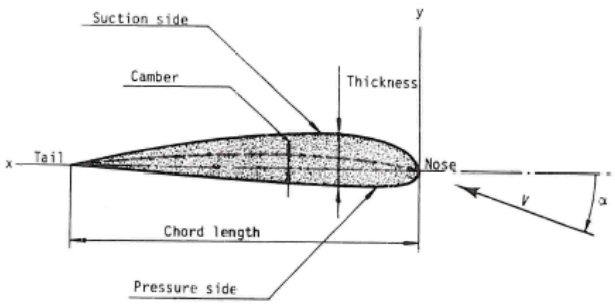

Figure 2.2: Geometry of a propeller blade, from [19]

$$L = \frac{1}{2}\rho C_l(\alpha) A v^2 \qquad (2.1)$$

$$D = \frac{1}{2}\rho C_d(\alpha) A v^2 \qquad (2.2)$$

2.1.1. Pitch

A propeller changes rotational power from the propeller shaft into transversal power. The distance the propeller moves during one rotation is the geometical pitch, mostly given as P/D, the pitch ratio over the propeller diameter. Each section of a propeller blade is in a certain geometrical pitch angle, θ, related to the P/D-ratio (eq. (2.5)). Furthermore the hydrodynamic pitch can be defined as the distance which the water travels during one propeller rotation. The hydrodynamic pitch angle is defined as the angle between in inflow velocity v_a and rotating velocity v_r (eq. (2.4)) and is closely related to the advance ratio J (eq. (2.3)). The angle of attack α is the difference between θ and β (eq. (2.6)) and corresponds to the slip of the propeller. One can derive that α and K_T is zero for J=P/D. The ratio $J/(P/D)$, i.a. used by Gutsche [22], is a for pitch corrected

advance ratio.

For a properly fitted propeller, α is small (such that flow is not separating on the blades). In off-design conditions, β is changing such that a lesser optimal angle of attack is found. A controllable pitch gives the possibility to adapt θ to the change of β and obtain a safe working point. Fixed pitch propeller does not offer that possibility, which makes them prone to engine overloading and/or thrust loss in off-design conditions.

$$J = \frac{v_a}{nD} \tag{2.3}$$

$$\beta = arctan(\frac{v_a}{\pi nD}) = arctan(\frac{J}{\pi}) \tag{2.4}$$

$$\theta = arctan(\frac{P/D}{\pi}) \tag{2.5}$$

$$\alpha = \theta - \beta \tag{2.6}$$

Lift and drag resulting from the propeller blade are to be reconstructed into the components in forward direction and radial direction. The sum of components in forward direction is giving the thrust (eq. (2.7)), at the cost of the torque composed of the components in radial direction and the arm (eq. (2.8)), drawn in fig. 2.3. Thrust and torque are mostly non-dimensionalized by the propeller rotation rate, diameter and density (eq. (2.9) and 2.10).

Propeller characteristics are changing dependent on the ratio of the inflow and rotational velocity, which is defined by J. For common J-values, K_T and K_Q are known for a certain propeller and can be given in the open water diagram, already found in fig. 1.2. Also propeller efficiency η_0 is plotted, which is defined as the ratio between transversal power and rotational power (eq. (2.11)).

$$T = \int L(r)sin(\beta(r)) - D(r)cos(\beta(r)dr \tag{2.7}$$

$$Q = \int r(L(r)cos(\beta(r)) + D(r)sin(\beta(r)))dr \tag{2.8}$$

$$K_T = \frac{T}{\rho n^2 D^4} \tag{2.9}$$

$$K_Q = \frac{Q}{\rho n^2 D^5} \tag{2.10}$$

$$\eta_0 = \frac{T \cdot v_a}{2\pi Qn} = \frac{K_T J}{2\pi K_Q} \tag{2.11}$$

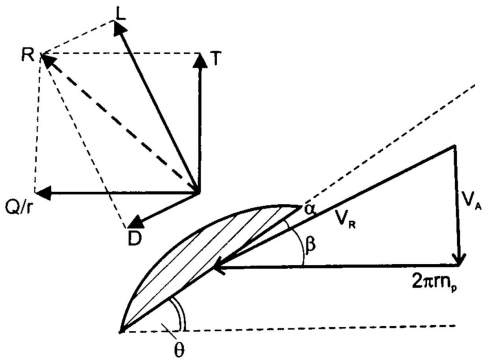

Figure 2.3: Hydrodynamic and geometric pitch angles and reconstruction of thrust and torque. from [39]

Finding the correct propeller for a ship in terms of diameter, rotation rate, blade number, pitch angle etc. is dependent on multiple ship characteristics as the resistance, wake factor, thrust deduction factor and speed. Propeller matching is making use of the open water diagram. For the procedure, I refer to Klein Woud and Stapersma [39], chapter 10 and 11.

2.1.2. Further propeller geometric parameters

A propeller blade is not only rotated around the length axis, but also perpendicular to the shaft (rake) and around the shaft (skew). Rake has little effect on the propeller performance and can be applied to increase tip clearance. Skew is applied to reduce unsteady pressure peaks [19] and cavitation/ventilation, in the wake peak at the 12 o'clock position behind a vessel.

Blade area is another important parameter to decrease cavitation/ventilation likeliness. As lift is the integral of the pressure over the blade area, a larger blade area gives a lower thrust per area. Keller [33] derived a criterion for the minimum blade area to prevent cavitation. Blade area is non-dimensionally given as the expanded area over the disk area: A_e/A_0. From this definition it is clear that A_e/S_0 can be reduced if the propeller diameter increases, as expanded blade area may be equal. Wageningen propeller series use this parameter in the disctinction of propellers; in the Wageningen C4.55, the propeller has 4 blades and an expanded area of 0.55.

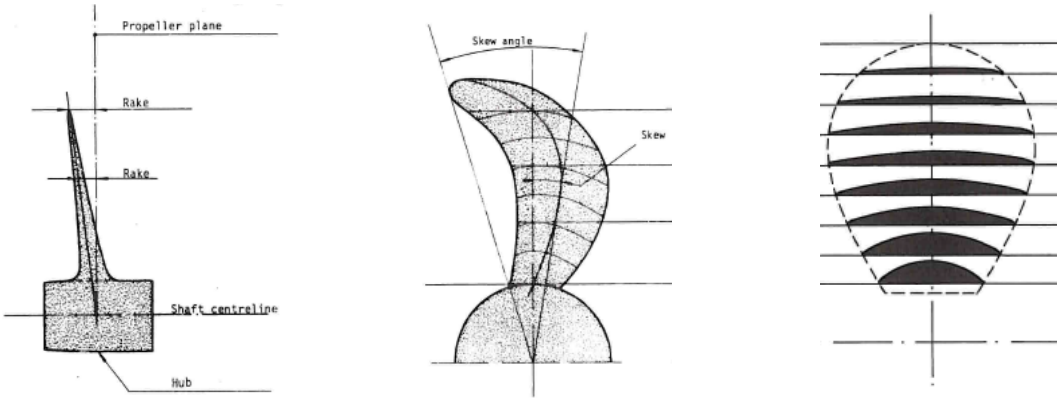

Figure 2.4: Rake, skew and expanded area of a propeller blade, from [19].

2.2. Propeller ventilation

Ventilation is the entrinment of atmospheric air into the propeller area. One of the first researchers in this topic, Shiba [72], gives the description:

"Air drawing of a marine propeller signifies the penetration of atmosphere through an air hole or along the blade surface in contact with atmosphere into the dead water region or sub-atmospheric region on the upper surface of the propeller blades".

According to Swales et al. [74], although derived for hydrofoils, there are three requirements for the occurence of (stable) ventilation. First of all, an area of separation has to be apparent. Tests with surface-piercing hydrofoils showed that a stable ventilating cavity could not exist before the foil was stalled. In non-stalled flows, the cavity immediately breaks away and is carried away by the flow. Secondly, a sub-atmospheric pressure is needed to build up a pressure gradient such that air is drawn. These low pressure areas are likely to occur in the low pressure peak of a propeller blade, in the low pressure area in front of the propeller of in a tip vortex core. Both requirements tend to occur in highly loaded propellers. Lastly there has to be a connection to airmospheric air. As Shiba already mentions in his definition, inception mechanisms differ in fulfilling this condition; a connection can be made by a vortex from the blade or by breaking through the free surface.

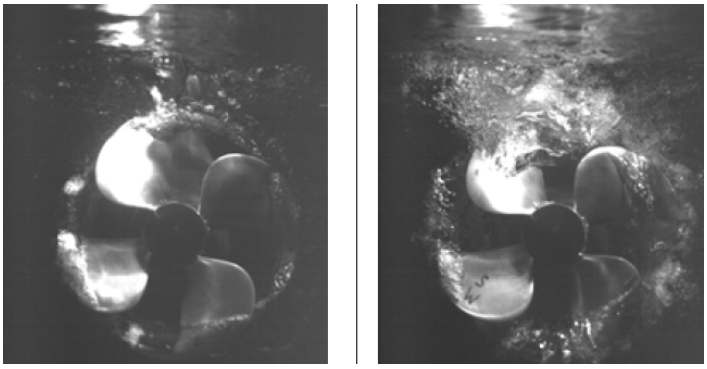

Figure 2.5: Examples of propeller ventilation, from [43]

.

2.2.1. Thrust loss and hysteresis

Thrust loss associated with ventilation can be substantial. In experimental research, Califano [5] and Koushan [42] found decreases up to 80% for certain propeller loadings and depths. The propeller thrust loss is often captured by the ratio β of the ventilation thrust(coefficient) over the deeply immersed thrust(coefficient). In fig. 2.6, one can see the influence on one rotation, where thrust is significantly reduced just after the 12 o'clock position at zero blade angular position. Depending on the severeness, significant breakdown is also found at other positions. In fig. 2.7, the effect on the open water propeller diagram can be seen, where partly and full ventilations are separated by a critical advance ratio.

$$\beta_T = \frac{T_{ventilation}}{T_0} = \frac{K_{T,ventilation}}{K_{T,0}} \tag{2.12}$$

$$\beta_Q = \frac{Q_{ventilation}}{Q_0} = \frac{K_{Q,ventilation}}{K_{Q,0}} \tag{2.13}$$

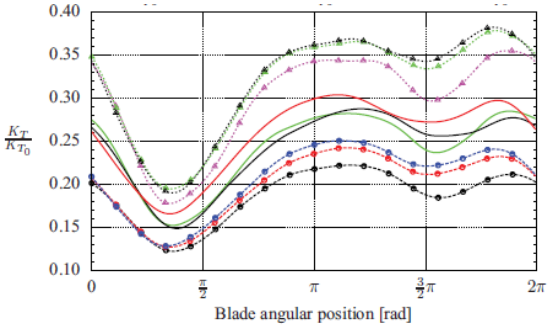

Figure 2.6: Influence of ventilation on thrust during one rotation, from [5].

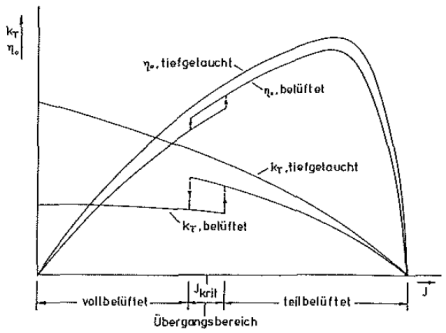

Figure 2.7: Influence of ventilation on open water propeller diagram, from [65].

The box around the critical advance ratio in fig. 2.7 is a bistable region. Depending on the origin (low or high J), the phenomenon behaves differently. This is known as hysteresis. Due to added resistance, e.g. in waves, loading of the propeller increases, which may incept ventilation. When thrust is then decreased, ventilation may wash out. Eventually this could lead to continuous inception and wash-out of (more severe) ventilation. Bistability leads to a decreased thrust, even if power should be sufficient in that condition, by taking engine margin into account [39]. In excessive situations, this can be problematic in heavy seas, where thrust loadings are continuously high and the propeller keeps ventilating. Especially when the propeller pitch is not controllable, a vessel could end up in a state when it no longer has enough thrust to even stay in position and loses control. In lesser severity, ship speed and efficiency decrease, which is neither favourable, although surmountable if in lesser demanding conditions overall efficiency is increased.

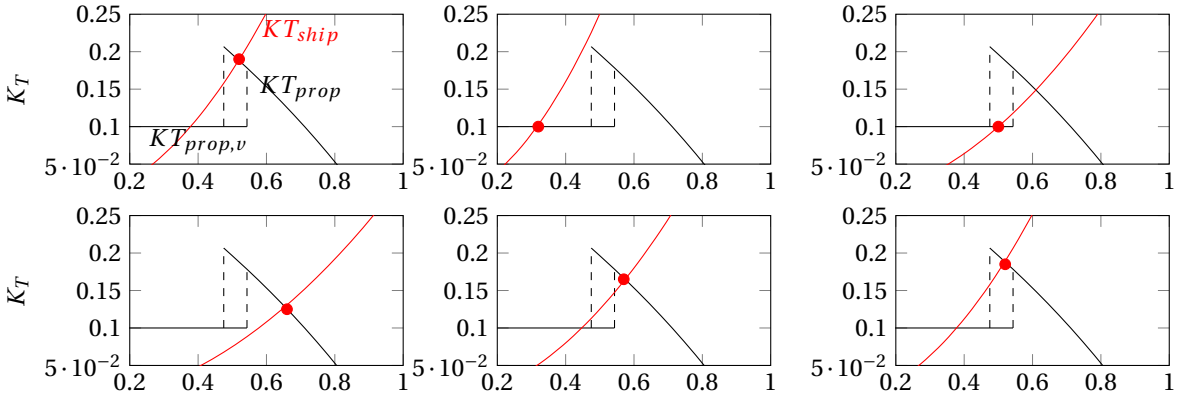

Figure 2.8: Hysteresis effects: (1) ship in heavy load conditions, where due to added resistance the propeller is heavier loaded and starts ventilating (2). Lesser loading then results in the ventilated K_T-curve (3), so lesser thrust is generated. If the propeller is even lesser loaded, the regular K_T curve is again followed (4), even when thrust loading is increasing more (5,1) until a new inception takes place (2).

2.2.2. Inception regimes and air provision

Ventilation inception modi are dependent on multiple parameters. It was shown that the immersion depth is an important parameter, on which three modi can be distuingished [7]. Close to the free surface or due to ship motions (fig. 2.9), the free surface is drawn into the propeller and air is provided, leading to free surface ventilation. More deeply immersed, the free surface can not be broken anymore and a ventilating vortex to the free surface provides air, called (propeller-free surface) vortex ventilation. A mixed zone exists inbetween these regions, where air is provided by a free surface vortex and surface breaking as well. Depths mentioned in the figure are indicative and strongly dependent on further parameters.

Figure 2.9: Ventilating propeller in heavy weater due to ship motions, from [32]

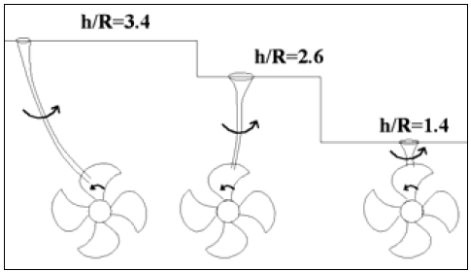

Figure 2.10: Inception at deep to moderate depths, from [43].

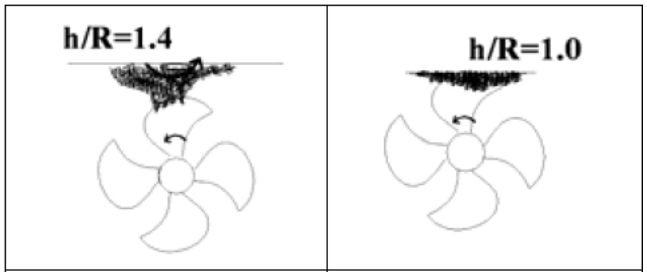

Figure 2.11: Inception and moderate and shallow depths, from [43].

2.2.3. Ventilation regimes

Thrust breakdown severity is dependent on the ventilation regime. The larger the area of the propeller blade is covered in air, the larger the thrust breakdown. Califano [5] distuingished three regimes; inception, partial ventilation and full ventilation. During ventilation inception, atmospheric air can only be found near the top of the propeller. In a more severe situation, air is advected along the rotation of the propeller, although it is detached before the full disc has filled with air. This is called partial ventilation. When air keeps attached to the blade for more than one rotation (so air is still apparent when new air is drawn), one speaks of full ventilation. The transition between partially and fully ventilation is however not completely clear and it is hard to differentiate between partial and full ventilation.

The ventilation regime is highly dependent on the inception regime and air provision. Ventilation inception by a vortex does not necessarily lead to full ventilation, as air provision might be insufficient. According to Califano [5], full ventilation immeadeately occurs after free surface breaking, although experiments showed this not to be by definition the case in lightly loaded propellers.

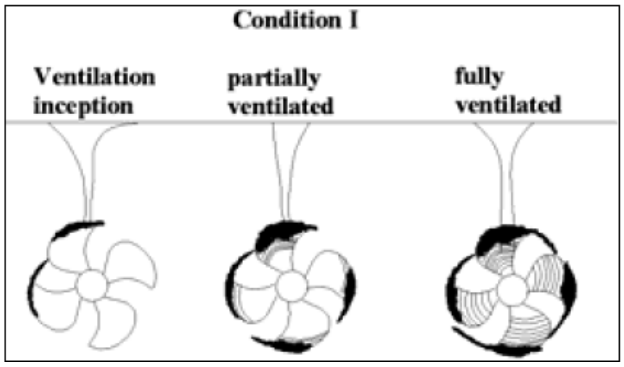

Figure 2.12: Regime at deep to moderate depths, from [43].

Figure 2.13: Regime and moderate and shallow depths, from [43].

Gutsche [22] already had a scientific more educated distinction between fully and partially ventilated, although it is still hard to differentiate based on visual results. He classifies the ventilation regime based on the extend of air suction at the suction side of the propeller. When the whole side is filled, it is considered full ventilation. Then the thrust only consists of the pressure difference between the positive pressure on the pressure side and the atmosperic pressure on the suction side and thus thrust decreased significantly.

A third classification of propeller ventilation was made by Sato et al. [69], who categorized based on the impingement of the air ventity; M-type starts from the mid chord (drawn by the local separation and low pressure peak); T-type only from the tip (when local low pressure or separation area on the blade is insufficient); and S-type from the blade leading edge and stretching over the blades towards the hub depending on the ventilation extent. Unfortunately there is no more in-depth explanation when to expect which ventilation regime, but it is expected that M-type is not likely to happen regarding the improvements in propeller design (w.r.t. application of skew and rake). Similarly, ventilation experiments by Kozlowska et al. [43] merely shows S-type air drawing. Submerged hydrofoils (see fig. 2.23) seem to show M-type ventilation. Schematic views can be found in fig. 2.14.

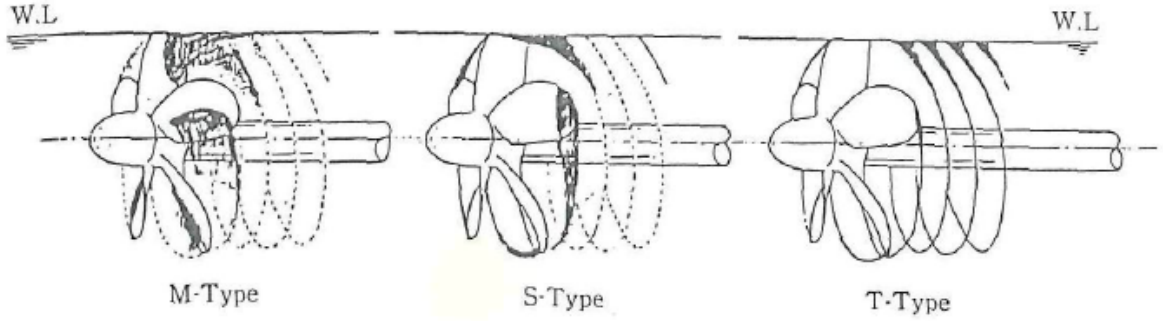

Figure 2.14: Ventilation Regime Classification according [69].

2.3. Similarity of ventilation to other phenomena

Regular propeller ventilation is not an often discussed subject in literature. However, partly similar phenomena can give more insight in the ventilation phenomenon too. Cavitation, propeller-hull vortex, surface piercing hydrofoils and surface-piercing propellers are elaborated upon in this section.

2.3.1. Cavitation

Ventilation is often being confused with cavitation. Both are gaseous entrapments in low pressure areas near/on the propeller and appear to be similar in model tests [75]. However, the physical background and effect is completely different. Whereas air in cavitation is provided via phase transition, atmospheric air is convected in case of ventilation. Furthermore the pressure in the cavitating air pocket is below the vapor pressure, in ventilation it is (near) atmospheric. The pressure difference between pressure side and vapor or atmospheric pressure is the origin why a small amount of blade cavitation does not directly lead to significant thrust breakdown, which is the case in blade ventilation.

One of the first who researched the influence of ventilation on cavitation and vice versa, is Brandt [2]. He endorses the similarity between cavitation and ventilation by classifying the thrust breakdown due to cavitation and ventilation according a similar trend. Based on the propeller loading, six regimes are separated, given in fig. 2.15. In experimental research he observes that cavitation and ventilation can coexist and coinfluence in partially conditions (1-3), i.a. by initiating a stable area on the blade surface. In regime 4-6, cavitation immediately follows ventilation when the free surface connection is lost, and vice versa when a connection is initiated. Furthermore experimental results showed that the cavitation number can not be neglected in lower loads (when cavitation and ventilation coexist), the influence of cavitation even grows when the propeller loads grows until full ventilation is reached. This can be found in fig. 2.15 as the deviation of dashed lines in phase 3. From phase 4 on, in full ventilation, the influence of cavitation becomes neglegible, according to Brandt [2] and ITTCs rules by Kruppa [46] .

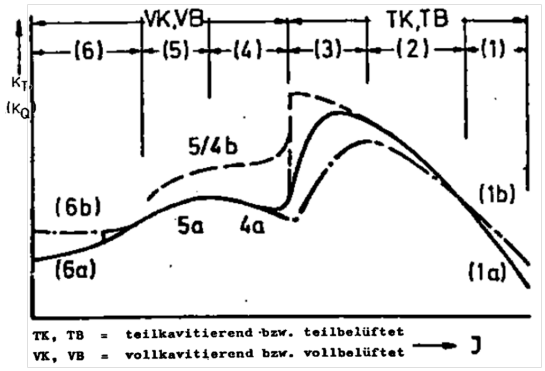

Figure 2.15: Ventilation regimes dependent on thrust loading for $1 < h_{shaft}/R < 2.2$ acc. to Brandt [2]. Dashed line indicate a high cavitation number, dashed-dotted line a low cavitation number. Cavitation number is influenced by local depressurizing. Explanation of phases 1 to 6 are given table 2.1.

Table 2.1: Description of phases found in fig. 2.15

(1)	Change of zero-crossing value and probable higher Kt.
(2)	Partial/vortex ventilation/cavitation in wake, T-type acc to Sato et al. [69].
(3)	Unsteady, seperating suction side ventilation/cavitation.
(4a)	Steady and full ventilation on suction side. Surface piercing blades are not spraying.
(5a)	Steady and full ventilation on suction side. Surface piercing blades are spraying.
(4/5b)	Steady and full ventilation that does not reach the propeller hub. WagB-series show this behaviour [49]
(6)	Full ventilation over the whole propeller, w/o spray.

Van Beek and Van Terwisga [75] also showed the coinfluence of cavitation and ventilation. In experiments in the depressurized wave basin at MARIN, a propeller behind a fast-sailing container vessel showed ventilation in the non-cavitating case, while in the cavitating case it did not show ventilation. This is ascribed to the moderating effect of sheet cavitation to the suction peak pressure.

2.3.2. Propeller-Hull Vortex

Initiation and existence of a propeller-free surface vortex is expected to be comparable to a propeller-hull vortex. First and major research into this topic was executed by Huse [29], who deduced the influence of various parameters on and derived a physical explanation for the initiation of the vortex. His most probable explanation is the 'pirouette' -effect, where due to the proximity of the plate, low wake velocity and a heavily loaded propeller, water recirculates above the propeller and creates a stagnation point in the flow. Conservation of rotational momentum then leads to an increased rotational velocity and the vortex. This local water velocity above the propeller close to zero may happen in the wake of a ship/thruster at the 12 'o clock position. Other hypotheses based on shear flow in the wake field and existing vortices are condidered less likely regarding the experimental results [29], although Sato et al. [70] speaks about influence of the propeller in his hypotheses.

In experimental results, Huse [29] concluded that the inception of a propeller-hull vortex is more dependent on the hull geometry rather than propeller geometry, although the propeller may still have influence too. Furthermore a lower advance ratio, smaller tip clearance and lower cavitation number are increasing the likeliness of propeller-hull vortex inception. A noticable effect that the vortex appeared to be the most stable for J=0.3 instead of J=0.1 was also found. In fig. 2.17 the extend in time of a vortex is given dependent on σ_v and J, probably as a consequence of cavitation or recirculation. Also recirculation of water above the propeller might be of influence. Lastly, from an operational point of view, Huse placed longitudinal skegs above the propeller, which prevented the formation of propeller-hull vortices, supporting the hypothesis of the 'pirouette'-effect. However, as the vortex has a predominant direction of rotation, there are other influences as well.

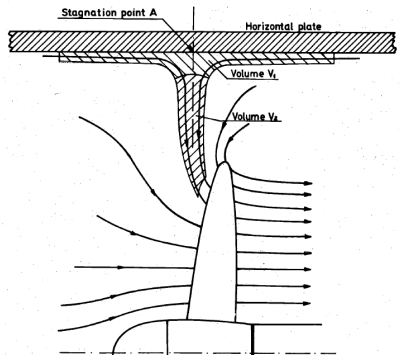

Figure 2.16: Vortex starting due to the 'pirouette'-effect, from [29].

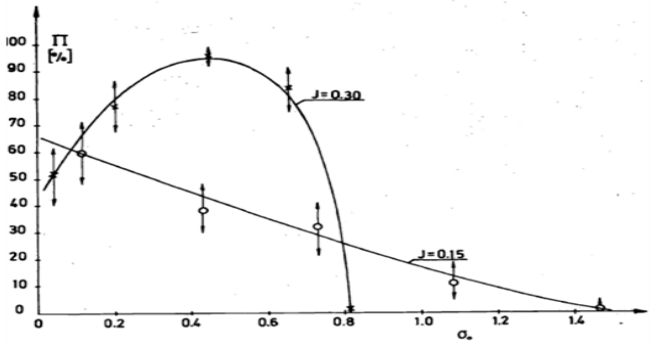

Figure 2.17: PHV-extend in percentage of time of complete test dependent on cavitation number and advance ratio, from [29]

Further experimental work was executed by Sato et al. [70]. In their work, patterns in the flow field are categorized in six regimes, found in fig. 2.18. Using potential flow analysis and experiments, the suction limit and boundaries between flow regimes are parameterized by the tip clearance and thrust loading. For high thrust loadings, regimes are only a function of tip clearance. fig. 2.19 show these regimes.

Also using potential analysis, they derived that next to the 'pirouette'-effect, a vortex may be generated by the same principle as in a bathtub. In the bathtub hypothesis, the vortex in the aft region (C/3 in fig. 2.18/fig. 2.19) is generated by the acceleration of the reversed flow due to the propeller tip. The predominant rotation direction is equal to the circulation around the propeller blade. Furthermore, experiments show in fig. 2.19 that the vortex regimes are only a function of tip clearance at high thrust loadings.

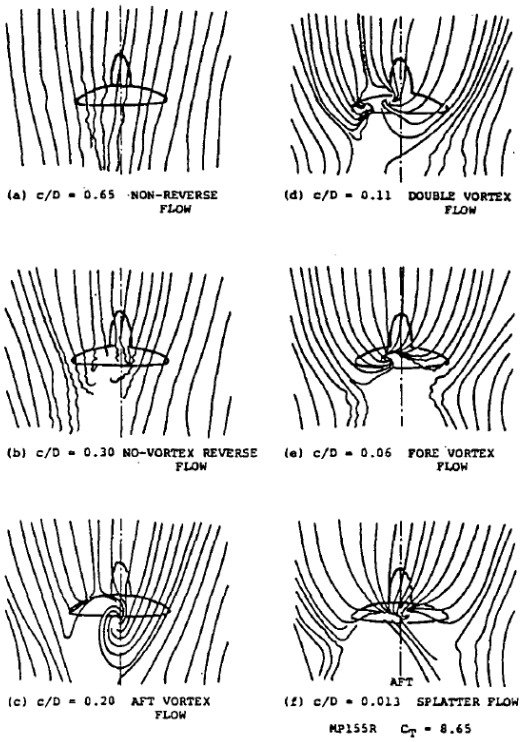

Figure 2.18: Flow regimes on a plate above the propeller, from [70]

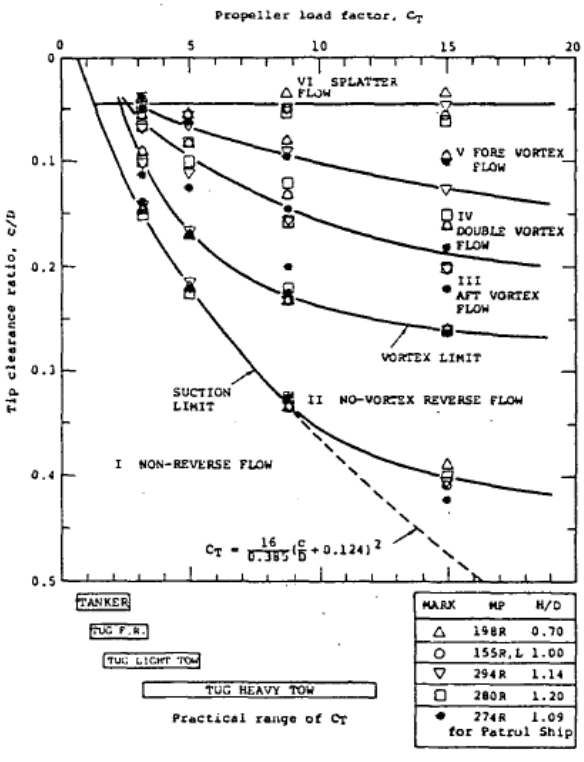

Figure 2.19: Flow regimes on the plate as function of thrust loading and tip clearance, from [70]

Numerical research into propeller-hull cavitation was conducted by Martio et al. [54]. Using RaNS code on a grid on only 500.000 cells, they found good agreeability in comparison with the vortex shapes and inception limits set by Sato et al. [70]. The origin of the vortex showed to be steadily positioned on the blade

surface, whereas the shape is influenced by the propeller blade position. The thrust coefficient was stronger influenced by the impingement of the vortex on the blade at $J = 0.249$, seen by the more unstable signal in fig. 2.20. However, thrust loss due to free surface proximity was found with and without impingement of the vortex on the blade.

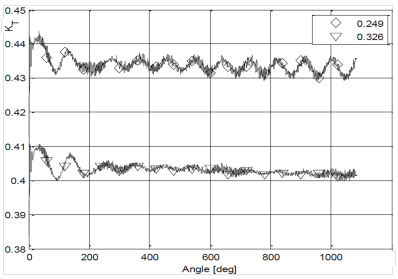

Figure 2.20: Time dependent thrust coefficient K_T for $J = 0.249$ and 0.326, from [54].

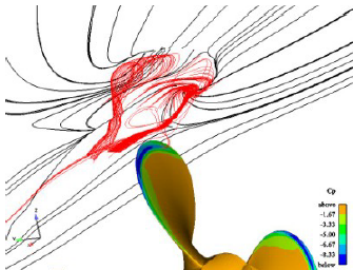

Figure 2.21: Vortex Impingement at the propeller blade at J=0.326, from [54]

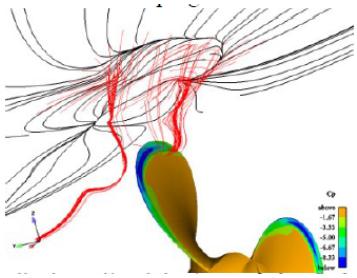

Figure 2.22: Vortex Impingement at the propeller blade at J=0.249, from [54]

2.3.3. Surface piercing hydrofoils

Also surface piercing hydrofoils are prone to ventilation. It is known that at high speeds, rudders A-class catamarans are ventilating and controllability of the boat is significantly reduced. Figure 2.23 shows the daggger board as investigated at the free surface cavitation tunnel at the University of Berlin [34], [20]. A comparable issue is found in wind surfing, when a skeg is ventilating and losing lift, leading to a spin-out of the board into the wind, personally experienced by the writer too. Figure 2.24 clearly shows the ventilating trough behind the board.

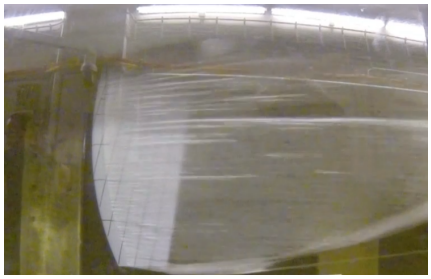

Figure 2.23: Ventilating A-cat hydrofoil. Note the rising tip vortex due to cavitation. From [20] and [34]

Figure 2.24: Spin-out during windsurfing due to ventilating skeg. Note the trough behing the board in the red oval. From [31]

.

Swales et al. [74] investigated ventilation inception of surface piercing hydrofoils. Whereas requirements set in the introduction are valid for hydrofoils, inception mechanisms are different than for propellers. At surface-piercing (airfoil-shaped) hydrofoils, a low-pressure area is apparent close to the free surface and immediately ventilation might be expected. However, Hay [26] found out that a thin layer of fluid at the surface does not seperate and so immediate ventilation is prevented. This effect may be found in propellers as well. Each succesive pertubation of this seal allows some air ingress, until the inception point is reached and the ventilating cavity is continuously fed. Inception via a tip vortex might also occur; due to a rising cavitating tip vortex or lowered water level after the flow, air may be drawn.

Sharp-nosed profiles were also taken into account in the experiments. A distiction of ventilation types was found dependent on the nose shape; sharp-nosed profiles could also incept due to separation at the leading edge. A long, non-cavitating nose bubble initiates a vortex which allows air ingress. As the vortex strength is dependent on the velocity, likeliness of nose ventilation increases with flow velocity. It also increases when the nose bubble size increases and the viscous damping decreases. In general nose ventilation occurs at lower incidence angles than regular ventilation. Due to the pertubation train necessary for stable tail ventilation instead of a single pertubation in nose ventilation, tail ventilation shows a higher repeatabity and controlability. This is however contradictory to the application of superventilating profiles in surface-piercing propeller.

According to Swales et al. [74], cavitation may initiate ventilation by acting as a stable region of seperating flow. Reducing ambient pressure reduces the inception angles in all cases, as was also found by [2]. Waves

are of infuence too; ventilation may occur in short wave crests due to farther draw-down of the free surface as a result of the vertical acceleration. Similarly, in long wave troughs ventilation may occur due to smaller distance to the free surface. This might not only be true for hydrofoils, but also for propellers.

Harwood, Brucker, Miguel, Young, and Ceccio [25] obtained close similarity between numerical and experimental results for a surface-piercing hydrofoil. In fig. 2.25 one can see that how the lift coefficient is influenced by the wetted or ventilated flow. It is shown that a bistable region exists between the bifurcation point an stall point. In the bistable region, the foil can be fully wetted, but also fully ventilated. Hysteresis occurs in this region. At angles smaller than the bifurcation angle, no bistability is found. Also from the moment the foil is stalled (also a bifurcation point as multiple circumstances lead to a single solution), the foil is fully ventilated and bistability is no longer found. The lift coefficient decreases in ventilating conditions.

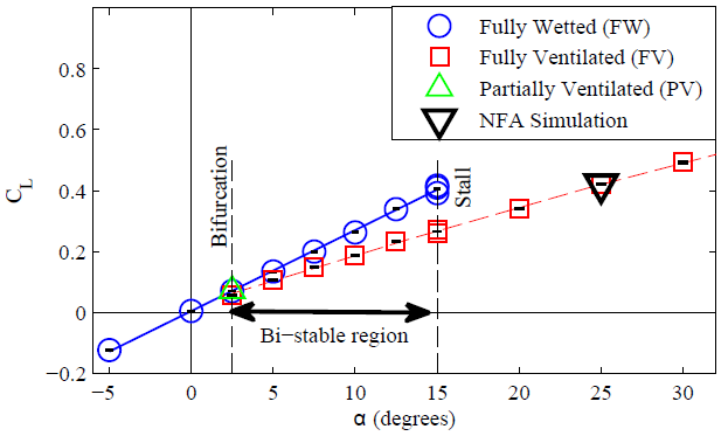

Figure 2.25: Lift coefficient influenced in the bistable zone. Note that fully wetted flow disappears after stall and fully ventilated flow after the bifurcation point. From [25].

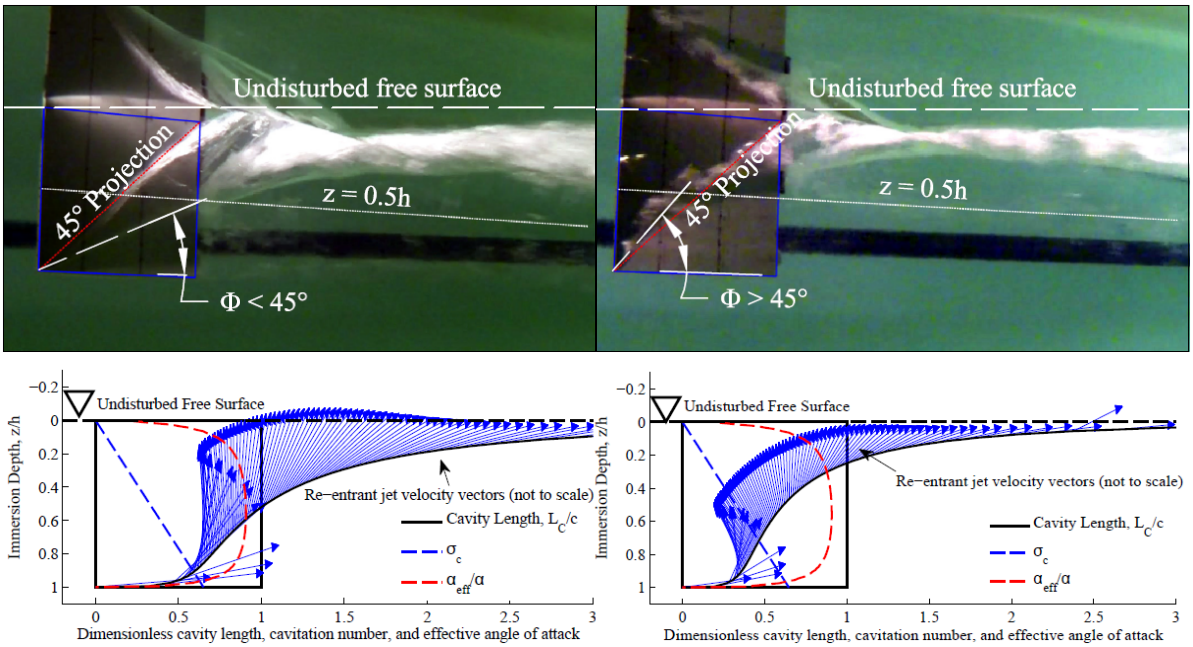

Figure 2.26: Proposed criterion for full or partial ventilation by Harwood et al. [25]. On the left the jet is not undercutting the cavity, thus FV. Right side is PV. Note that both would be considered PV before, based on the cavity length which is smaller that the chord length. From [25].

A further disctinction in the process to full ventilation is been proposed. First of all, inception has to take place; induced by a free-surface pertubations or induced by stall. After the inception, which leads to partial

ventilation, stabilization of the flow into full ventilation is said to occur. Whereas full ventilation was previously defined as a cavity running over the full chord of the foil, Harwood et al. [25] added the role of the re-entrant jet to the definition. If the jet undercuts the cavity, it is not stable and one speaks of partial ventilation. This is visible in fig. 2.26. One can imagine that this criterion is hardly applicable for propeller purposes.

The process of ventilation to attached flow, wash-out, had also been observed. This process has two phases; the transition from full ventilation to partial ventilation when re-entrant jet criterion cannot be met or the cavity no longer runs to the tip. A critical Froude number was derived for the first phase. Secondly the flow reattaches and all remaining air is carried downstream.

2.3.4. Surface piercing propellers

Propellers which are always working in the vicinity of the free surface are surface piercing propellers. These propellers have widely been researched by Oberembt [61], Hadler and Hecker [23] and Olofsson [62] in an experimental way. Young Young and Savander [86] used BEM-calculations together with FEM to analyse the hydroelasticity of the propellers. Yari and Ghassemi [85] and Himei [27] both executed viscous CFD-culculations on surface piercing propeller, both leading to agreeable results.
Surface piercing propellers depend on ventilation by piercing the waterline and the Wagner effect [77] to work properly; without the thrust deduction they overload the engine. Fully submerged, surface piercing propellers act as supercavitating propellers to take advantage of the cavities and so reducing water drag. SPP are found in high-speed craft, as the efficiency exceeds the regular propeller efficiency. Furthermore the absence of appendages is an advantage, as well as the absence of a water inlet in case of a waterjet driven vessel. Drawbacks are reduced efficiency in low speed conditions, high lateral forces due to asymmetric load, high blade stress and fatique issues and the lack of reliable design tools. [86]

Surface piercing propellers are in their design inherently different from immersed propellers to initiate full ventilation and supercavitation. The difference in the design of a surface-piercing propeller can be found in the foil shape. Whereas a propeller has in general a blunt nose and a sharp tail, a surface piercing propeller contrarily has a wedge shape; a sharp nose and a abrupt tail. The foil's shape initiates a stable ventilating or cavitating cavity from the leading edge until after the trailing edge, leading to full ventilation or cavitation, given in fig. 2.27. Since the design and working principle is inherently different, no further notice will be given to the physical background of surface piercing propellers. CFD-research is governed in section 3.3.

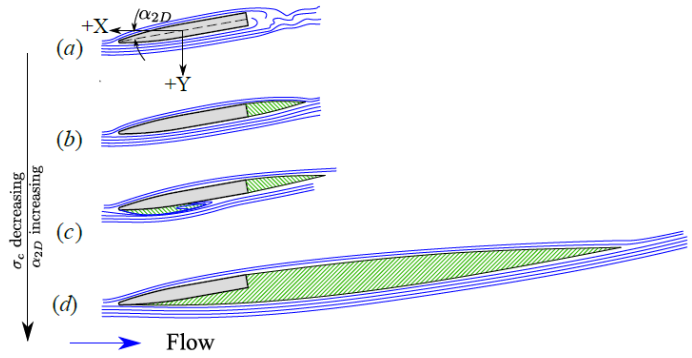

Figure 2.27: Ventilation of surface piercing propeller's characteristic foil shape, from [87]

2.4. Influencing parameters

2.4.1. Introduction of non-dimensional parameters

In the ventilation (inception) regimes it is already noted that ventilation is influenced by the depth of the propeller. Also thrust load is expected to influence ventilation. Furthermore non-dimensional numbers such as the Reynolds, Froude and Weber number might be of use. In this section, useful parameters are defined.

Immersion ratio I

The depth of the propeller is often non-dimensionalized by the radius or diameter. In literature, the depth is often defined as the depth of the propeller axis w.r.t. the undisturbed free surface. However, as the tip clearance is the shortest distance from the low pressure peak to the free surface, it might be physically more correct to define the immersion ratio according the tip clearance.

$$I = \frac{h_{tip}}{D} = \frac{1}{2}\frac{h_{shaft}}{R} \tag{2.14}$$

Thrust loading coefficient C_T

Thrust loading is non-dimensionally given by the thrust loading coefficient C_T. The coefficient denotes the velocity increase from the farfield to the disk plane and thus contraction of streamlines through the propeller. The derivation can be found below, where the definition of thrust using C_T is equalled to the thrust using the dynamic pressure jump:

$$C_T = \frac{T}{0.5\rho A v_a^2} \rightarrow T = \frac{1}{2}\rho C_T A v_a^2 \tag{2.15}$$

$$T = \rho A v_D^2 \tag{2.16}$$

which gives:

$$v_D^2 = \frac{1}{2} C_T v_a^2 \tag{2.17}$$

Thrust loading coefficient is also often seen as the thrust per area of the propeller. A lower C_T is obtained by increasing the propeller size, generally profitable in terms of efficiency.

The propeller thrust loading coefficient C_T can be deduced using J and the propeller load coefficient K_T. As propeller thrust coefficient K_T is a necessity to derive the thrust loading coefficient C_T, J on it's own is not sufficient to express the thrust load independent of the propeller characteristics. However, in serveral works such as Gutsche, Sato and Pohl, J is used to indicate the start of severe thrust breakdown and/or hysteresis.

$$C_T = \frac{8K_T}{\pi J^2} \tag{2.18}$$

Ventilation (inception) number σ_V

Ventilation might occur when a negative pressure gradient exists between the atmospheric pressure and the low pressure in the propeller disc, so air is drawn. The local pressure needs thus to be lower than the atmospheric pressure: $p_{local} - p_0 \leq 0$. The local pressure is a summation of the atmospheric pressure, hydrostatic pressure and dynamic pressure. In case of a negative pressure gradient, p_{dyn} must be a negative pressure.

$$\Delta p = p_{local} - p_0 = (p_0 + \rho g h + p_{dyn}) - p_0 = \rho g h + p_{dyn} \leq 0 \tag{2.19}$$

The ventilation number appears when the pressure gradient above is non-dimensionalized using the dynamic pressure. One should always be careful which ventilation inception number is used as several different definitions have been found in literature.

$$\sigma_v = \frac{(\rho g h_{tip} - p_{dyn})}{p_{dyn}} \leq 0 \tag{2.20}$$

$$= \frac{\rho g h_{tip}}{p_{dyn}} \leq 1 \tag{2.21}$$

An other way of looking at the ventilation number is the ratio of the 'preventing' pressure over the driving pressure. The ventilation number drops below zero when the driving negative pressure is larger than the hydrostatic pressure. A clear dependency of the propeller depth exists.

The origin of the driving pressure may differ per case. For an actuator disc it can be derived to be the dynamic pressure due to thrust, whereas for a propeller it is dependent on the ventilation regime. In free surface ventilation, the negative pressure is the dynamic pressure in front of the propeller due to thrust, whereas in vortex ventilation the negative pressure in the vortex is driving. Both have been described in Kozlowska et al. [45] as influencing low pressure areas.

If the pressure jump over the propeller, T/A, is used, the ventilation number for free surface ventilation can be derived, which is dependent on the increase of axial velocity via C_T:

$$\sigma_V = \frac{\rho g h_{tip}}{T/A} = \frac{\rho g h_{tip}}{0.5\rho C_T v_a^2} = \frac{2gh_{tip}}{C_T v_a^2} \tag{2.22}$$

If the negative pressure is equal to the dynamic pressure $\frac{1}{2}\rho v^2$, an apparent Froude number appears, shown in eq. (2.23) and often called the depth Froude number. However, as the physical derivation showed that this is actually a ventilation number, it is chosen not to use the depth Froude number, even if the ventilation number is a ratio between gravity and momentum forces.

$$\sigma_V = \frac{\rho g h_{tip}}{0.5\rho v^2} = \frac{2gh_{tip}}{v^2} = \frac{2}{Fr^2_{htip}} \tag{2.23}$$

Froude number Fr

The Froude number is a dimensionless parameter quantify the influence of the momentum forces to the gravitational forces. This is mainly of interest near the free surface. The diameter Froude number can be used in the quantification of the wave steepness due to contracting streamlines and in the potential of deforming the free surface.

If water flows at a high rate (high momentum forces), it is rather difficult to deform the free surface. The same applies if the length of the driving low pressure area due to the propeller thrust is short w.r.t. the wave length. Using potential wave equations, the wave length λ is equal to v_a^2/g, showing a dependency on the gravity; wave length grows with decreasing gravity. This is schematically given in fig. 2.28. It is assumed that the length of the low pressure area is linear in the propeller diameter.

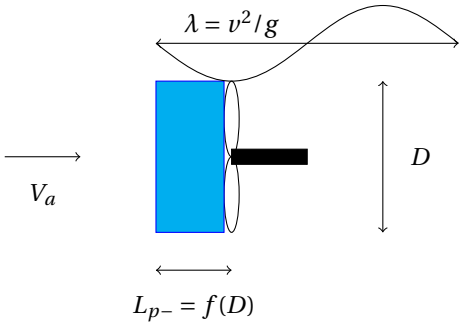

$$\frac{\lambda}{L_{p^-}} \text{linear in} \frac{\lambda}{D} = \frac{v_a^2}{gD} = Fr^2 \tag{2.24}$$

$$Fr = \frac{v_a}{\sqrt{gD}} \tag{2.25}$$

Figure 2.28: Schematic application of Froude Number in wave steepness description

So the diameter Froude number Fr_D is a non-dimensional parameter which indicates the potential of free surface deformation.

Reynolds number Re

The Reynolds number quantifies the ratio between the viscous and momentum forces. Based on the Reynolds number, it can be determined wheter a flow is laminar or turbulent. Reynolds number is mostly defined as eq. (2.26). μ and ρ are the dynamic viscosity and density. The quotient μ/ρ is defined as ν, the kinematic

viscosity.

$$Re = \frac{\rho u L}{\mu} = \frac{uL}{\nu} \tag{2.26}$$

For propeller use, Reynolds number is mostly used in the determination of flow state on the propeller blade. ITTC [30] defines therefore Reynolds number using the chord length ratio c/D and rotational velocity nD:

$$Re_{ITTC} = \frac{nD^2}{\nu}\frac{c}{D} \tag{2.27}$$

Weber Number We

The Weber number quantifies the ratio between the internal forces and surface forces. Especially at large curvatures or thin film flows, surface forces may not be neglected and the Weber number is of importance. σ is the surface tension from water to air.

$$We = \frac{\rho L u^2}{\sigma} \tag{2.28}$$

Other definitions of the Weber number were found in literature. Shiba [72], who derived a minimum Weber number for scaled test, used eq. (2.29). This definition is the square root of the aforementioned Weber number, where u is taken to be nD.

$$We = nD\sqrt{\frac{\rho}{\sigma}D} \tag{2.29}$$

2.4.2. Scaling

Full scale influence of propeller ventilation is of importance to identify risks associated with it. However, experiments in propeller ventilation were executed in model scale so scaling is necessary to identify the influence on full scale. Geometry, velocities and forces have to be extrapolated based on similarity laws. Geometric similarity is governed by the ratio between full and model scale, whereas the kinematic similarity is governed by the same advance ratio in model and full scale. Given the definition of the advance ratio, one could argue that this is a geometric similarity of the velocity inflow angle to the propeller blade. The dynamic similarity law may however differ between experiments.

$$\text{Geometric: } \alpha_L = \frac{L_f}{L_m} \tag{2.30}$$

$$\text{Kinematic: } \alpha_J = 1 \text{ or } J_m = J_f \tag{2.31}$$

$$\alpha_\beta = 1 \text{ or } \beta_m = \beta_f \tag{2.32}$$

Reynolds Scaling

Propeller thrust and torque needs to be predicted as accurately as possible. Therefore, accurate full scale viscous forces are necessary. To extrapolate model viscous forces correctly, the flow regime in model and full scale should coincide. The dynamic similarity based on the Reynolds number is governing for this. For well-immersed propellers or experiments without free surface, Reynolds extrapolation is used as long as this is possible. This scaling knows the problem of needing excessive revolution rates, which are mostly not workable. Within MARIN, revolution rates of 900 to 1200 rpm are used to ensure at least turbulent flow over the propeller blades, such that flow regimes are comparable. Similarity of the Reynolds number is not obtained. The following law is applied.

$$\alpha_{Re} = 1 \text{ or } Re_m = Re_f \tag{2.33}$$

Using Reynolds extrapolation, the following factor between full scale and model scale quantities exists, assumed that material properties do not change from model to full scale:

$$\alpha_L = \alpha_L \qquad \alpha_v = 1/\alpha_L \qquad \alpha_n = 1/\alpha_L^2 \qquad \alpha_t = \alpha_L^2$$

First of all, this extrapolation requires excessive and impossible revolution rates for the length scale factors which are used, see α_n. Furthermore, dynamic similarity of the ventilation phenomenon is not obtained, as the ventilation number in model scale far exceeds the full scale number.

Froude Scaling

Dynamic similarity may also be deduced from the ventilation number to scale the phenomenon correctly:

$$\alpha_{\sigma_v} = 1 \text{ or } \sigma_{v,m} = \sigma_{v,f} \tag{2.34}$$

Using the ventilation number for extrapolation, the following factor between full scale and model scale quantities exists, which are the same as for Froude scaling appears. This is not suprizing, as in eq. (2.23), it is already shown that the ventilation number also gives a ratio of the momentum and gravitational forces. Also the fact that free surface is of influence on ventilation, and free surface scaling (in wave-making resistance of a towing tank model test) always uses Froude number similarity supports the correctness of this scaling. Understanding relations are derived in appendix B.3.

$$\alpha_L = \alpha_L \qquad \alpha_v = \sqrt{\alpha_L} \qquad \alpha_n = 1/\sqrt{\alpha_L} \qquad \alpha_t = \sqrt{\alpha_L}$$

When using Froude scaling, the revolution rates are not excessive anymore and experimental results can be obtained. However, the viscous forces are not consistent in model scale compared to full scale, but underestimated due to the laminar flow on the blade entry sections and sections close to the propeller shaft in model scale. Solutions may be found in the placing of sand strips on the propeller blade, although it is chosen not to do so as it is unknown what further consequences of sand strips are to the working of the propeller, i.a. to cavitation inception. To obtain thrust breakdown as result of ventilation only, a deeply immersed open water diagram under Froude scaling will be made to correct the total thrust breakdown for incorrect viscous scaling. Deeply immersed results at low revolution rates also give the possibility to investigate the difference in obtained thrust dependent on the flow state. This is however not part of this work.

2.4.3. Former work on influencing parameters and prediction

Over the past years, research has been executed in the field of propeller ventilation to understand the phenomenon and indicate the influence of parameters. In 1953 Shiba [72] was one of the first who experimentally investigated a wide series of propellers in different conditions, whose results are still being used today in the ITTC-regulations [46]. Other worth mentioning researches were conducted by Gutsche [22], Pohl [66], Minsaas et al. [58], Kozlowska and Steen [44] and Califano [5].

The most valuable part of Shiba [72]'s work is the investigation to dependencies based on scaling parameters such as the Froude, Reynolds and Weber number. Investigation using spheres close to the water surface gives a dependency of the Froude number for free surface drawing according eq. (2.35).

For the Reynolds number defined as $Re = nDc/\nu$, as early as 1937 in the International Conference of Tank Superintendents, a minimum value of $Re = 4 \cdot 10^4$ had been opted for deeply immerged propellers tests [30]. Using results of Kempf (1938) and experiments under different temperature (so only changing ν), Shiba concluded that also close to the surface, no dependency of Re exists onto the inception. When the propeller is ventilating, the change of boundary layer on the downside of the blade was neglectible.

The most referred work of Shiba is the derivation of the minimum Weber number for free surface ventilation. According to Shiba, the surface forces are of greater importance than the gravity forces and inception should thus be parameterized by the Weber number. Similar tests under different temperatures, as in the Reynolds number investigation, showed a clear trend where the dependency of the Weber number on the critical advance ratio disappeared at $We = 180$. An overprediction of the Froude number in model scale might be the result of that. Results are shown in section 2.4.3. It appeared that, as this work is based on Froude scaling, the critical Weber number could not be exceeded.

$$\frac{z}{D} = \frac{1}{2} C \frac{v}{v_{ref}}^2 * Fr_D^2 \tag{2.35}$$

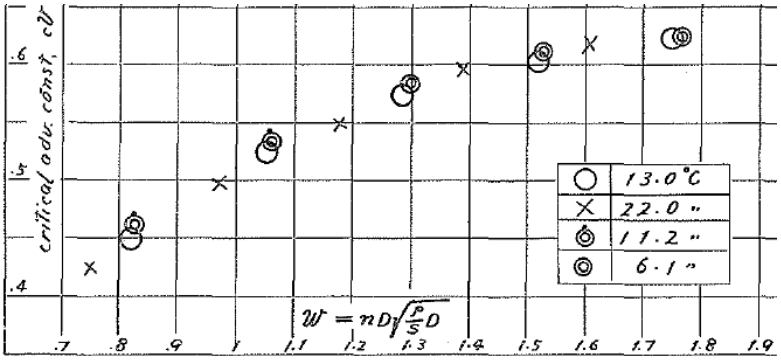

Figure 2.29: Test results showing the influence of the Weber number on the critical advance ratio. From [72].

Shiba [72] also put a lot of effort in the influence of propeller geometric parameters onto ventilation. Experimentally and mathematically he drew conclusions for the influence of expanded area, blade outline, airfoil shape, radial pitch distributions and skew. It should be noted that propellers investigated are not always comparable to modern ship propellers anymore. Conclusions derived by Shiba should thus always be used with care.

Gutsche [22] derived a pressure factor $\epsilon = \beta / C_{L,0.7R}$ in which he expressed the thrust diminution with regard to the propeller loading. It shows no dependency on the expanded area and blade number and a slight depencency on the pitch. Using ϵ, Gutsche obtains a critical advance ratio, although the derivation is missing in the paper. The effect on β of immersion depth and revolution rate is expressed in a circumferencial velocity depth froude number $Fr = \frac{n^2 D}{h/D}$, which is similar to a ventilation number. Plotted against C_T, Gutsche obtains fig. 2.31, which is a preliminary prediction of ventilation breakdown dependent on major parameters C_T, σ_V and I.

He also deduced the thrust diminuation during ventilation into three origins; thrust corrected for the loss of disk area, dynamic thrust comparable to suction side cavitation phenomena and the static pressure difference between suction and pressure side. Schematically the influence of each origin can be found in fig. 2.30; the largest contributor is the loss of low pressure area in the pressure jump.

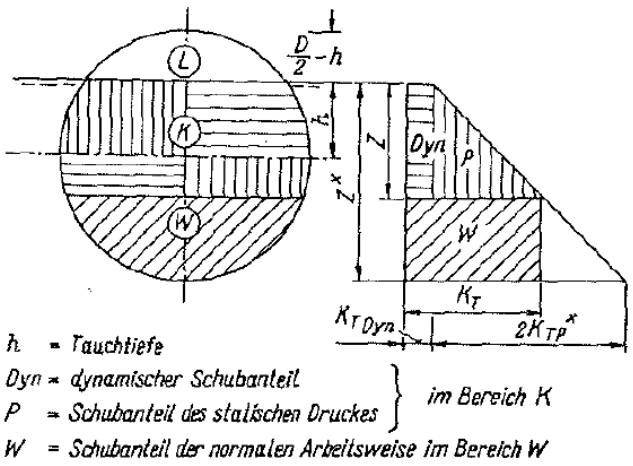

$$\beta_{DiskArea} = \frac{1}{2} + \frac{h_{tip}}{D} - \frac{z}{D} \tag{2.36}$$

$$\beta_{Dynamic} = (1 - \frac{J}{P/D}) \frac{z}{D} \tag{2.37}$$

$$\Delta p_{LossOfLowPressure} = \rho g z \tag{2.38}$$

Figure 2.30: Schematic overview of three thrust losses according [22].

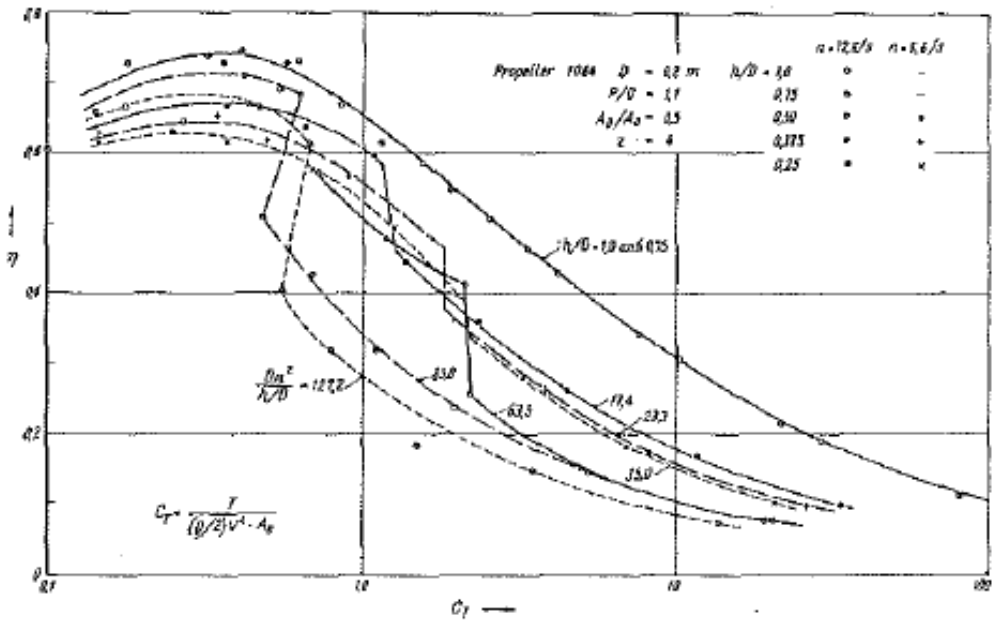

Figure 2.31: Effect of thrust loading and ventilation number on ventilation, from [22].

Pohl [66] extensively researched the effect of pitch for surface piercing propellers using data of Shiba [72]. A wide model series was evaluated on which approximation formulae are fitted. Using the ventilation number $\sigma_{v\infty}$, propeller loading C_T and the propeller pitch P/D, he obtained a border between air ingress and save operation found in fig. 2.32.

$$\sigma_{v,\infty} = \frac{2gh_s}{v_\infty^2} = \frac{2gh_s}{v_a^2} \cdot \underline{\frac{1}{1+(\frac{\pi}{J})^2}} \tag{2.39}$$

However, from the figure it is questionable if safe operations should be a function of P/D. One could see that C_T decreases with decreasing $\sigma_{v,\infty}$. This is as expected; a propeller with a lower pitch needs more rotations (thus lower $\sigma_{v,\infty}$) to give the same C_T and vice versa. Several points of $C_T = 1.5$ and $\sigma_{v,\infty} = 1.0$ were extracted from fig. 2.32 to indicate the dependency on P/D.

The thrust loading coefficient C_T can be rewritten into the advance ratio J and propeller thrust coefficient K_T. As K_T changes with P/D, also J must change to obtain corresponding C_T. By absence of propeller data of the used propeller, Wageningen C-series had to be used to rewrite C_T into J. The propellers are comparable in terms of blade area and P/D, but not in blade shape. If J is obtained, the in eq. (2.39) underlined correction factor can be calculated. If the resulting, regular ventilation number is equal for all data, the dependency on P/D does not exists, but is a result of dependency on C_T. As in table 2.2 an unequal ventilation number σ_V is obtained, an effect on P/D may still exist.

Table 2.2: Values obtained for the revolution rate during inception, derived from fig. 2.32

P/D	$\sigma_{v,\infty}$	C_T	J using $K_T\|_{WagC}$	$\frac{1}{1+(\frac{\pi}{J})^2}$	σ_v
0.8	1.0	1.8	0.47	0.044	22.5
1	1.0	1.3	0.62	0.073	13.6
1.2	1.0	1.0	0.76	0.107	9.3
1.4	1.0	0.7	0.91	0.147	6.8
0.8	0.7	1.5	0.50	0.049	14.0
1.0	1.5	1.5	0.59	0.066	22.3
1.2	3.2	1.5	0.66	0.084	38.0

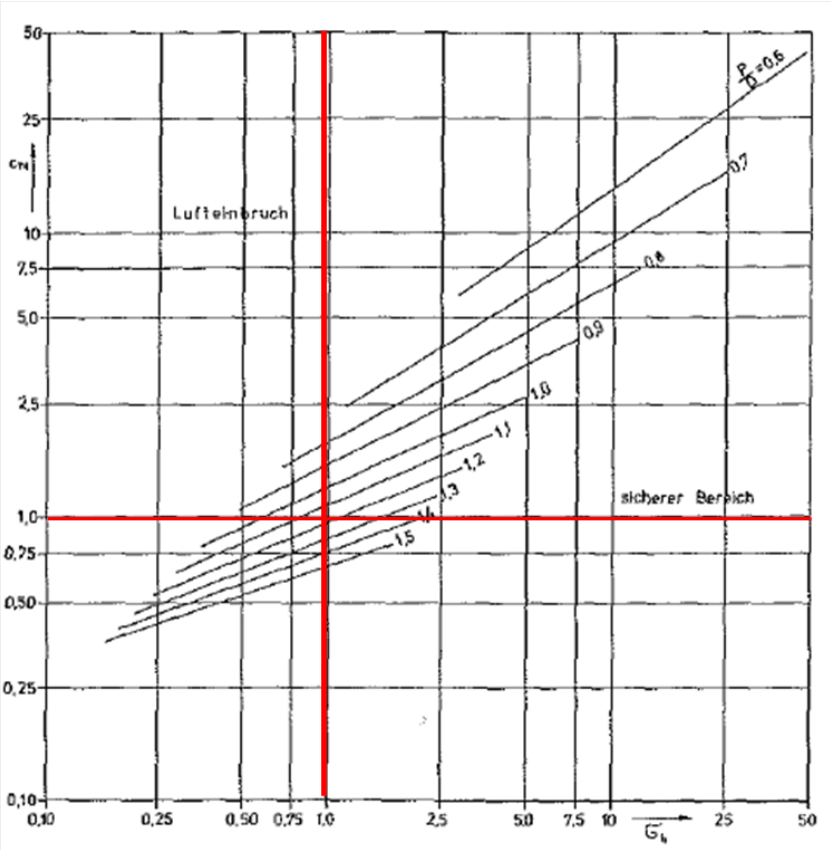

Figure 2.32: Effect of P/D on ventilation, from [66] and [65]. The orange line indicates the values taken for the revolution rate calculation.

Besides Gutsche [22], more researchers contributed to (empirical) thrust breakdown component equations. Fleischer [18] improved the loss of disk area by deriving the loss for a circular disk, instead of a squared disk Gutsche was using, found in eq. (2.40). Minsaas et al. [58] added empirically the effect of wave-making of the propeller based on results of Kempf [35], eq. (2.42) and the Wagner effect eq. (2.41). This effect describes the lift build up after sudden immersion, which is half the steady lift and grows with travelled chord lengths to the full steady lift [77]. Lastly the ventilation thrust loss in eq. (2.43) is comparable to the derivation of Gutsche, although now derived by Minsaas. The total thrust loss due to placing near the free surface is obtained by the product of β. Hagesteijn and Brouwer [24] showed that the dynamic Wagner model provided the best results compared to experiments. For thrust only, the propeller independent steady state (empirical) model of Guoqiang et al. [21] for β also provided good results [24].

$$\beta_{DiskArea} = 1 - \frac{arccos(h/R)}{\pi} + \frac{h}{\pi R}\sqrt{1-\left(\frac{h}{R}\right)^2} \qquad \text{for} h_{shaft}/R < 1.0 \tag{2.40}$$

$$\beta_{Wagner} = 0.5 + 0.5\sqrt{1-\left(\frac{155 - V_\infty t/c}{155}\right)^{27.59}} \qquad \text{for } h_{shaft}/R < 0.7 \tag{2.41}$$

$$\beta_{Wave-making} = 1 - 0.657(1 - 0.0769(h/R)^{1.2358}) \qquad \text{for } h_{shaft}/R < 1.3 \tag{2.42}$$

$$\beta_{Ventilation} = \frac{1.5EAR}{K_T} * (\frac{\pi}{2}\alpha + \frac{2gh}{v_\infty^2}) \tag{2.43}$$

$$\beta_{Total} = \Pi_i^n \beta_i \tag{2.44}$$

The last major investigation into ventilation is conducted at the NTNU and Rolls-Royce center for Performance in Seaway by Califano [5], Kozlowska et al. [43] and Koushan [42]. Rolls-Royce initiated this research as ventilation was resulting in thruster gear breakdown in offshore dynamic positioning applications. Excessive experimental test at high thrust loadings by Califano gave the dependency of thrust breakdown to

immersion depth and thrust loading coefficient in fig. 2.33. Results from all experimental tests are published by [44] in fig. 2.34. On the vertical axis, a re-written thrust loading coefficient is placed, see eq. (2.17) to derive $v_d/v_0 = \sqrt{C_T/2}$. Using the experimental result, a boundary for ventilation regimes based on [62] is derived dependent on C_T and I. Towards high C_T, the dependency on the immersion seems to disappear. Furthermore extrapolating the boundaries to $v_d/v_0 = 0$ seems incorrect as $v_d/v_0 = 1$ is a zero-thrust situation and boundaries should be extrapolated to there. These two facts make the dependency of ventilation regimes on C_T questionable.

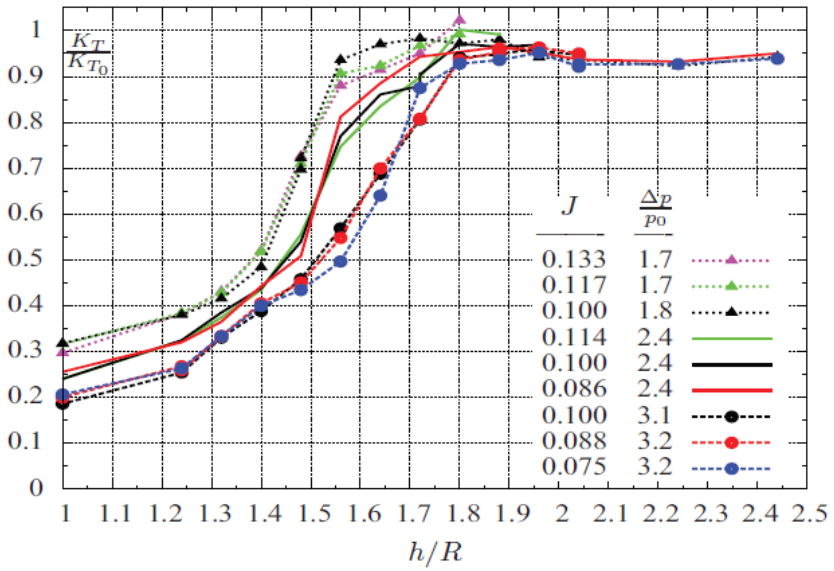

Figure 2.33: Ventilation thrust breakdown as function of h_{shaft}/R at multiple thrust loadings and advance ratios, from [5].

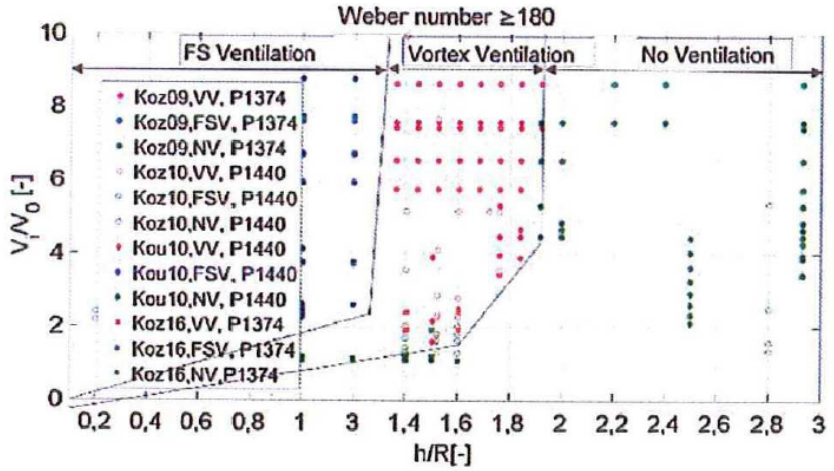

Figure 2.34: Ventilation regime prediction as function of h/R and $v_d/v_0 (= \sqrt{C_T/2})$, obtained from multiple test series. From [44].

3

Fluid dynamics

An important part of this research is the numerical calculations on ventilation. To be able to understand the choices made, basic understanding of fluid dynamics is essensial. This chapter will briefly provide this knowledge for fluid dynamics in general and for computational fluid dynamics in particular. As the software used is an incompressible flow solver, equations will be derived for incompressible flow. Knowledge of this chapter is mostly extracted from Kundu et al. [47], White [79], Brennen [3] and Nieuwstadt et al. [60] .

3.1. Basics of Fluid Mechanics

A fluid is a substance that deforms continuously under applied shear stress. It has no preferred shape, like a solid has. For a Newtonian fluid, the deformation is linear to the applied shear stress.

$$\tau = \mu \frac{\partial u}{\partial y} \tag{3.1}$$

3.1.1. Conservation equations

Several quantities are being conserved in physics. Well-known examples are mass, (linear) momentum and energy. To accurately model the physics, it is obvious that these laws should be applied in the model. For fluid dynamics, conservation of mass and linear momentum are giving the Navier-Stokes equations. Energy is implicitely conserved in incompressible flow.

A general expression, often called the advection-diffusion equation, for conservation of quantity Q is given in eq. (3.2). It states that a quantity change over time (on the left hand side) is a contribution of three phenomena. The first, given by $\nabla \cdot (D\nabla Q)$, is called the diffusion. Diffusion is the spreading of the quantity from (in case of positive diffusion constant D) high concentration to low concentration volumes. Secondly $\nabla \cdot (\mathbf{u}(\mathbf{x}, t)Q)$ is the advection. This is the transport of the quantity due to flow velocity. Together the diffusion and advection are transporting the quantity in the domain. Lastly $q_{source/sink}$ is stated. This is the creation and/or destruction of quantity Q in time.

$$\frac{\partial Q}{\partial t} = \nabla \cdot (D\nabla Q) - \nabla \cdot (\mathbf{u(x,t)}Q) + q_{source/sink} \tag{3.2}$$

For the sake of clearancy, $\mathbf{u}(\mathbf{x}, t)$ is denoted as $\mathbf{u}$, although it is a function of space and time.

Conservation of mass

One of the keystones of numerical methods is the conservation of mass. Aforementioned general conservation equation is used in deriving the applicable form in the numerical methods.

Unless velocity is near the speed of light, mass can neither be created nor destructed. Mass can neither be accumulated within a cell volume locally, nor globally in a volume of multiple cells. Mass is given by the volume integral of the density, conservation as the prohibition of change over time, given in eq. (3.3).

$$\frac{d}{dt} \iiint_{V(t)} \rho(\mathbf{x}, t)\, dV = 0 \tag{3.3}$$

Expansion of eq. (3.3) using Reynolds transport theorem gives a statement in which the boundaries are explicitly part of the mass conservation. eq. (3.4) shows the change of mass is partly dependent on the change of density ρ in the volume and partly the mass in- and outflow over the boundaries. In differential form, the statement can be found in eq. (3.5). Compared with eq. (3.2), it can be noticed that mass conservation is in fact the change of density ρ where the diffusion and source terms are zero.

$$\iiint_{V(t)} \frac{\partial \rho(\mathbf{x},t)}{\partial t} dV + \iint_{A(t)} \rho(\mathbf{x},t)\mathbf{u}\cdot\hat{\mathbf{n}} dA = 0 \tag{3.4}$$

$$\frac{\partial \rho(\mathbf{x},t)}{\partial t} + \nabla\cdot(\rho(\mathbf{x},t)\mathbf{u}) = 0 \tag{3.5}$$

To obtain the incompressible continuity equation, the second term in eq. (3.5) can be rewritten using the material derivative D/Dt of $\rho(\mathbf{x},t)$:

$$\frac{\partial \rho(\mathbf{x},t)}{\partial t} + \mathbf{u}\cdot\nabla\rho + \rho(\nabla\cdot\mathbf{u}) = 0 \tag{3.6}$$

$$\frac{D\rho}{Dt} + \rho(\nabla\cdot\mathbf{u}) = 0 \tag{3.7}$$

Mass conservation states that $D\rho/Dt$ equals zero. Then $\rho(\nabla\cdot\mathbf{u})$ must be equal to zero too. As ρ is strictly positive, the incompressibility contraint or continuity equation appears. It is never assumed that ρ is constant, so even for a variable density flow (as in multiphase VoF-solvers), the continuity constraint is governing for mass conservation. Derivation is found in the `ReFRESCO` manual [53].

$$\nabla\cdot\mathbf{u} = 0 \tag{3.8}$$

Conservation of momentum

The physical principle behind the conservation of momentum M is Newton's second law. Simplified, this law states that the sum of all forces equal the mass times acceleration. However, this is not complete. The sum of all forces is equal to the change of linear momentum over time.

$$\sum \mathbf{F} = \frac{d\mathbf{M}}{dt} = \frac{d}{dt}\iiint_{V(t)} \rho\mathbf{u} dV \neq m\mathbf{a} \tag{3.9}$$

Forces acting on a fluid can be divided in volume body forces and surface forces. Volume forces are buoyancy and gravity forces, which can be described a force per unit volume. Surface force is friction, which can be described as a force per unit area:

$$\sum \mathbf{F} = \mathbf{F}_{body} + \mathbf{F}_{surface} = \iiint_{V} \rho\mathbf{g} dV + \oiint_{A} f_{surface}\hat{\mathbf{n}} dA \tag{3.10}$$

Reynolds transport theorem is applied on the right hand side of eq. (3.9). Together with eq. (3.10), the result give the momentum equation.

$$\iiint_{V(t)} \frac{d}{dt}(\rho\mathbf{u}) dV + \iint_{A(t)} \rho\mathbf{u}(\mathbf{u}\cdot\hat{\mathbf{n}}) dA = \iiint_{V(t)} \rho\mathbf{g} dV + \oiint_{A(t)} f_{surf}\cdot\hat{\mathbf{n}} dA \tag{3.11}$$

Using Gauss' theorem, two surface integrals from eq. (3.11) can be rewritten into volume integrals (eq. (3.12) and eq. (3.13)).

$$\iint_{A(t)} \rho\mathbf{u}(\mathbf{u}\cdot\hat{\mathbf{n}}) dA = \iiint_{V(t)} \nabla\cdot(\rho\mathbf{u}\mathbf{u}) dV \tag{3.12}$$

$$\oiint_{A(t)} f_{surf}\cdot\hat{\mathbf{n}} dA = \iint_{A(t)} \hat{\mathbf{n}}\mathbf{T} dA = \iiint_{V(t)} \nabla\cdot\mathbf{T} dV \tag{3.13}$$

Substituting these give the momentum equation in integral form in eq. (3.14). The differential form can be found in eq. (3.15). The differential form can also be written in terms of the material derivative, see eq. (3.16). This one is also known as the Cauchy momentum equation.

$$\iiint_{V(t)} \frac{d}{dt}(\rho \mathbf{u}) dV + \iiint_{V(t)} \nabla \cdot (\rho \mathbf{u}\mathbf{u}) dV = \iiint_{V(t)} \rho \mathbf{g} dV + \iiint_{V(t)} \nabla \cdot \mathbf{T} dV \tag{3.14}$$

$$\frac{d}{dt}(\rho \mathbf{u}) + \nabla \cdot (\rho \mathbf{u}\mathbf{u}) = \rho \mathbf{g} + \nabla \cdot \mathbf{T} \tag{3.15}$$

$$\rho \frac{D\mathbf{u}}{Dt} = \rho \mathbf{g} + \nabla \cdot \mathbf{T} \tag{3.16}$$

The tensor **T** describes the surface forces acting on the fluid. Diagonal elements T_{aa} describe the normal stresses, off-diagonal elements T_{ab} the shear stresses. For a Newtonian fluid, this tensor is symmetric; $T_{ij} = T_{ji}$ and in the limit of $dV = dxdydz \rightarrow 0$, the tensor has only six independent entries.

Applicable surface forces are pressure forces and shear. Pressure is acting normal to the surface; it is a normal stress and therefore on the diagonal of **T**. In rest, this is the only acting force, leading to $T_{ij} = -p\delta_{ij}$, where δ_{ij} is the Kronecker delta. The Kronecker delta is 1 on the diagonals where $(i = j)$ and 0 if not $(i \neq j)$. When the fluid is not in rest, stress components τ_{ij} are added to T_{ij}: $T_{ij} = -p\delta_{ij} + \tau_{ij}$. For incompressible flow, the deviatoric stress tensor τ_{ij} is often assumed to be equal to $2\mu S_{ij}$, known as the Boussinesq assumption. S_{ij} is the rate of strain tensor Substituting in eq. (3.16) gives the incompressible Navier-Stokes momentum equation in eq. (3.19). Without viscous effects ($\mu = 0$), the Euler equation appears in eq. (3.20).

$$T_{ij} = -p\delta_{ij} + 2\mu S_{ij} \tag{3.17}$$

$$\rho \frac{D\mathbf{u}}{Dt} = \rho \mathbf{g} + \nabla \cdot (-p\delta_{ij} + 2\mu S_{ij}) \tag{3.18}$$

$$\rho \frac{D\mathbf{u}}{Dt} = -\nabla p + \rho \mathbf{g} + \mu \nabla^2 \mathbf{u} \tag{3.19}$$

$$\rho \frac{D\mathbf{u}}{Dt} = -\nabla p + \rho \mathbf{g} \tag{3.20}$$

3.1.2. Flow states

A flow has two major states; laminar and turbulent. Laminar flow is characterized by the smooth and organized flow, while turbulence is known to be chaotic. It is defined as small scale variations of a quantity in a flow. The non-dimensional number often used to describe the flow's state, is the Reynolds number found in section 2.4.1.

Deducting the flow's state can be done by means of stability analysis. Adding a small pertubation to the particular solution and substituting this sum in equations of motion derives a new eigenvalue-problem. If the non-trivial solution grows in time, then the flow is turbulent. If the solution decays, the the flow is stable and thus laminar. If the solution is not dependent on time, the flow is neutrally stable. An other manner of deducting the flow's state, is by experimental results. For certain flows it is known for which Reynolds number the flow changes from laminar to turbulent. For a flat plate, Schlichting and Gersten [71] derived that the flow is laminar for $Re < 5e5$ and turbulent for $Re > 1e7$. The region $5e5 < Re < 1e7$ is known as the laminar-turbulent transition region. In fig. 3.2 it is visible that in model scale according Froude scaling, the flow is in the laminar-turbulent transition regime.

The transition of flow from laminar to turbulent is widely researched. Instabilities leading to turbulence are likely to occur in boundary layers or free shear layers. Shear flow instabilities are known as Kevin-Helmholtz instabilities. Instabilities directly due to viscosity, the driving force in a Poiseuille flow are called Tollmien-Schlichting instabilities. As effects of viscosity and shear are common in the boundary layer, the boundary layer is a source for turbulence. [60]

In a turbulent flow, energy is more rapidly dissipated than in a laminar flow. As a result, turbulent flow has in general more drag force along an object. On the other hand; the boundary layer of a turbulent flow separates later, delaying pressure losses. Wheter a turbulent boundary layer is desired, is case dependent. Obviously in many cases one does not have the design freedom to design the flow's state as velocity or lengthscales are too large. Examples of a desirable laminar flow are internal pipe flows, whereas dimples in a golf ball are used to

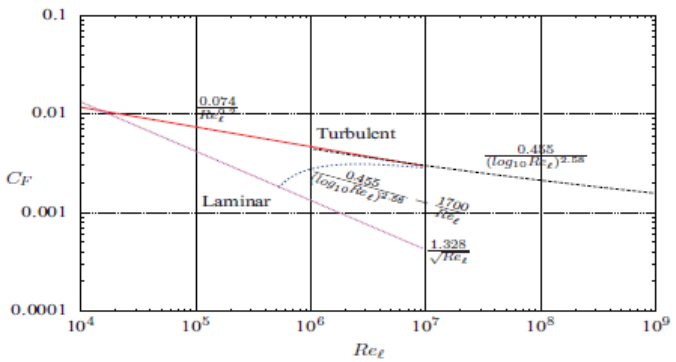

Figure 3.1: Difference in drag coefficient due to skin friction between turbulent and laminar flow dependent on Re_l, from [71], adapted by [5].

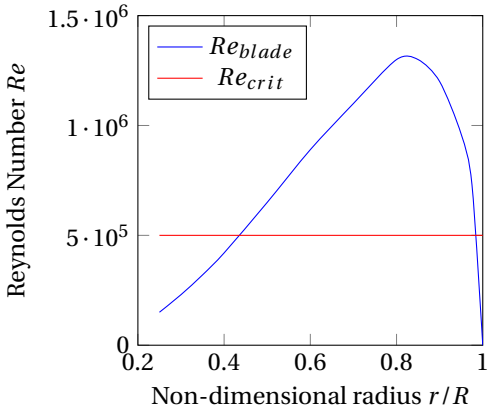

Figure 3.2: Reynolds number over a C4.55 propeller blade of $D = 0.23294m$ at $J = 0.2$ and $N = 10rps$.

delay separation by making the flow turbulent and so diminsh the frictional (form) drag.

Model tests are often interesting with regard to flow state. Because of Froude scaling, turbulent flow around full scale vessel might be rescaled to laminar flow around the scale model. Extrapolation of model test results without taking the flow state in consideration will lead to errors. Prevention from such errors is done by means of sand strips at the scale model to suppress laminar flow.

3.1.3. Vorticity

Vorticity is the amount of rotation in the flow. It is defined as the curl of the velocity field and has a direction perpendicular to the flow direction. A positive and a negative vorticity area may exist, which corresponds to the rotation direction of the vortex. Also without a defined vortex, vorticity may exist when flow accelerated near a body surface, such as the vorticity around an airfoil.

$$\Gamma = \nabla \times \mathbf{u} \tag{3.21}$$

Expressing the vorticity in fluid dynamics is often done by the means of the Q-value. This value is the 'relative' vortex strength, defined as:

$$Q = \frac{1}{2}(||\Omega||^2 - ||S||^2) \tag{3.22}$$

$$\Omega = \frac{1}{2}(\nabla u + (\nabla u)^T) \tag{3.23}$$

$$S = \frac{1}{2}(\nabla u - (\nabla u)^T) \tag{3.24}$$

3.1.4. Compressibility

Compressible flow modeling is necessary when Mach numbers are exceeding 0.3. The Mach number is the fluid velocity over the speed of sound in the respective medium. For water, the speed of sound is around $1500m/s$ and thus the critical Mach number of 0.3 is hardly exceeded. However, for water-air mixtures, the speed of sound reduces significantly according eq. (3.25) to $24m/s$ for a mixture of 50% air dissolved in water [3] [84], which is visible in fig. 3.4. One could expect compressibility to be of importance where phases are mixed. On the other side, incompressible cavitation calculation do still show sufficient results on global level.

$$c_\alpha = 1/\sqrt{\Big(\alpha\rho_a + (1-\alpha)\rho_w\Big)\Big(\frac{\alpha}{\rho_a c_a^2} + \frac{1-\alpha}{\rho_w c_w^2}\Big)} \tag{3.25}$$

When taking compressibility into account, aforementioned Navier-Stokes equations change. As the material derivative of the density is no longer zero, the continuity equation eq. (3.8) can not be derived from eq. (3.7). The valid mass conservation can already be found in eq. (3.5). The momentum equation needs an equation of state for the relation between the density and pressure, often derived from the energy conservation, which

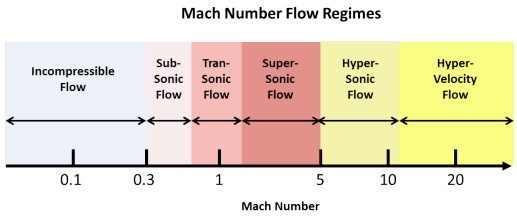

Figure 3.3: Mach Number Regimes, from [81]

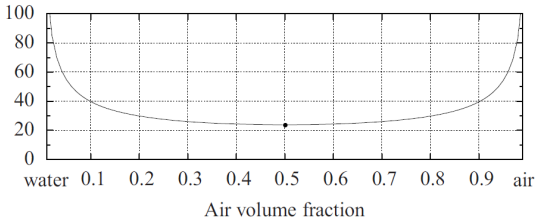

Figure 3.4: Speed of sound in an air-water mixture. The black dot represents the low speed of sound at $\alpha = 0.5$, from [5] [84].

will couple the thermodynamics to the kinematics and dynamics of the flow. As compressible flow is not applied in this work, this derivation is left behind.

3.2. Computational Fluid Dynamics

The software made use of is `ReFRESCO`. The name is an acronym for *REliable and Fast RaNS-Equations (solver for) Ships and Constructions Offshore.* and is optimized, verified and validated for maritime use. `ReFRESCO` is a viscous-flow CFD code that solves multiphase unsteady incompressible flows using the RaNS equations and VoF-method. The equations are discretized using a finite-volume approach with cell-centered saving of variables. Many turbulence methods are available and various grid settings can be used such as movable, deforming and adaptive grids.[53]

Figure 3.5: `ReFRESCO` logo, from [53].

3.2.1. RaNS-equations

Implementation of the Navier-Stokes equation is often done by means of RaNS. RaNS is the acronym for *Reynolds-averaged Navier-Stokes.* Averaging is applied to diminish computational costs. By averaging, information about small scale fluctuations of quantities in the flow is lost. Turbulence is therefore hardly possible to simulate and has to be modeled instead using turbulence models.

Derivation of the RaNS-equations is being performed by substituting the sum of a average value and the fluctuations for the velocity $\mathbf{u}$ and pressure p in the Navier-Stokes equations, and then ensemble averaging these equations. The average is defined as the time average over the time domain of the simulation. Fluctuations are defined as the difference between the time dependent value and the average. Due to this definition, the time average of the fluctuating part is zero. The derivation of the RaNS-equations can be found in appendix A.2, for the mass conservation in eq. (3.26) and for the momentum conservation in eq. (3.27) yields:

$$\nabla \cdot \overline{\mathbf{u}} = 0 \tag{3.26}$$

$$\rho \frac{D\overline{\mathbf{u}}}{Dt} = -\nabla \overline{p} + \mathbf{F} + \mu \nabla^2 \overline{\mathbf{u}} - \rho \overline{\mathbf{u'} \cdot \nabla \mathbf{u'}} \tag{3.27}$$

The last term on the right hand side of the momentum equation is called the Reynolds stress or apparent turbulent shear stress. This term arises from averaging, which is clearly visible in comparison with eq. (3.19). The arising term is often taken into the deviatoric stress tensor from eq. (3.17), such that the Reynolds stress tensor from eq. (3.28) gives the RaNS momentum equation. The Reynolds Stress term leads to closure problems. Because this term can not be neglected, turbulence modeling is applied to close the system.

$$T_{ij} = -p\delta_{ij} + 2\mu S_{ij} - \rho \mathbf{u'} \cdot \nabla \mathbf{u'} \tag{3.28}$$

$$\rho \frac{D\overline{\mathbf{u}}}{Dt} = \mathbf{F} + \nabla \cdot T_{ij} \tag{3.29}$$

3.2.2. Turbulence modeling

Basis of most turbulence models is the (incompressible) Boussinesq approximation (eq. (3.30)), which assumes that turbulence is generated by shear flow. It therefore states that the Reynolds stress term is proportional to the rate of strain tensor. An apparent viscosity μ_t is constructed from turbulence kinetic energy and lengthscales, often called eddy viscosity of turbulent viscosity.

$$-\rho\overline{\mathbf{u'}\cdot\nabla\mathbf{u'}} = \mu_t S_{ij} \tag{3.30}$$

Recalling eq. (3.28) and inserting Boussinesq's approximation for the Reynolds stress terms show the similarity between the molecular and eddy viscosity in eq. (3.32). Eddy viscosity is modeled in turbulence models, e.g. as eq. (3.34) for $k-\omega$-equations and eq. (3.43) for LES. k, the turbulent kinetic energy, is defined as $\frac{1}{2}u_i' u_i'$.

$$T_{ij} = -p\delta_{ij} + 2\mu S_{ij} + \mu_t S_{ij} \tag{3.31}$$

$$T_{ij} = -p + (2\mu + \mu_t) S_{ij} \tag{3.32}$$

$k-\omega$-models

k-ω turbulence models are widely applied in closing the RaNS-equations. Based on succesful application in propeller calculations, it is decided to use a $k-\omega$-model. Originally, the two-equation model is developed by Wilcox [83] and consists of transport equations for turbulence kinetic energy k and specific turbulent dissipation ω. The latter is linked to specific disspation rate ϵ, as used in the $k-\epsilon$ turbulence models according eq. (3.33)

$$\epsilon = \beta_k \omega k \tag{3.33}$$

Advantage of the $k-\omega$-model is the indepencency on the wall distance in calculations. Furthermore the model is less stiff than the k-ϵ model in near wall regions. On the other side, the original set of parameters gives a strong depencency on the free stream turbulence variables, which is of great influence on free-shear separation layers [56]. As the k-ϵ model does not have this dependency, Menter [55] succesfully blended the k-ω and k-ϵ models. However, problems in the application of $k-\epsilon$-models can be expected.

For $k-\omega$ turbulence models, the turbulent length scale l and turbulent kinetic energy k determines the eddy viscosity according eq. (3.34) and turbulent dissipation ϵ according eq. (3.35). Both are used in the transport equations for k and ω in eq. (3.36) and (3.37), which describe the change these over time.

$$\nu_t = l\sqrt{k} = \frac{k}{\omega} \tag{3.34}$$

$$\epsilon = \beta_k \frac{k^{3/2}}{l} \tag{3.35}$$

$$\frac{\partial k}{\partial t} + \frac{\partial(\rho k u_j)}{\partial x_j} = P_k - \rho\epsilon + \frac{\partial}{\partial x_j}\left((\mu + \sigma_k \mu_t)\frac{\partial k}{\partial x_j}\right) \tag{3.36}$$

$$\frac{\partial \omega}{\partial t} + \frac{\partial(\rho \omega u_j)}{\partial x_j} = P_\omega - \beta\rho\omega^2 + \frac{\partial}{\partial x_j}\left((\mu + \sigma_\omega \mu_t)\frac{\partial \omega}{\partial x_j}\right) + C_D \tag{3.37}$$

In which P is production, $\rho\epsilon$ and $\beta\rho\omega^2$ are dissipation and C_D is the cross-diffusion term. σ-, α- and β-terms are closure coefficients which differ between various $k-\omega$ turbulence models.

$$P_k = \tau_{ij}\frac{\partial u_j}{\partial x_i} = \tau_{ij}\nabla u \tag{3.38}$$

$$P_\omega = \frac{\alpha_\omega \omega}{k} P_k \tag{3.39}$$

$$C_D = \sigma_d \frac{\rho}{\omega} max\left(\frac{\partial k}{\partial x_i}\frac{\partial \omega}{\partial x_i}, 0\right) = \sigma_d \frac{\rho}{\omega} max\left(\nabla k \nabla \omega, 0\right) \tag{3.40}$$

The $k-\omega$ models are using the Boussinesqs assumption that turbulence is generated by shear flow. Many turbulence models use this statement in the modeling of turbulence in the fluid by assuming the turbulence production of eq. (3.38) to be a function of the rate of strain tensor. In many cases, this is a valid assumption, but in vortices it is not. A vortex is essentially laminar. However, due to the large velocity gradient since the flow is rotatins, lots of turbulence is generated. According to eq. (3.34), the eddy viscosity is overpredicted due to excessive production of kinetic energy and the vortex is modeled to be too diffusive.

$k-\omega$ TNT

In an attempt to exclude the free-stream turbulent parameter depencency, Kok [40] derived new values for σ_k, σ_ω and σ_d postulating a weak solution of a 1D-diffusion equation at the turbulent/not-turbulent front which is moving over time. Boundary conditions that *(1)* ω, k and u must go to zero at the turbulent/non-turbulent front (such that the weak solution exists) and *(2)* that the velocity profiles has a physically correct finite slope yield new turbulent parameters. Based on the first boundary condition, the free stream variables are expected to be not of influence in the non-tubulent region. This is contrary the model of Wilcox, which does not satisfy the constraint. The $k-\omega$ model parameters of Menter do not satisfy the second boundary condition and is invalid as ω goes to infinity when approaching the turbulent/non-turbulent front.

$k-\omega$ TNT-XLES

Secondly a hybrid method called $k-\omega TNT-XLES$ (shortly XLES) is applied. XLES consists of RaNS $k-\omega$-TNT modeling and a k-equation subgrid scale model (LES). XLES, acronym for Extra Large Eddy Simulation, simulates turbulent structures which are supported by the grid and models structures which are not, instead of modeling all turbulence. According to eq. (3.34), dissipation is therefore smaller in LES-regions. The XLES-formulation uses the same formulation of the turbulent kinetic energy as RaNS k-models and still uses Boussinesq's assumption, found in eq. (3.36), but models the eddy viscosity differently. Furthermore it does not need the ω-equation. Dissipation rate is given in eq. (3.44) instead. Drawbacks may be expected as Pereira et al. [64] mentioned significant 'challenges' in *(1)* the errors of RaNS/SRS at the interface and *(2)* forcing the onset of turbulence on the leading edge.

Distinction between XLES and RaNS is made based on what extent the grid supports LES-calculations by comparing the LES filter with to the turbulence length scale according eq. (3.42). Filter width Δ is by default the largest edge length of the cell. In case of a grid study, the filter width Δ may be fixed [41].

Near solid walls, l goes to zero and the $k-\omega$ model is applied. Where the flow is turbulent (large turbulent length scale l) and the filter width is small enough, LES is applied. Since l typically decreases in LES-mode, back-and-forth switching between RaNS and LES may occur, until local equilibrium of production and dissipation is reached. Definitions for ν_t and ϵ in k-equation SGS LES-mode are found in eq. (3.43) and eq. (3.44), where C_1 is calibrated to 0.06 and C_2 such that ν_t and ϵ switch simultaniously [41]. Contrary to eq. (3.34), it can be found that turbulent dissipation is bounded by the filter width and does not grow with decreasing turbulent length scales anymore.

$$\text{if } C_1\Delta < l \rightarrow \text{TNT} \tag{3.41}$$

$$\text{if } C_1\Delta > l \rightarrow \text{TNT-XLES} \tag{3.42}$$

$$\nu_t = C_1\Delta\sqrt{k} = 0.06\Delta\sqrt{k} \tag{3.43}$$

$$\epsilon = C_2\frac{k^{3/2}}{\Delta} = \frac{\beta_k}{0.06}\frac{k^{3/2}}{\Delta} \tag{3.44}$$

3.2.3. Convective flux dicretization

Discretized convective equations are often dependent on the downsteam cell face value. Many interpolation schemes can be used in obtaining this value. Most basic, one can project the cell's centre value on the forward face, called *First Order Upwind (FOU)* or *Upwind Differencing (UD)*. This method is highly stable, but at the cost of first order accuracy and diffusion. Backward differencing may be applied in high resolution applications. Then the face value is set to the downstream cell center, leading to more robustness. Higher order methods can also be used; non-linear and linear schemes are applied. Linear schemes of the mostly used κ-family follow understanding equations, such as central differencing (CDS) and QUICK. ϕ in eq. (3.45) is the equation for the downstream face value, where Φ_C is the value in the cell center. and Φ_U the value in the upstream cell center. eq. (3.46) is a limiter function, in this case linear in r (under the assumption that $\kappa \neq f(r)$. Several values for κ and $\phi(r)$ are given in section 3.2.3. r is the ratio between difference downstream and upstream value in the cell center.

Higher order schemes are in general more accurate. Drawback of the higher order schemes is a lower degree of robustness. Non-linear schemes, using flux limiters, bounds $\phi(r)$ to be in the TVD-region. TVD stand for Total Variation Diminishing. The Total Variation in a timestep n is a indication of change:

$$\Phi_f = \Phi_C + 0.5\phi(r)(\Phi_C - \Phi_U) \tag{3.45}$$
$$\phi(r) = 0.5[(1+\kappa)r + (1-\kappa) \tag{3.46}$$
$$r = (\Phi_D - \Phi_C)/(|\Phi_C - \Phi_U) \tag{3.47}$$

Table 3.1: Values of κ and $\phi(r)$ for often used schemes. Note that FOU is 1st order and thus $\phi(r)$ is no function of r.

Scheme	**order**	κ	$\phi(r)$
FOU	1st	-1	0
CDS	2nd	1	r
QUICK	2nd	0.5	0.75r+0.25
Fromm	2nd	0	0.50r+0.50

$$TV(|\Phi^n) = \int_x |\frac{\partial \Phi^n}{\partial x} dx \tag{3.48}$$
$$= |\Phi_2 - \Phi_1| + ... + |\Phi_{Icells} - \Phi_{Icells-1}| \tag{3.49}$$

If a discretisation is TVD, then no new local extrema must be created and absolute values of existing local maxima may not increase. In other words, the total variation at timestep $n+1$ must be equal or smaller than at timestep n:

$$TVD \text{ if: } TV(\Phi^{n+1}) \leq TV(\Phi^n) \tag{3.50}$$

Flux limiters are used to bound $\phi(r)$. Most flux limiters are based on linear schemes. Applied limiters are Van Leer/Harmonic (`ReFRESCOs` default [53] and part of ReFRICS) [36] and superBEE [68]. Many more are available too. The limiter functions of Van Leer, which is smooth, and SuperBEE, which is piece-wise constant, are:

$$\phi_{VanLeer}(r) = (r + |r|)/(r+1) \tag{3.51}$$
$$\phi_{SuperBEE}(r) = max(0, min(2r,1), min(r,2)) \tag{3.52}$$

Graphically the stability regions and limiter functions are listed in the Sweby-diagram fig. 3.6. This diagram shows the stability region, which is bounded between two discretization schemes. The Warming & Beam scheme produces wiggles after a top head profile, the Lax-Wendroff scheme before. By blending the new scheme between these two schemes, a stable scheme is obtained. This area is coloured blue. The darker blue regions are proven by Sweby to be TVD. [78].

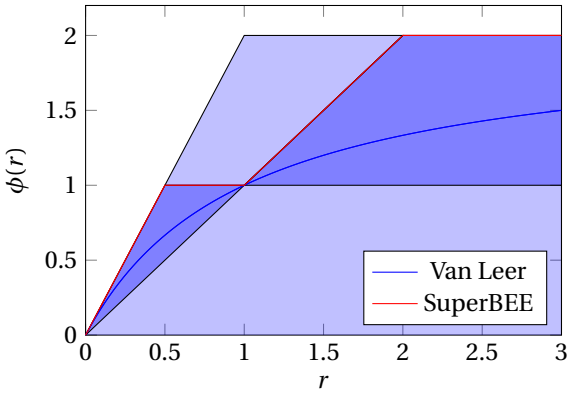

Figure 3.6: Sweby diagram, consisting of blue stable areas between Lax-Wendroff and Warming& Beam schemes. Darker blue area is proven by Sweby to be TVD. Both Van Leer's and SuperBEEs scheme are in the last area.

3.2.4. Multiphase modeling

The most common multiphase flows in marine applications are gas-fluid flows, for instance in ship wave pattern calculation, cavitation or ventilation. Fluid-solid mixtures are found in dredging calculations. To model the free surface interface there are a number of options. If the position of the interface is known or not complicated, an interface tracking method can be used. In these methods, the interface is taken into account by the same cells and threats the interface as a sharp boundary. The major disadvantage is the computational effort; in many interface capturing methods, the grid needs to be adapted to the free surface deformation, which might be costly.

Interface capturing methods do not have this disadvantage. These methods reconstruct the interface depedent on quantities in the cell and do not need grid adaptation. To reconstruct the free surface, the Volume of Fluids uses the quantity air volume fraction α. If a cell is full of air, $\alpha = 1$, and for water $\alpha = 0$. The free surface is then defined as the cells with $0 < \alpha < 1$. The fact that the interface might be captured in multiple cells and is not sharp, is one of the shortcomings of this method, due to the assumptions of the Volume-of-Fluid method that the discrete phases can be captured as a continuous phase. Discrete nature is neglected in and effects are approximated upon the continuous phase [3]. Quantities as density and viscosity are linear interpolated over α. Progression of α is governed by the transport equation of eq. (3.53).

$$\frac{\partial \alpha}{\partial t} + u \cdot \nabla \alpha = 0 \tag{3.53}$$

$$\rho(\alpha) = \alpha \rho_a + (1-\alpha)\rho_w \tag{3.54}$$

Free surface smearing is dependent on the free surface convective discretization term. Discretization using forward stepping, such as First Order Upwind (FOU) or Central Differencing (CDS) is in general leading to significant smearing due to numerical diffusion. Compressible schemes have been developed which do not suffer from this problem, such as SuperBEE and REFRICS by MARIN. REFRICS is a scheme which compresses in direction of largest pressure gradient and thus prevents smearing [36]. Backward stepping is used in the high resolution scheme in the other directions. Flux limiter SuperBEE compresses in all directions. SuperBEE is already used in ventilating flows [68], whereas diffusive schemes as FOU and CDS are still being applied in cavitating flows [51] for robustness reasons. The difference in free surface discretization schemes is found in fig. 3.7, which indeed shows the excessive smearing of upwind dscretization and the compressiveness of SuperBEE and REFRICS.

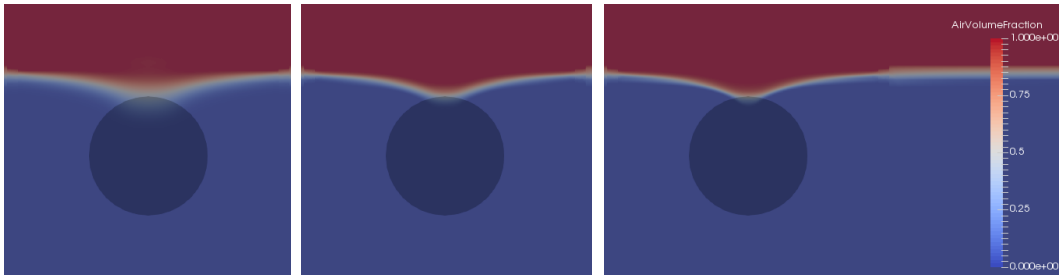

Figure 3.7: Different Free Surface Discretizations. From left to right: First Order Upwind, SuperBEE and REFRICS

3.2.5. Convergence and Errors

CFD is by definition an approximation of reality. The correct equations are to be modeled, which also has to be done correctly. Errors in using the wrong equations are called modeling errors. Validation of the model is here of importance; validation is the examination if the correct equations are solved. Physical experiments are necessary to make this comparison. The second part, solving the equations correctly, is verification. This includes code verification so that no bugs are apparent, but also the precision of the computer, decretization method and iterative processes are of influence on numerical errors. These numerical errors can be distinguised in three major categories; round-off errors, iterative errors and discretization errors.

An error e is the difference between the approximate solution ϕ_{num} and the exact solution ϕ_{exact} and has a sign. Uncertainty is closely related to that; uncertainty $U(\phi)$ defines an interval that contains the exact solution.

$$e = \phi_{num} - \phi_{exact}$$
$$\phi_{num} - U(\phi) \leq \phi_{exact} \leq \phi_{num} + U(\phi)$$

Round-off errors are errors due to the finite precision of a computer. These are in the order of $1E-14$ for a double precision machine and in general multiple order smaller than the other errors. Therefore solving to machine precision at high computational cost is, if even possible, in many cases not necessary.

The iterative error is the error made in solving the system of equations. Several contributions to the iterative errors are linearization of convective terms in transport equations (Picard of Newton approximation), segregated solvers, finite approximation order of discretization schemes and linearization of non-linear processes [53]. The size of the error is captured as the change between consecutive iteraton. It can be given in the L_∞-norm; the maximum changes in all cells or in the $L2$-norm; the root-mean-square of changes in all cells. In unsteady flow simulation, care should be taken to the iterative error, as this error is taken to the next timestep [17].

$$L_\infty = \max_N(|\Delta \mathbf{x}_i|) \tag{3.55}$$
$$L_2 = \sqrt{\frac{\sum_1^N (\Delta \mathbf{x}_i^2)}{N}} \tag{3.56}$$

Iterative convergence can be made more robust at the cost of more iterations by under-relaxation using implicit and/or explicit relaxation factors. Explicit relaxation factor stabilizes the convergence by only using a part ω_{exp} of the solution, at the cost of slower convergence (see eq. (3.57)). Implicit relaxation reduces the diagonal strength of the system and makes it easier to obtain the matrix inverse (see eq. (3.58)) . As this method changes the matrices, modeled physics is harmed by this method. In the starting calculation, the implicit relaxation is used, but decreased during the calculations. `REFRESCOs` default values are 0.25 for the starting value, to 0.975 in the end value in 100 steps. A slight adaptation of the matrix diagonal is still apparent.

$$u^{k+1} = u^k + \omega_{exp}(u^* - u^k) \tag{3.57}$$
$$\Big(Q + \frac{1-\omega_{imp}}{\omega_{imp}} dQ\Big) u^{k+1} = f + \Big(\frac{1-\omega_{imp}}{\omega_{imp}} dQ\Big) u^k - Gp^k \tag{3.58}$$

Lastly the discretization error exist. This error originates from approximating the geometry in a grid and separating continuous algebraic equations in space and time into discrete steps. The size of the error can be estimated by refining grids and/or timesteps and observing the convergence to an infinitesimal small step. Eca and Hoekstra described this method for spatial discretization [15]. A grid refinement study is conducted and presented in section 4.3.

3.3. Former CFD-work on ventilation

The ventilation phenomenon is attempted to simulate in three major applications; surface piercing foils by Harwood, Brucker, Miguel, Young, and Ceccio [25], surface piercing propellers by Himei [27], Yari and Ghassemi [85] and regular propellers (whether or not partially submerged) by Kozlowska et al. [45] and Califano [5] and by Paik [63].

Harwood et al. [25] were using a incompressible flow solver called *NFA CFD*, solving the Navier-Stokes equations in a cartesian grid formulation supported by sub-grid turbulence modeling. A second order accurate VoF-method was used, where every timestep the interface was reconstructed using piece-wise planar surfaces. A QUICK-threatment was used for all the convective terms. To enforce incompressibility, a multigrid Poisson solver is used. The two meshes consists of hexahedrals, varying in number of cells between 42M and 377M. For visualisation purposes,the interface is corrected by isosurfaces for a representation without holes and ridges. With regard to CFD of a vessel, a relatively bigger domain is necessary due to the tip vortex and leeway angle of the foil. Also ramp-up times to 10 times the convective time unit c/U_∞ and V-cycles, changes

between grids, are needed to model the tip vortex correctly. Once the tip vortex was established, the timestep is increased and the amount of V-cycles decreased.

Numerical and experimental results match very well. Both in lift, drag and moment coefficients, similarity is found, but also in the appearance of the flow field and formation of the aerated tip vortex. The similarity can be seen in fig. 3.8 and fig. 3.9.

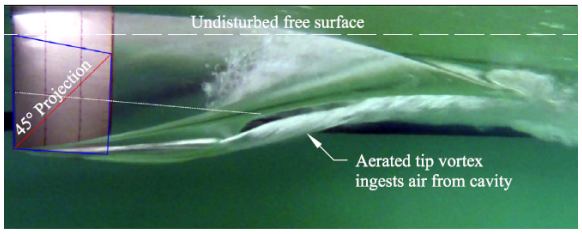

Figure 3.8: Experimental result of surface piercing hydrofoil, from [25].

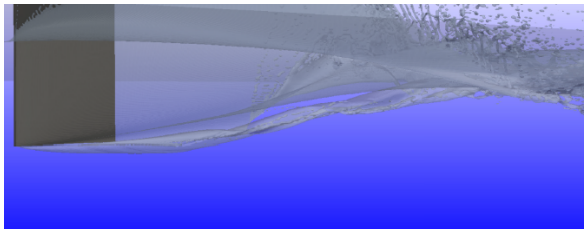

Figure 3.9: Numerical result of surface piercing hydrofoil in same conditions, from [25].

Himei [27] and Yari and Ghassemi [85] both did calculations on a surface-piercing propeller. The working principle and physical results of the studies are not of importance, but numerical settings might be of interest in the modeling of a submerged regular propeller.

Himei [27] used a VoF-method to capture the interface. All convective terms, including free surface equation, were discretized using a second order upwind scheme. $k-\epsilon$ turbulence modeling was applied. The flow is not resolved until the walls, $y^+ = 50$ and wall models were applied. A timestep corresponding to $1/10°$was used, such that CFL resulted to be smaller than 1. The grid was fully unstructured (also on propeller blades) and consists of 17M cells. It was found that K_T roughly followed experiments. K_Q was was overestimated, ascribed to oversimulated interface deformation. The obtained interface is fairly sharp.

Yari and Ghassemi [85] also used a VoF-method in the commercial RaNS-code `ANSYS-FLUENT`, supported by $k-\epsilon$ turbulence modeling. Discretization schemes are not listed. 2D-wedge calculations showed an extremely sharp interface. In the 3D-case, wall functions were applied with maximum $y^+ = 90$. An overset grid consisting of structured and unstructured blocks is used, consisting of 3.8M cells. It is said to be verified and 3.8M cells is said to be enough, but the author is sceptic about that. However, K_T and K_Q are mimicing experimental result fairly good. CFD results are showing slight underprediction of coefficients. Forces on a single blade are underestimated in all directions, due to incorrect simulation of ventilation attachment on the blades.

Not fully submerged regular propellers were part of the work of Paik [63]. The propeller was 5-bladed ($D = 250mm$, $A_e/A_0 = 0.8$ and $P/D = 0.95$), immersed at three depths: $h_{shaft}/R = \{0.0, 0.5, 1.0\}$ and four revolution rates: $\{2,4,6,8\}$ rps. `STAR-CCM+` was used, Pressure-velocity coupling was governed by a SIMPLE-algorithm. A VoF-model was applied for free surface capturing, supported by a sharpening factor regulating the reduction numerical diffusivity, which is tuned to 0.5. $HRIC$, a method blending *first order upwind* an *bounded downwind* dependent on CFL and pressure gradient, was used in the discretization of Free surface convective terms. Other convective terms were second order upwind discretized. The grid consisted of a structured propeller and a background grid of 1.58M and 5.30M cells. Local tip and root refinement is applied and care was taken such that $y^+ < 1$.

Results given in section 3.3 showed that extensive air drawing can be captured in CFD at bollard pull conditions. These conditions are however surface-piercing such that air may be drawn by momentum effects of the propeller breaking the free surface rather than a pressure gradient. Furthermore this is at bollard pull conditions so that air is lesser advected downstream, such that air can easily stay in the propeller area. In partially submergence conditions, air seems to be attached to the propeller, while in $h_{shaft}/R = 1$, this is reduced.

Numerical experiments on fully submerged regular propellers were executed by Califano [5], [8], [6] and Kozlowska et al. [45] in the research funded by Rolls-Royce, all in the free-surface ventilating regime. `ANSYS-FLUENT` is used for the viscous, incompressible, multiphase calculations. Multiphase modeling was taken into account via a VoF-method, where the transport equation is discretized according HRIC. Momentum equations are discretized using a second-order upwind scheme, pressure-velocity-coupling used the SIMPLE-algorithm.

The grid consists of rotating and stationary blocks. A structured grid was used in the rotating block, with

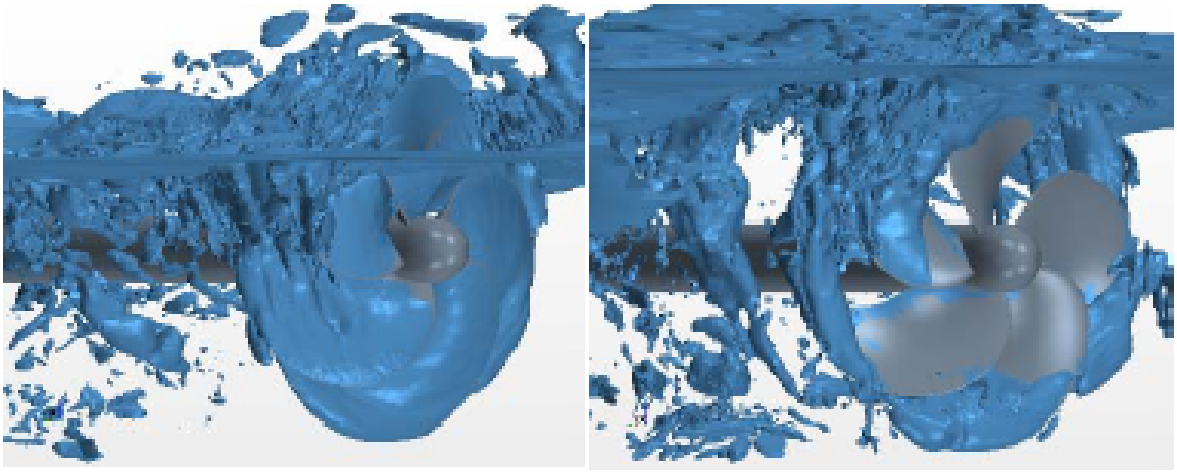

Figure 3.10: Air drawn by the propeller at $h_{shaft}/D = \{0.5, 1.0\}$ for $\alpha = 0.5$ at N=8rps at bollard pull conditions visualized by the contour of the air volume fraction.

a superimposed prismatic layer at the propeller walls to capture the boundary layer. Further cells are completely unstructured. The total amount of cells is 2.35 million, which gives a typical cell size of 5mm at the free surface.

Propeller rotation was archieved by a Multiple Reference Frame (MRF) model and by a Sliding Mesh model. The first model assumed the propeller to be fixed, while the propeller rotations is taken into account using a local, rotating reference frame. Equations are to be adapted to make this possible. A MRF-model is suitable when the interaction between stationary and moving parts are quasi-steady [8]. In a Sliding Mesh method, the grid consisting the propeller geometry is moving within the stationary grid with the propeller rotation rate. Quantities are interpolated between the adjecent cells, although the adjecent cell changes each timestep. This method allows unsteady interaction between the stationary and moving parts, and is therefore used in CFD-calculations, although it is more expensive.

Results showed an overestimation of thrust at all angles, except for the upright position. Thrust losses are underestimated by 50% with respect to experimental data, shown in fig. 3.11. fig. 3.12 shows the difference in air-advection along the rotation. Significant differences are the partly advection, as air is transported downstream in the numerical experiments. Also the formation of bubbles is not captured in the numerical experiments. Restrictive assumptions of the simulation are listed, being a short simulation time, absence of turbulence, absence of cavitation modeling, bubbly flow mechanics, compressibility and pressure drop.

In experiments, several ventilation modes have been found during the test, which takes significantly longer than the CFD simulated time. It may be that therefore agreement is not found. Turbulence is shown not to play an important role in the thrust loss, as free surface deformation is mostly due to pressure forces exerted from the body. However, turbulence is important in separation of flow, which might play a role in ventilation. Cavitation is shown to influence ventilation by Van Beek and Van Terwisga [75] and Brouwer and Hagestein [4]. Cavitation might introduce stable separation areas which can be filled after contact with air. Bubbly flow is not expected to be captured as the grid is not fine enough. These are diffused in the VOF-method.

The pressure drop from pressure to suction side shows a major difference in fig. 3.12. In experiments, a sheet of air on the suction side can be found, whereas in numerical experiments, only a part of the suction side is covered. This indicates that air reaching the surface is insufficient or that air remains confined around the tip, instead of advection along the blade. Both mechanisms assert that the pressure drop is insufficient; either between the blade and free surface, or locally on the suction side. In the latter case, turbulence is expected to be of importance. However, in the scale of the propeller, where laminar-turbulent transition will occur, this can not be solved adequately. Mesh refinement will increase the resolution and probably decrease the underestimation. Insufficiency in air suction between the free surface and propeller blade is expected to be caused by the grid, which does not allow to draw a vortex to the free surface big enough to draw air. These vortices are in the order of 3 mm and require a fine mesh of at least 10 cells in the diameter [44], but probably

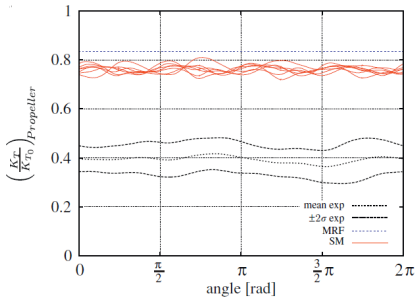

Figure 3.11: Underestimation of CFD w.r.t. experiments of 50%, from [8]

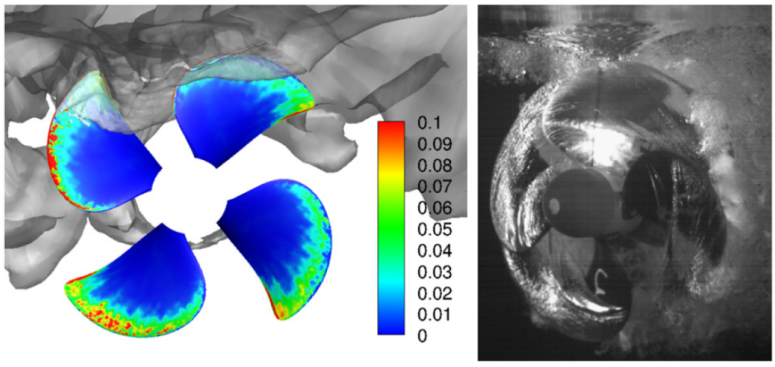

Figure 3.12: Visual difference between CFD and experiments, from [8]

more [1]. The cell size used is far from sufficient, and also the CFL-number was locally to high for HRIC to correctly solve the free surface equation. Kozlowska et al. [45] even speaks about the inability to resolve the ventilating vortex in RANS-VoF calculations.

4

Preliminary computational research

4.1. Propeller-free surface vortex

A ventilating vortex might be a source of air in ventilation. The extend in which a vortex is possible to model, is unknown. A short assesment was done to indicate the ability to model a vortex. This was done by placing a horizontal acuator disk below a plate (mimicing a propeller-hull vortex). Using a horizontal actuator disk, not only the ability to model, but also the origin of the propeller-hull vortex could be assessed. Theories of Huse [28] indicated no need for a propeller to initiate a the vortex.

Calculations have been performed using `ReFRESCO`. The grid used can be found in fig. 4.1, which was fully cartesian. Refinement boxes were placed at the propeller plane and above the propeller in the vortex region. The latter refinement level led to a cell size of $5e-5m$ per cell, nearly corresponding to the indication that a vortex should be captured with at least 10 cells and a typical vortex size of 3.3mm [44].

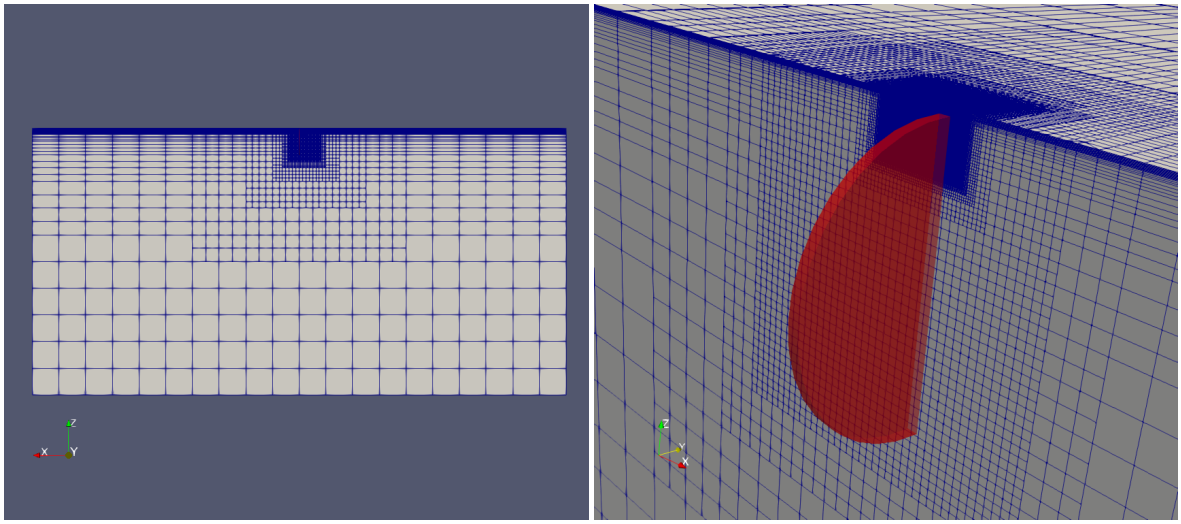

Figure 4.1: Grids used in the calculations of the propeller-hull vortex.

The actuator disk was modeled including and excluding swirl. Results were equal. Comparable to the research of Martio et al. [54], limiting streamlines were used to find the vortex. Results are shown for multiple thrust loadings, higher than the loadings used by Sato et al. [70] and Martio et al. [54]. At the thrust loadings used in literature, no vortical structures were found. This indicates that an actuator disk's axial thrust is only part of the vortex initiation. Rotational wake and vorticity from the propeller body is expected to be of influence as well.

Comparable to Sato et al. [70] flow regimes in fig. 2.19 were found for higher thrust loadings, shown in fig. 4.2 till 4.5. The fore flow vortex at small thrust loading coefficient moves backward for increasing thrust loadings.

In between, the double flow vortex in indeed found. Velocity, varied in fig. 4.2 and fig. 4.3, did not show a strong influence on the limiting streamlines and vortical structures. Low pressure in the vortex could not be captured, even when a laminar calculation is performed and Boussinesq's assumption is not used.

As the propeller vortex and low pressure is not found in these calculations, it is not expected to find these vortices in the multiphase calculations either.

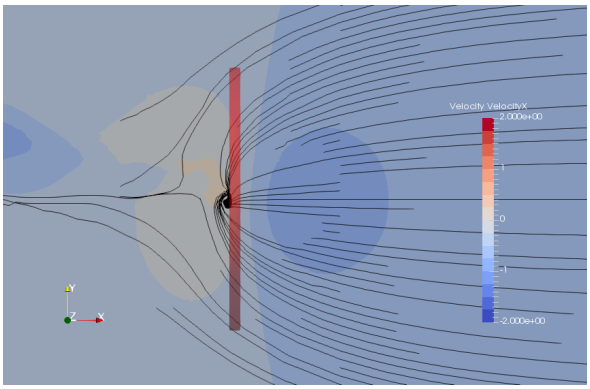

Figure 4.2: Aft vortex flow for C_T=40 and h_{tip}/D=0.09 at a lower velocity.

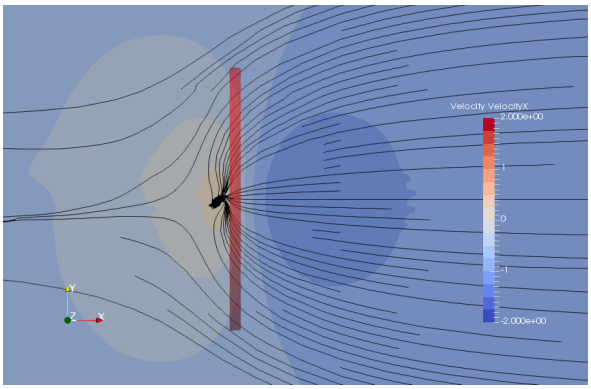

Figure 4.3: Aft vortex flow for C_T=40 and h_{tip}/D=0.09 at a higher velocity.

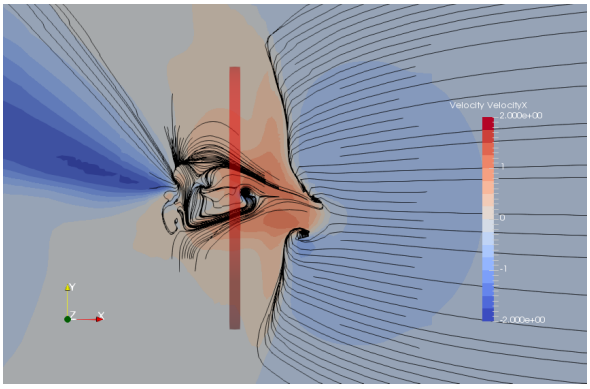

Figure 4.4: Fore vortex flow for C_T=80 and h_{tip}/D=0.09

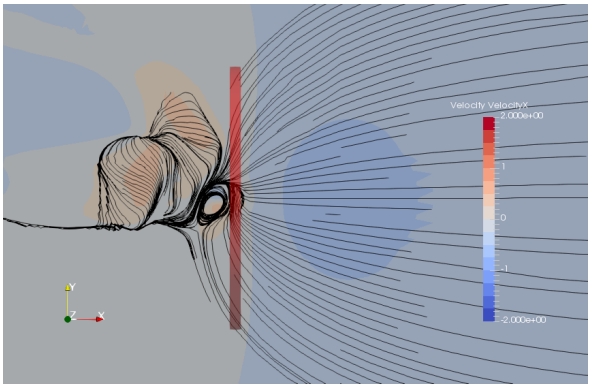

Figure 4.5: Aft vortex flow for C_T=132 and h_{tip}/D=0.15, which shows comparable vortical structures as fig. 4.2 and fig. 4.3.

4.2. Ventilating actuator disk

Preliminary computational research has been executed using an actuator disk, adapted for the use in ventilation phenomena. Goal of this part is to derive trends between the several non-dimensional parameters and the ventilation inception and thrust breakdown.

A basic theory of presenting a propeller is the actuator disk or momentum theory. In this theory, the propeller is modelled as a pressure jump over an area. No viscosity is taken into account, the model consists of only axial axisymetric flow and uniform pressure distribution for an infinite blade number. Application of Bernoulli's principle and mass conservation derives the ideal efficiency of the propeller only dependent on the thrust loading coefficient (and thus axial acceleration of flow).

$$\eta_{ideal} = \frac{2}{1+\sqrt{C_T+1}} \tag{4.1}$$

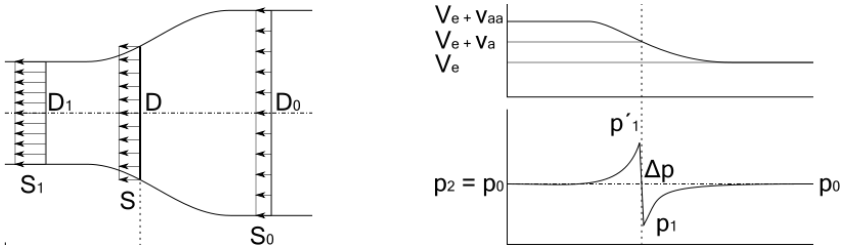

Figure 4.6: Schematic actuator disk, from [82]

4.2.1. Application of actuator disc theory in CFD

Application of the actuator disc theory in computational fluid dynamics is a cost-effective way of modeling a propeller because of the absence of a body in the flow. No adaptive or moving grids are necessary, a fully cartesian grid is sufficient to model the propeller force. Whereas the theoretical model knows aforementioned restrictions, some of these are solved by the way of implementing the disc.

Implementaton of the actuator disc in computational fluid dynamics will be done by means of applying volume forces on grid cells and taking these into account in the conservation of momentum, eq. (3.9). These force vectors can be radially and circumferentially varied, such that the restrictions of axisymmetry, uniformity and axial flow are no longer necessarily true. Summation over all cells of the integrated body forces in x-direction over the cell volumes gives the applied thrust.

Recalling the momentum equation of eq. (3.9), it can be derived that application of the momentum conservation on an air-filled cell gives a far overpredicted speed. So if the actuator disc starts to ventilate, the results are no longer (close to) valid. To adapt the model for ventilation purposes, body forces are made dependent on the cell local air-volume fraction α according eq. (4.3). The shape factor ASF is used to obtain a continuous function to improve numerical stability. This factor is set to 8, so a steep dependency of α exist such that force assigned to air-filled cells is nihil.

$$\mathbf{T} = \sum_{iCell} \int_{V_{iCell}} \mathbf{F}_{iCell} \cdot \hat{\mathbf{x}} dV \tag{4.2}$$

$$\mathbf{F}_{iCell} = \mathbf{F}_{iCell} \cdot (1-\alpha)^{ASF} \tag{4.3}$$

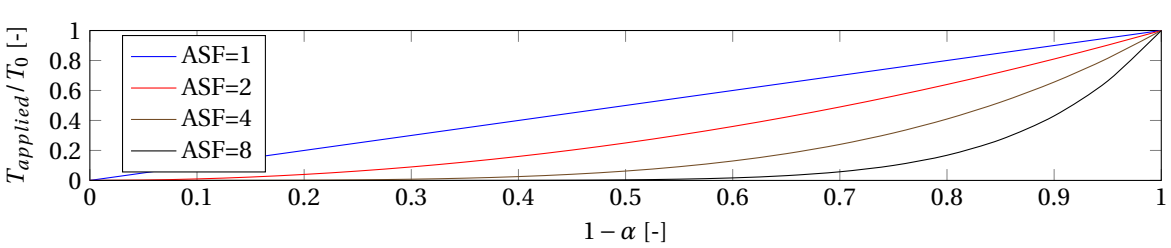

Figure 4.7: Applied thrust dependent on ASF

It is not possible to initiate the full thrust at once. If one does so, a servere acceleration is resulting due to the initially low velocity in the cell, leading to a steep wave. This is physically incorrect behaviour and so the thrust is built up in steps, typically 300, seen in fig. 4.8. After the full thrust is built up, the calculation converges to the reduced thrust when the velocity in the cell does not change anymore and power is constant. The instantanuous thrust loss is the difference between the required thrust in the ReFRESCOs controlfile and the calculated thrust in ReFRESCO after eq. (4.3).

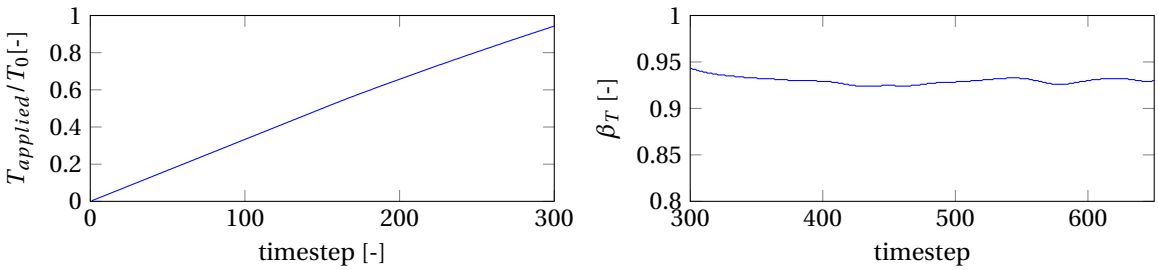

Figure 4.8: Relaxation in thrust build-up and breakdown.

4.2.2. Trends between non-dimensional parameters

Using the actuator disc, it was only possible to capture ventilation due to free surface piercing. Air was not advected along the propeller, as there was no body rotating. Rotation in the flow was not able to advect the air. Therefore thrust losses are smaller than found in literature [5].

All calculations were performed on the grid made using Hexpress and found in fig. 4.9. The grid consists of $0.5M$ hexahedrals, is unstructured and consists hanging nodes, but is fully cartesian. Around the actuator disk, two grid refinement boxes refining in three directions up to 6 levels were placed. Around the free surface, grid refinement in z-direction is applied, such that no hanging nodes are apparent in the z-direction.

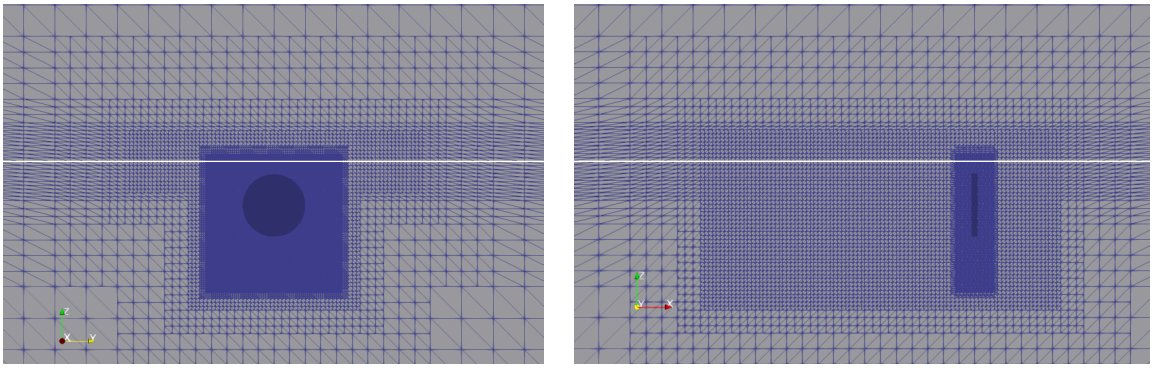

Figure 4.9: Cross sections of grid, left: YZ, right: XZ

The calculations were unsteady. Timestep of the simulation was $2e-3s$. Timestepping was taken care of by a three timelevel implicit method. The convergence tolerance for the inner loops was 1e-5, while the maximum inner loops was 200. In general, this was insufficient for convergence, although residuals were sufficiently low ($L_2 \leq 1e-5$). The convective term of the free surface equation is discretized using REFRICS. Other convective terms are discretized using Van-Leer's TVD scheme. Multiple combinations of in literature found parameters; thrust coefficient C_T, immersion depth I and ventilation number σ_V, as shown in table 4.1 were used. A list of calculations can be found in appendix D.1.

Table 4.1: Parameter range used in calculations.

	min		max
C_T	7		10
I	0.2		0.3
σ_V	0.05	0.10	0.15

Most severe thrust breakdown was found when the propeller was placed the closest to the waterline, at the highest thrust loading coefficient and lowest ventilation number. Nevertheless was this breakdown only 11.0 % of the nominal thrust. Fifure 4.10 shows the cross sections of the domain during ventilation of the propeller in two views.

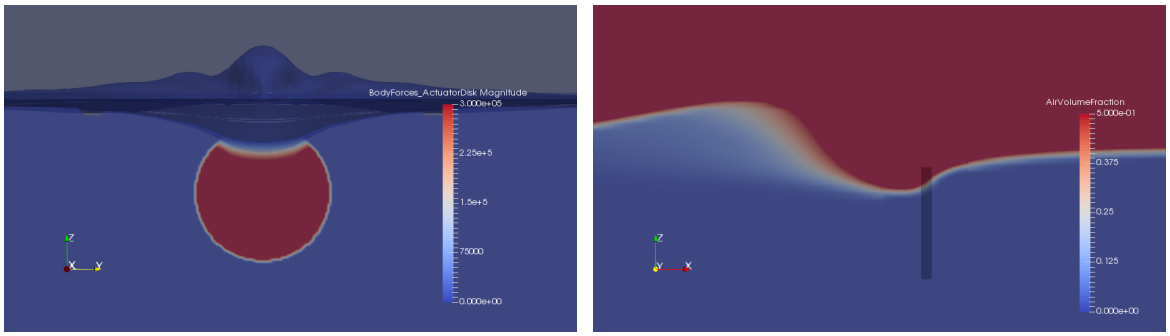

Figure 4.10: Cross section of AD-FSV for C_T=10, I=0.2 and σ_V=0.05.

In fig. 4.11 the thrust reduction can be found for the input parameters of table 4.1. Clear trends are found for the immersion depth I and ventilation inception number σ_V, whereas the trend for thrust loading coefficient C_T is smaller. As expected is thrust further decreased when the propeller is lesser immersed. Also a larger driving pressure, thus a lower ventilation number, seems to increase the thrust breakdown. With regard to thrust coefficient, the spreading becomes larger and thrust breakdown tends to grow with increasing thrust loading.

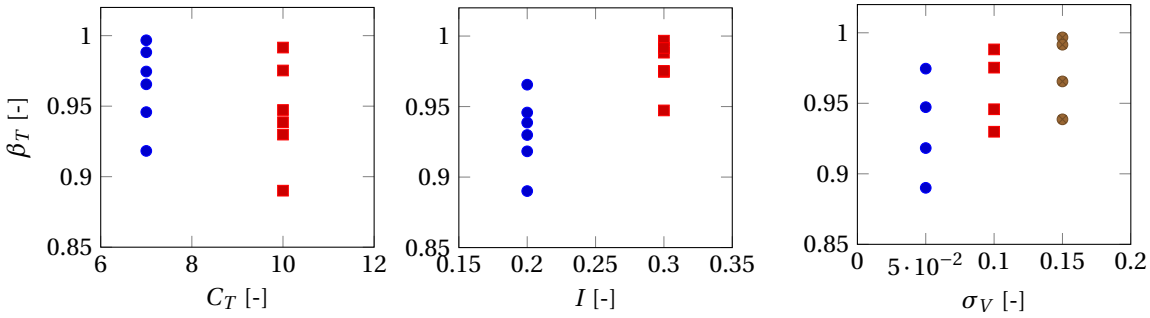

Figure 4.11: Thrust reduction of actuator disc due to three input parameters C_T, I and σ_V.

Calculations showed increasing wave steepness and breaking after the propeller. According to H. Raven, this phenomenon can be described by the Froude number, which is already been eloborated upon in section 2.4.1. In fig. 4.12, the change in wave steepness can be found. An increasing Froude number is indeed apparent between the cases.

Plotting thrust reduction against the Froude number Fr_{va} leads to fig. 4.13. These figures indicate a strong depencency on both the immersion depth I and ventilation number σ_V per Froude number. As both parameters show a clear distinction per Froude number, it also shows that the Froude number is a parameter needed to express the phenomenon. The left figure indicates a positive relationship between β and Fr_{va}. For the immersion depth, a similar shaped point cloud is visible per depth, where a larger depth shows lesser thrust reduction. A positive relationship between β and I is thus expected. The ventilation number shows three distinctive lines, all consisting of the comparable point locations. The trend between β and σ_V is positive as well.

Given the positive relations between the parameters w.r.t. β, it is expected that the free surface ventilation phenomenon can be captured in eq. (4.4). According the definitions, this equals eq. (4.5), which is also useful as C_T is explicitly part of the definition. The corresponding figure can be found in fig. 4.14.

$$\beta = f(\sigma_V \cdot I \cdot Fr_{va}) \tag{4.4}$$

$$= f(I^2/2C_T Fr_{va}) \tag{4.5}$$

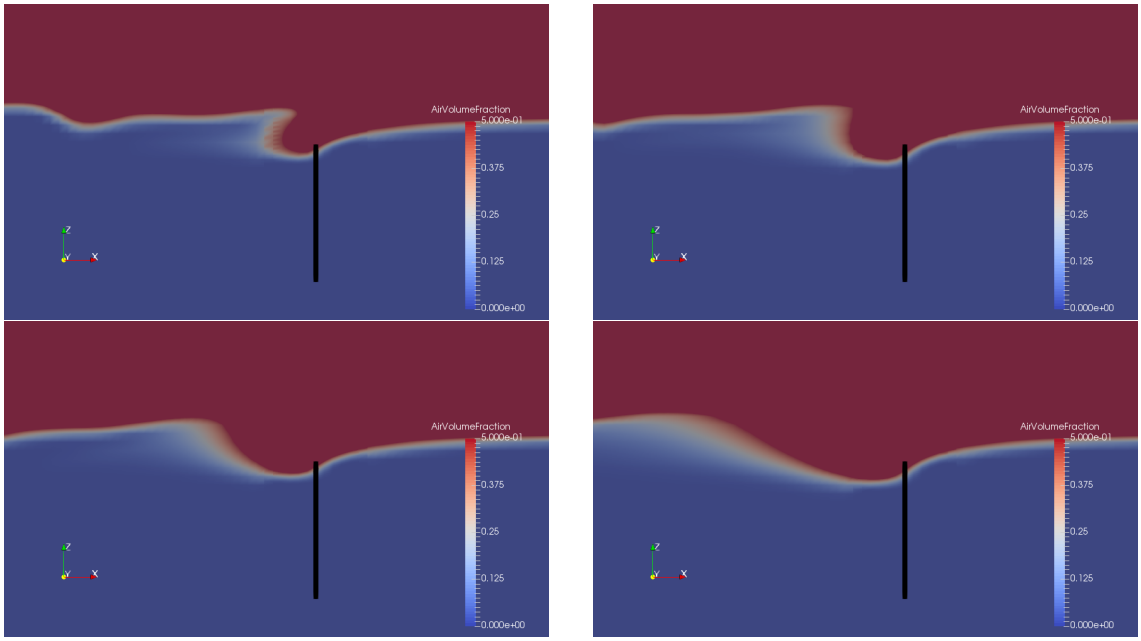

Figure 4.12: Wave steepness behind actuator disk dependent on Froude Number. Clockwise from left top: $Fr = 0.52, 0.63, 0.76, 1.07$

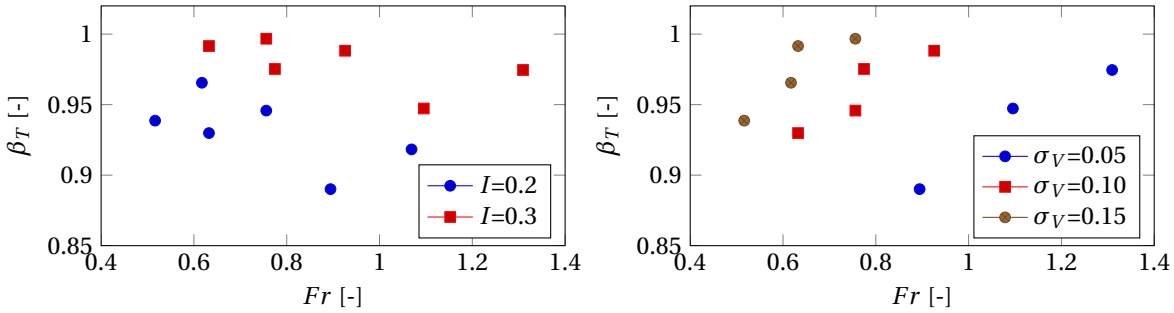

(a) β_T gathered by I

(b) β_T gathered by σ_V

Figure 4.13: β_T plotted against Froude number, gathered by the immersion depth and by ventilation number.

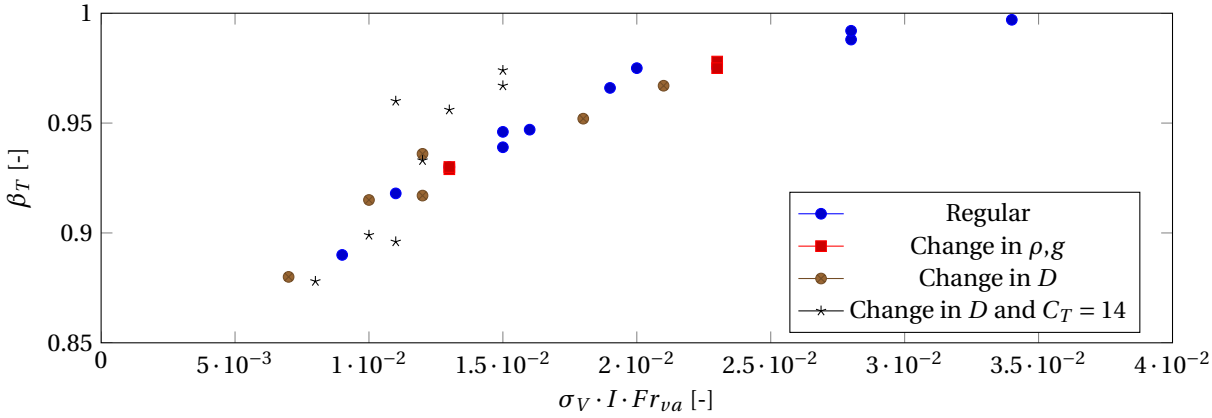

Figure 4.14: β_T dependent on $\sigma_V I Fr_{va}$. Note that in serie 'Change in D and C_T' values are not matching the curve. This is due to breaking waves into the disk area, leading to artificial thrust as been discussed before.

4.3. Propeller grid refinement study

Verification is not expected to be possible on the ventilating propeller, first of all because this research has an explorative character, but also regarding the computational effort of a verification study of an unsteady phenomenon. However, some verification is expected in this work, which was executed on the same propeller in open water conditions. The results can be used in an uncertainty estimation for the ventilating propeller. To diminish the computational effort, a frozen rotor approach is applied, similar to the verfication study of the B-series [57].

Frozen rotor or Absolute Formulation Method (AFM) calculations can be steady calculations. Mass and momentum equations of the Navier-Stokes equations are extended by the relative velocity of the inner grid with regard to the earth reference and solved in the moving reference frame. The solution is written in terms of the inertial reference frame. Application of a cylindrical domain gives the opportunity to use AFM on both frames and so capture the tip vortex in the outer domain as well. By `ReFRESCO` used equations are found below; in bold symbols, the difference w.r.t. the regular Navier-Stokes equations are highlighted.

$$\frac{\partial(U_i - \boldsymbol{U_{g,i}})}{\partial x_i} = 0 \tag{4.6}$$

$$\frac{\partial(\rho U_i)}{\partial t} + \frac{\partial}{\partial x_j}(\rho U_i(U_j - \boldsymbol{U_{g,j}}) = \frac{\partial}{\partial x_j}[(\mu + \mu_t)(\frac{\partial U_i}{\partial x_j} + \frac{\partial U_j}{\partial x_i})] - \frac{\partial}{\partial x_i}(P + \frac{2}{3}\rho k) - \rho\epsilon_{ij}\Omega_j U_k \tag{4.7}$$

4.3.1. Grids

The computational domain consists of a structured propeller domain inside an unstructured, cylindrical outer domain. Coupling of domains is governed by halo cells. By default, halo cells mirror the inner domain cell center into the outer domain and matches the closest outer domain cell center and vice versa. Equally sized cells are a necessity to apply halo cells correctly. Strechting in the boundary layer was equal.

The outer domain is cylindrical with a diameter and length of $2.75m$. Grids consisting of solely hexahedral cells are generated using `Hexpress`. Surface refinement to obtain $y^+ < 1$ on the torpedo body and cylindrical refinement around the torpedo of $0.15m$ diameter are applied. The inner propeller domain is cylindrical as well with a diameter $0.275m$ ($1.18D$), and a length of $0.30m$ centered around the propeller center. It is fully structured and hexahedral with refinement radially at the blade edges to capture the edge vortices and on the blade surface to ensure $y^+ < 1$. `GridPro` and a topology generator in `Rhino/Grasshopper` are used to generate the propeller grids, which were provided by B. Schuiling.

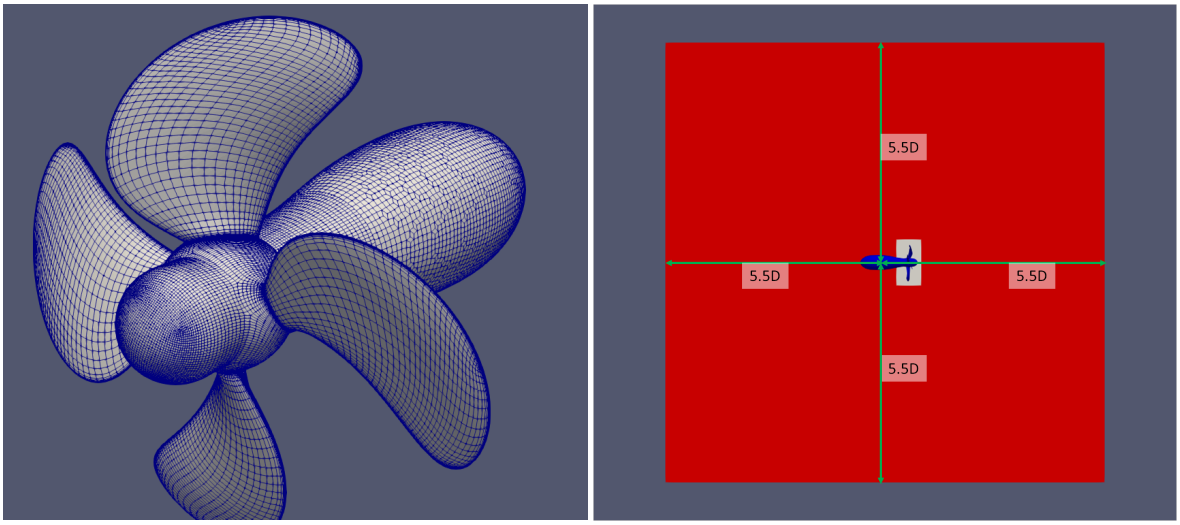

Figure 4.15: Axisymmetic body used in the grid refinement study and size of the circular domain around it. Results shown are for the coarstest grid for the sake of visibility.

Geometric similarity can perfectly be obtained on the inner structured propeller grid. Unstructured grids are known for their inability to obtain exact geometric similarity. This lack of geometric similarity is a main contibutor to noise in the data [16]. However, as the grid is fully structured in the propeller domain, the noise is foreseen to be small. Also for that reason, it is assumed that the grid density can still be represented by the typical cell size, as required in the procedure [16]. Furthermore research of Wieleman et al. [80] derived `Hexpress`-settings to obtain close to geometrically similar unstructed grids. Dependent on the grid refinement ratio, the diffusion factor for the coarsest grid is set, such that diffusion depths are equal. The number of cells in x, y, z-directions is also prescribed. Geometric unsimilarity is expected near trimmed corners and in circular grid refinement boxes. Visual inspection was necessary to review the similarity.

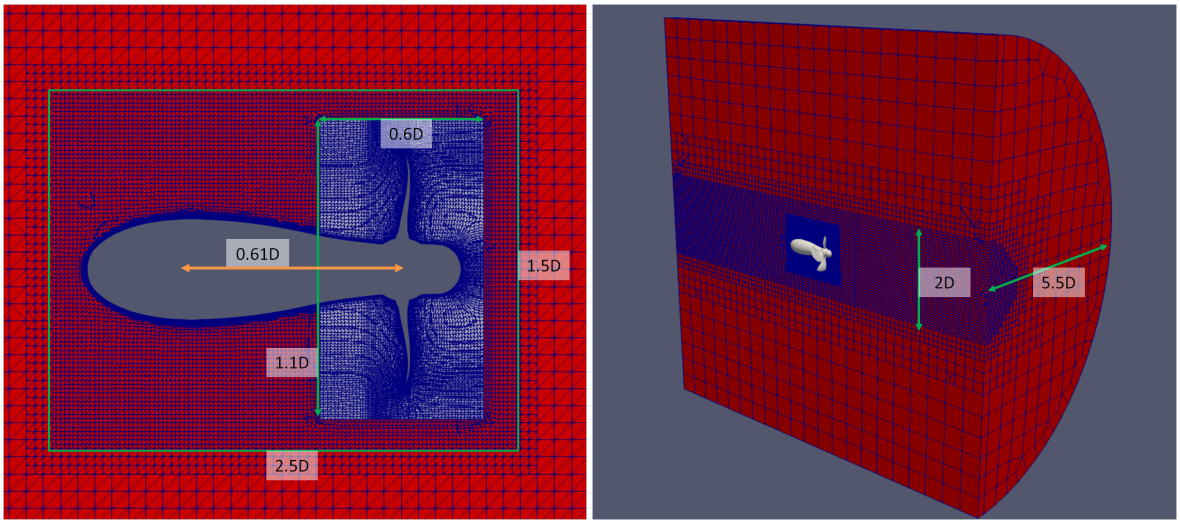

Figure 4.16: Refinement boxes in the grid. Note that this is the coarsest grid with the lowest diffusivity; finer grid have larger diffusivity and are so slightly larger.

A grid serie of 6 grids is used for the refinement study. The linear refinement factor between the coarsest and finest grid is 3 and grid refinement for intermediate grids is linear. In x, y, z-direction, a initial number of cells of multiple of 3 is needed, which has been set to 21 cells of $0.125m$. In section 4.3.1, the grid quantities are given. Comparison with the study of Merkens [57] indicate that these grids are in the asymptotic range.

Grid	0	1	2	3	4	5
Refinement factor	1	1.333	1.667	2	2.333	2.667
h_i/h_1	2.667	2.000	1.600	1.333	1.143	1.000
Diffusion factor	2	3	4	5	6	7
Farfield cell size	0.125	0.092	0.072	0.060	0.051	0.044
# Cells Inner grid [M]	0.9	2.2	5.4	12.2	17.8	31.5
# Cells Outer grid [M]	0.7	1.7	4.2	7.0	11.1	16.5
# Cells Total grid [M]	1.7	4.0	9.6	19.2	28.9	48.0

4.3.2. Calculation settings and iterative convergence

The propeller working point is $J = 0.25$, which is low and corresponds to propeller loading where ventilation may be found. A smaller advance ratio was not simulated as convergence problems were foreseen [57]. The procedure assumes sufficient iterative convergence to exclude this error component in the discretization error estimation. Second order schemes are applied in the discretization of the momentum and turbulence equation and Van Leer's flux limiter is used. The flux limiter may also be a source of scatter data according Eça and Hoekstra [16], altough it theoretically bounds the flux to be within the second order TVD region. Regarding the convective discretization schemes, second order grid convergence is expected. Turbulence modeling is done by application of the $k-\omega-TNT$ model of Kok [40]. Boundary conditions were set to BCInflow at the inflow, BCPressure on the cylindrical outer wall, BCOutflow at the outflow and BCWall on the propeller wall. The hub is coupled to the propeller w.r.t. the revolution rate.

The calculations runned until a steady force was obtained. Dependent on the simulations, up to 20000 iterations were necessary. In general, force convergence took more iterations than iterative convergence until stagnation. Stagnation was more often found in CFD calculations for high propeller loadings [57]. Iterative convergence behaviour can be found in section 4.3.2. Final values are listed in table 4.2 and force convergence is given in section 4.3.2.

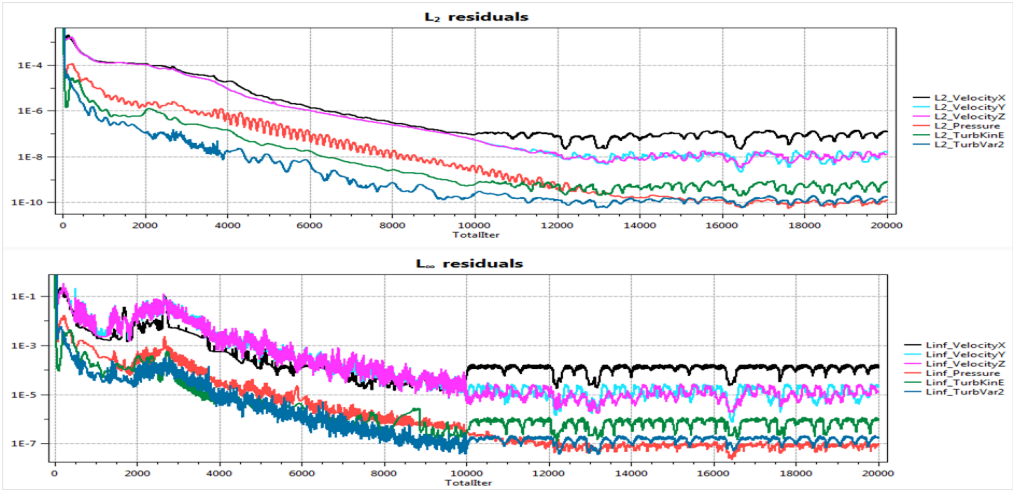

Figure 4.17: Typical iterative convergence in $L\infty$ and $L2$-norm. Stagnation is found in all converging parameters, in all grids. It corresponds to Merkens [57] at low advance ratios.

Table 4.2: Iterative convergence levels for various grids

	Grid	0	1	2	3	4	5
Velocity	L_∞	8E-03	1E-03	3E-04	1E-04	4E-04	2E-04
	L_2	6E-05	3E-06	2E-06	1E-07	5E-07	8E-07
Pressure	L_∞	2E-04	3E-06	1E-05	1E-07	1E-06	6E-07
	L_2	1E-06	1E-08	1E-08	1E-10	2E-09	2E-09
Turb.kin.E.	L_∞	2E-04	3E-06	5E-06	1E-06	1E-06	7E-07
	L_2	1E-06	1E-08	1E-08	7E-10	4E-09	2E-09
Turb.diss.	L_∞	2E-05	3E-06	6E-04	2E-07	2E-06	1E-06
	L_2	1E-07	1E-08	5E-07	1E-10	2E-09	3E-09

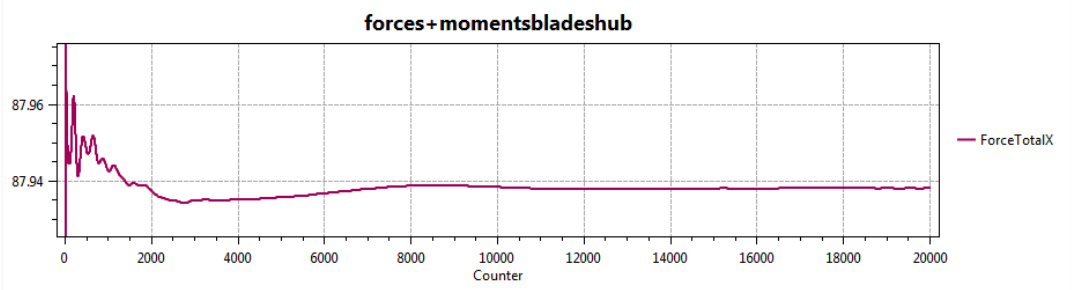

Figure 4.18: Force convergence.

4.3.3. Results and grid convergence

CFD-results are listed in table 4.4. Values listed are monitor data from 4 blades and hub, averaged over the last 3000 iterations when thrust and torque is sufficiently converged. It can be stated that K_T- and K_Q-values are accurate on the 5^{th} decimal. Using this data, the grid convergence study as described by Eça and Hoekstra [16] is applied using MARIN's program `uncertainty`. Results are shown in fig. 4.19.

Grid	h_i/h_1	T	Q	K_T	K_Q
5	1.000	87.88970	2.542850	0.297886	0.036999
4	1.143	87.93810	2.543680	0.298050	0.037011
3	1.333	87.95300	2.543270	0.298101	0.037005
2	1.600	88.03330	2.545620	0.298373	0.037039
1	2.000	88.03010	2.545600	0.298362	0.037039
0	2.667	88.20810	2.559021	0.298966	0.037234

Table 4.3: CFD results of the grid study.

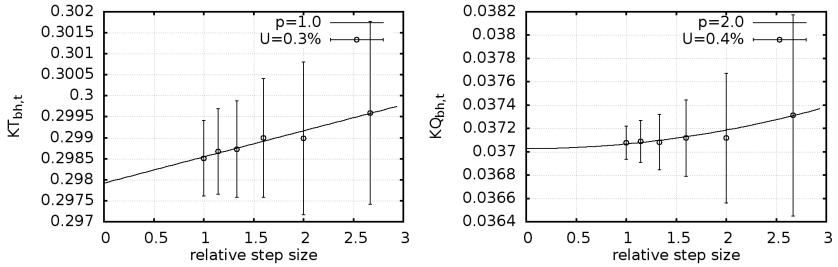

Figure 4.19: Grid convergence for K_T (left) and K_Q (right).

For the torque, the grids converges quadratically as expected. However, as shown, the thrust converges linearly. It is tried to trace which component is responsible for incorrect convergence in fig. 4.20. It is found that the convergence behaviour of only the blades shows an equal trend (fig. 4.20(a)). If the force is separated in the friction and pressure components, it is found that friction force is (nearly) second order converging (b) and pressure force is (nearly) linear (c). The same separation for the torque showed both quadratic convergence.

In the work of Merkens [57], also a lesser order of convergence is found for higher loaded propellers. This was ascribed to insufficient iterative convergence. Work of Eça, Vaz, and Hoekstra [17] showed that iterative errors of these orders can indeed give an seemingly correct grid convergence, while this actually due to insufficient iterative convergence. An other option is that grid densities are simply not high enough to properly simulate the pressure forces and separation associated with highly loaded propellers, but does properly simulate the friction forces. If the latter would be the case, the same grids should show a proper second order convergence at nominal working points, which is the case in the work of [57].

Furthermore v.d.van der Ploeg [76] reseached grid convergence depencency on the interpolation method and grid size. Larger grids showed a lower order of convergence for the pressure and velocity gradient for certain corrections and face interpolation schemes. Per default, face interpolation is governed by`FACEPOINT`, a method correcting for eccentricity and non-orthagonality. This method is the most accurate and could obtain higher orders of grid convergence. A more robust and formerly default method is `INVERSEDISTANCEPOINT`, which is only correcting for eccentricity. Especially convergence for grids with hanging nodes (`Hexpress`-grids) are benefiting from eccentricity and non-orthogonality correction instead of only eccentricity correction. However, `FACEPOINT`-interpolation showed robustness problems and thus the more robust `INVERSEDISTANCEPOINT` was used, at the cost of accuracy and lower order of grid convergence. To derive a conclusion, the grid refinement study should be repeated on the nominal work point, even finer grids, supplemented by study regarding interpolations correction methods.

Assumed second order grid convergence

Eça and Hoekstra [16] are suspicious in assuming a second order grid convergence when flux limiters, unstructured grids and blending turbulence models are used. Although the fact that Van Leer's flux limiters were applied (which are theoretically still second order TVD) and an unstructured outer domain (which is assumed not to influence the inner domain) was used, an uncertainty analysis assuming the second order grid convergence was performed, according the appendix of [15]. The weighted approach is presented, although hardly difference was found with the unweighted approach. Results show that a second order fit does still give proper results in terms of the resulting low value for the uncertainty. The weighted approach gives $\phi_0 = 0.2981$.

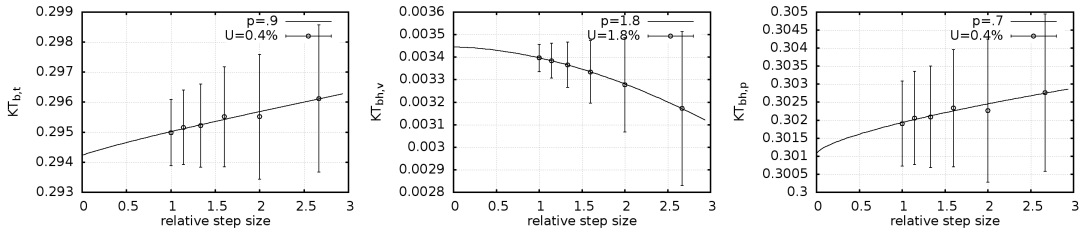

(a) total force on only blades (b) friction force on blades and hub (c) pressure force on blades and hub

Figure 4.20: Grid convergence for subparts. Pressure component (right) does not converge well.

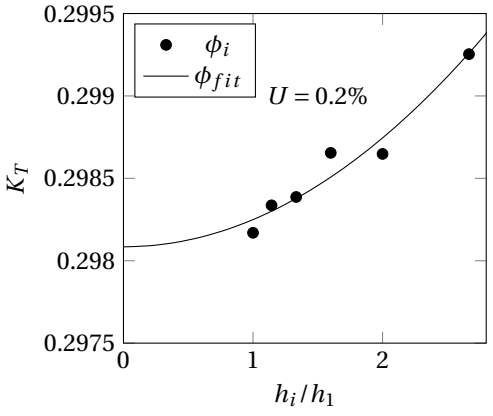

Figure 4.21: Assumed quadratic fit

Table 4.4: Results for assumed second order grid convergence

	weighted	unweighted
ϕ_0	0.29810	0.29808
α	0.0001616	0.0001652
σ	9.819E-05	9.701E-05

Table 4.5: Numerical values of assumed quadratic fit

Grid	h_i	w_i	ϕ_i	$\phi(h_i)$	U[%]
0	1.000	0.242	0.29817	0.29825	0.13
1	1.143	0.212	0.29834	0.29830	0.12
2	1.333	0.182	0.29839	0.29838	0.13
3	1.600	0.152	0.29865	0.29851	0.19
4	2.000	0.121	0.29865	0.29875	0.20
5	2.667	0.091	0.29925	0.29926	0.22

4.3.4. Validation using experimental results

Numerical results extrapolated to $h_i/h_1 = 0$ are expected to meet the experimental results (corrected for the experimental uncertainty interval). If so, the model is not only verified, but also validated. Validation is the assessment in what extend the correct equations are used. Based on fig. 4.21, experimental values at $h_i/h_1 = 0$ of $K_T = 0.298$ and $K_Q = 0.0370$ are expected. It should be noted that CFD and experimental geometry was not equal; in CFD, the strut was (for the sake of computational effort) not modeled.

In this study, the experimental and input uncertainty interval is assumed to be 1%, although it is questionable if this low value is a good estimate. Large differences might occur depending on i.a. the exact placement of the blades on the hub and so lack of geometric similarity. Also water conditions (perfectly still vs. slightly moving) and sensor noise might be influencing the uncertainty. However, as many of these components are unknown and thus any other uncertainty estimate is still guessing, it is decided to accept the 1% uncertainty level.

The experiments showed values of $K_T = 0.320$ and $K_Q = 0.0380$. As $K_T = 0.298$ is not within $0.320 \pm 1\%$, the model is not validated for K_T. For K_Q, the obtained value of 0.0370 is also not inbetween the experimental uncertainty band of $0.0380 \pm 1\%$. The difference between experimental and numerical values is 6.9% for K_T and 2.6% for K_Q. Validation uncertainty, defined as in eq. (4.8), is 1.08% for K_T and 1.02% for K_Q assuming that input uncertainty is 0. These values can also be found in table 4.6.

$$U_{val} = \sqrt{U_\phi^2 + U_{input}^2 + U_{exp}^2} \tag{4.8}$$

Table 4.6: Validation data

	numerical	U_{num}[%]	experimental	U_{exp}[%]	U_{val}[%]	% diff. wrt exp
K_T	0.298	0.4	0.320	1.0	1.08	6.88
K_Q	0.037	0.2	0.038	1.0	1.02	2.63

4.3.5. Comparison of AFM to MVG propeller computation

This verification study consists of steady frozen rotor calculations. However, ventilation calculations are unsteady calculations, using moving grids. An unsteady calculation was performed to assess the difference between frozen rotor and moving grid calculations and to assess the amount of outerloops necessary for sufficient force convergence. Force convergence results are shown in section 4.3.5. One can conclude that 250 outerloops is sufficient; probably 150 outerloops is sufficient to obtain an acceptable converged force. in this open water case. 150 outerloops might still be insufficient in the ventilating propeller due to complex two-phase flows. However, it is significantly lower than the outerloops necessary for the steady calculation, most probably due to stronger diagonal strength of the momentum matrix. An averaged value over 500 timesteps of $87.97N \pm \sigma = 0.044N$ is found (section 4.3.5). This is slightly higher than the value found for the steady calculation at grid 3; $87.93N$. Difference between steady and unsteady calculations is small.

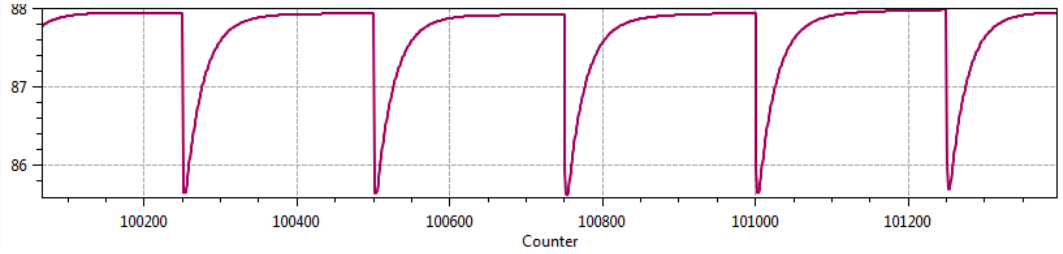

Figure 4.22: Force convergence for unsteady calculations.

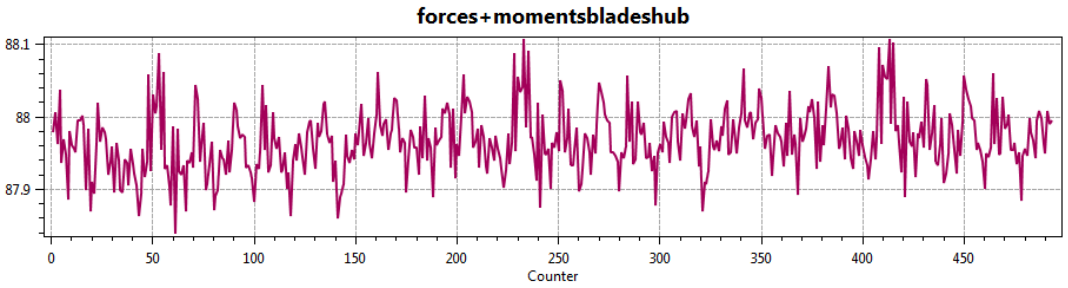

Figure 4.23: Unsteady force trace.

4.4. Chosen turbulence model

Three turbulence models were briefly evaluated on the computational set-up and grids used in the verification study; $k-\omega$-TNT [40], $k-\omega$-XLES [41] and $TNT-EARSM$ [14]. Computations were unsteady with a timestep corresponding to 0.5°propeller rotation. Based on results of Pereira et al. [64], $TNT-EARSM$ was forseen to be the most accurate in resembling the tip vortex pressure. $k-\omega$TNT-XLES was forseen to be the least diffusive and so giving the longest lasting tip vortex. Both characteristics might be of importance in modeling ventilation adequately.

Figure 4.24 shows results for the pressure in the tip vortex. $EARSM$ shows the lowest pressure and the highest resolution in the core, as expected. XLES and RaNS shows a nearly equal pressure, which is expected as XLES is still in RaNS-mode near the blade, see fig. 4.25 (left). Tip vortex pressure near the blade is thus not simulated using LES, but modeled using RaNS. Except for the blade, the domain is in LES-mode, inidcated as the blue regions in fig. 4.25. Figure 4.26 shows the extent of the tip vortex. Here it is clear that XLES indeed gives the longest tip vortex, followed by $EARSM$ and lastly RaNS. This result is expected.

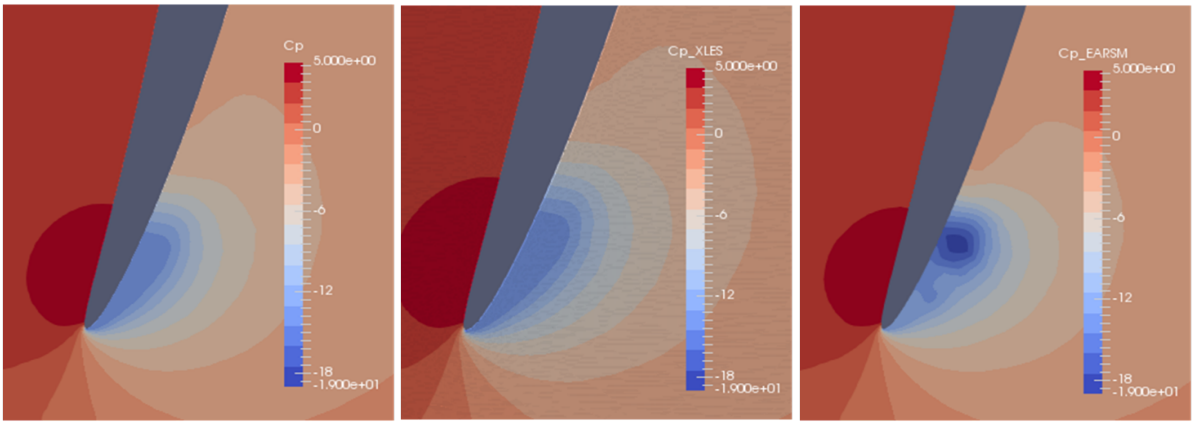

Figure 4.24: Comparison of low pressure in the tip vortex. Left is RaNS, center is XLES and right is $EARSM$.

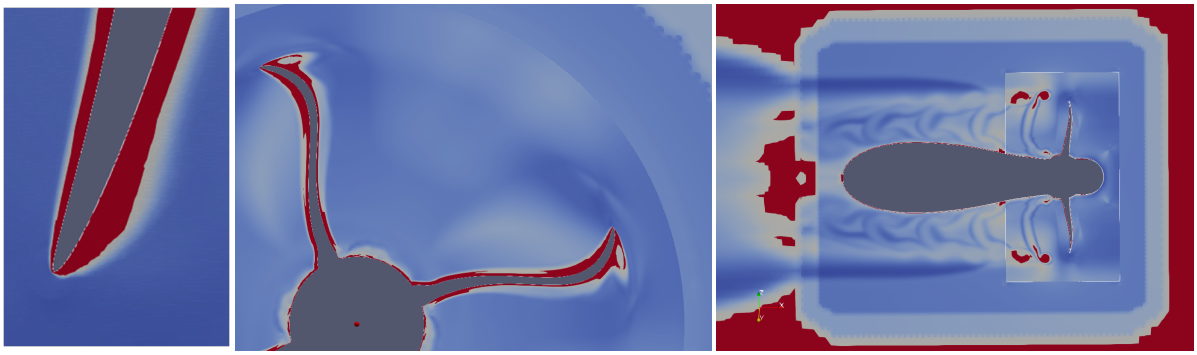

Figure 4.25: Application of RaNS/LES near the propeller for grid 3. Red coloured areas are LES-areas, blue coloured RaNS. Note that the maximum cell edge length in the farfield is determining RaNS/LES. A fully LES-propeller grid had not been made.

$k-\omega-TNT-XLES$-turbulence modeling/simulation and $TNT-EARSM$- turbulence modeling both show interesting differences with regard to the baseline $k-\omega TNT$-model. Therefore all three turbulence models were used in the ventilating propeller case. However, XLES appeared to be unapplicable as the for convergence necessary omega-limiter prevented the model to change to LES-mode close to the blades, see fig. 4.27.

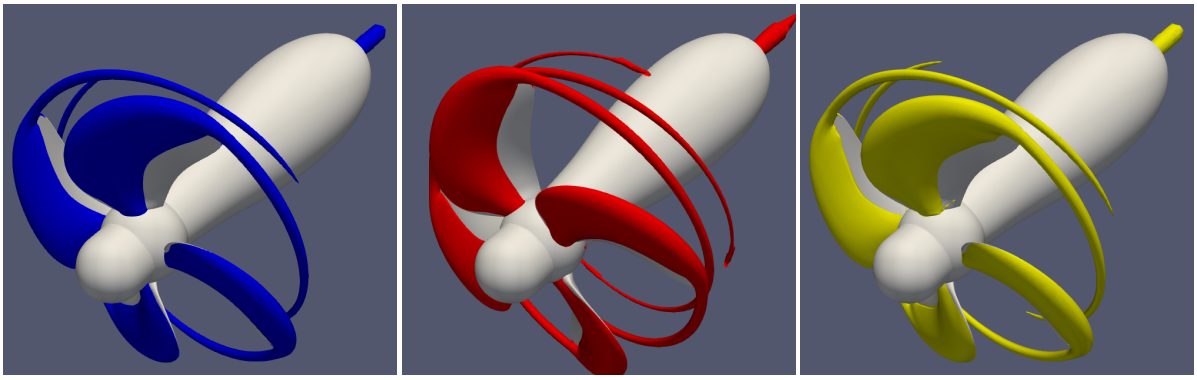

Figure 4.26: Comparison of extension of tip vortex using the contour of the pressure coefficient of -2. Left is RaNS, center is XLES and right is *EARSM*. XLES shows the longest tip vortex, followed by XLES and then RaNS.

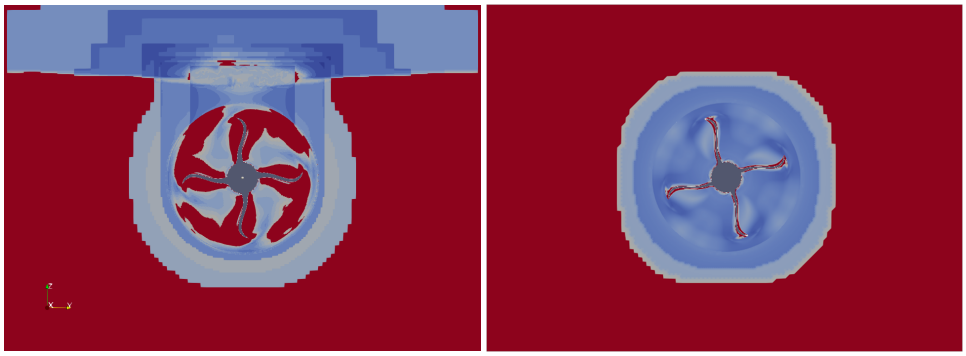

(a) Ventilation/multiphase calculation (b) Open water/single phase calculation

Figure 4.27: XLES-regions in the ventilating calculation. It can be found that the areas around the blade stay in RaNS-mode due to the omega-limiter.

4.5. Multiphase modeling in a rotating domain

To simulate the rotation of the propeller, frozen rotor calculations are not suitable as the ventilation phenomenon is too dynamic [5]. A moving grid (MVG) approach is applied. Each timestep, the inner grid rotates in the outer grid. All quantities stored on the inner grid are thus rotated, so water is displaced implicitly by the rotating the air-volume fraction. Halo cells are being used for the transfer of quantities over the grid boundaries, although these are reconstructed each timestep. First order interpolation of quantities is applied. An empty domain rotating through the water surface at low convective speed is simulated. The water surface should remain straight after sufficient convergence. This assessment is used to indicate the ability and requirements of the free surface discretization scheme, grid density, timestepping and iterative convergence to obtain a straight horizontal water surface.

Superbee's TVD scheme showed to be slightly more diffusive than REFRICS, which is in accordance with fig. 3.7. Furthermore it is known that SuperBEE may obtain a wavy free surface, although REFRICS showed this behaviour at high rotation angles and coarse grids due to the multi-directionability dependency on the pressure gradient as well, see fig. 4.29 (32 °at 4°/dt).

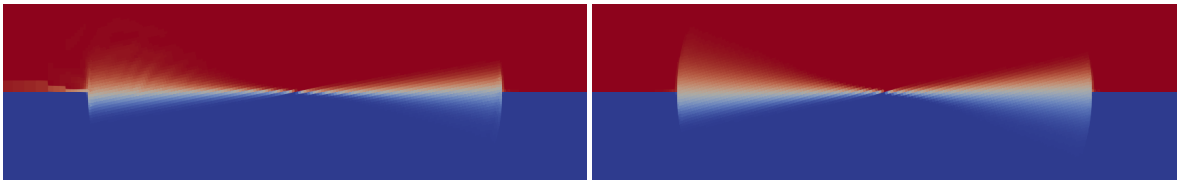

Figure 4.28: Comparison between ReFRICS (left) and SuperBEE (right) for a total rotation of 16°at 2°per timestep.

Timestepping was forseen to be not of importance as long as the amount of outerloops would be sufficient to obtain a straight free surface each timestep. However, iterative convergence of the air-volume fraction showed stagnation after 200 outerloops at L_2=0.1, while the free surface was not converged to a straight line yet. In fig. 4.29, one can see that the free surface is diffusing over time, with hardly influence of the rotation angle per timestep. Only for high rotation angles, slight differences are found. For higher rotation angles ($\geq$ 32 degrees), no changes were found w.r.t. the 32 degree situation. When observing ventilation results, one needs to take this free surface diffusivity into account. Better results are expected if the residuals are not stagnating at this insufficient level.

Grid refinement was shown to be a good manner of reducing free surface diffusivity in free-falling lifeboat simulations. However, a finer grid did not show smaller diffusivity angles in this assesment. One can see that fig. 4.28 (left) does hardy difference from fig. 4.29 at (2°/dt,8 °).

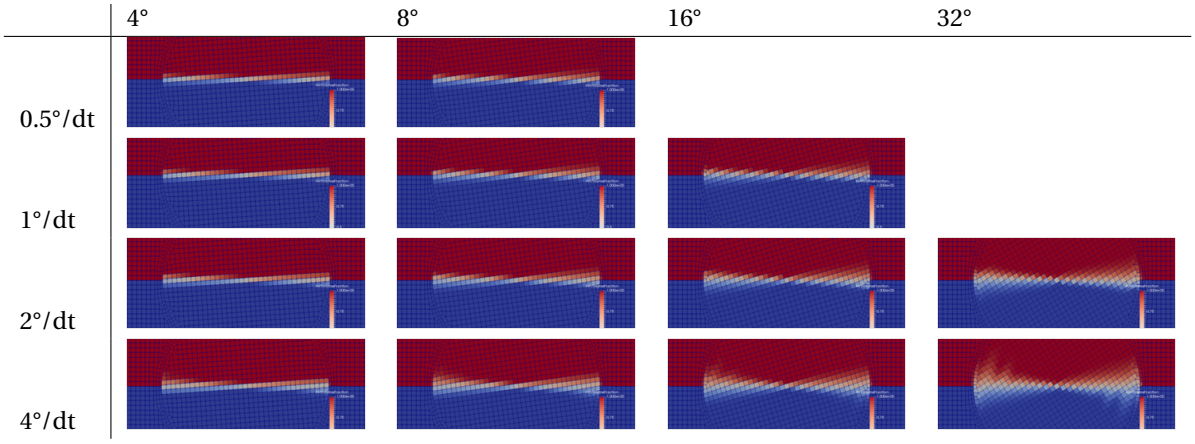

Figure 4.29: Free surface in rotated grid at various rotation rates and total angles.

Lastly is seems that data is not transferred over the grid boundaries, even if the most robust settings (`nearest-cell`, first order interpolation) and equal grid sizes at the boundary are used. Lemaire [50] found this behaviour if the interpolation order was equal or smaller than the discretization order. Increasing the interpolation order to 3 by i.g. a least squares polynomial interpolation only slightly improves the quality of interpolation at the cost of excessively more overhead. For the sake of time, within this assesment it is decided to accept this artifact and keep an eye on the grid boundary interpolation in the ventilation calculations. It is however foreseen that increased convective velocity solves part of this problem as transfer of quantities over the grid boundaries is also happening by convection, instead of only interpolation.

5

Experimental research

5.1. Preparation

5.1.1. Experimental setup

Experiments were performed at the depressurized wave basin (DWB) [52] of MARIN in Ede in collaboration with other internal MARIN projects. The tank is 240m long (of which 190m can be used for measurements), 18m wide and 8m deep. Ambient pressure can be reduced to 2500 Pa, although depressurized conditions were not applied in this part of ventilation research. Wave-makers are installed along the short and long side of the basin, but these were neither used. The tank is widely used for cavitation research, propeller noise research, wave impact forces and phenomena where scaling of entrapped air pockets is of importance. The aim of the partnering study is to identify the hysteresis effects of ventilation in characteristic wave period timescale and of depressurized conditions. [10]

The pulling propeller was mounted on a hexapod 6 DoF-frame. An electrical motor drives the propeller through an angled 47:19 gearbox in the propeller pod. Geometry of the pod and propeller hub were made specifically to fit to the hexapod frame necessary in the second part of experiments. No fairing around the circular strut was placed as preliminairy experiments showed no need. Underwater video was obtained at 25 Hz in high definition standards and the propeller was painted blue for the sake of clear video. In the propeller axis, a 6-DoF force and moment transducer was placed. Data acquisition took place at 1000Hz and was transferred using telemetrics to prevent from measurement noise from carbon brushes. Filtering was taken care of by data scientists at MARIN, correcting for i.a. inequal mass distribution, eigenfrequencies and measurement/set-up noise.

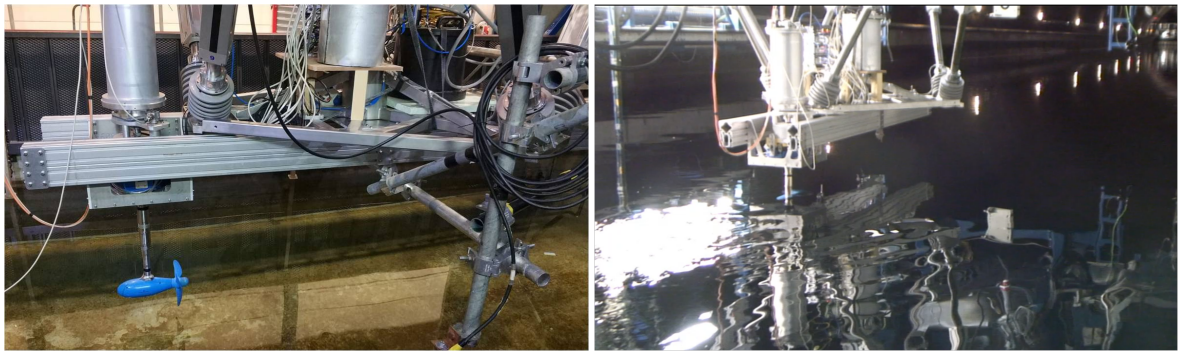

Figure 5.1: Experimental set-up

5.1.2. Quasi-steady approach

Experiments were conducted at constant rotation rate and varying carriage speed to obtain results for various advance ratios, as described by Lafeber and Dang [48] and succesfully conducted in cavitation experiments. Using this approach, a high degree of repeatability is found. The carriage speed will follow a cosine curve

found in fig. 5.2. A cosine curve for the advance ratio is then obtained as well. Reason to do so is the certainty to capture ventilation inception and the ability to obtain more ventilation data over a full open water diagram, both for inception and wash-out. This comes at the cost of not obtaining results of temporal influence of ventilarion at a single workpoint as been done in Califano and Steen [6]

Ventilation inception will follow immeadiately at the start of the experiment, as the propeller is highly loaded. In the acceleration of the carriage, ventilation wash-out will be found. The maximum speed of the carriage is such that the propeller is not loaded and any ventilation can wash out. During deceleration, ventilation inception will be found, as the thrust loading coefficient increases during the half-cycle. Maximum acceleration and decelaration is well below $0.1 m/s^2$.

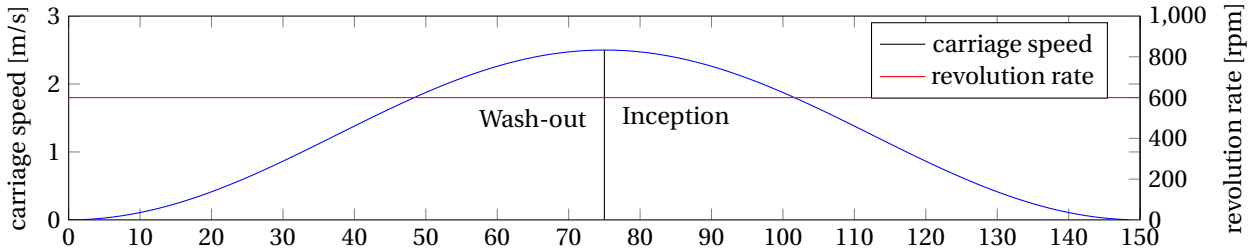

Figure 5.2: Carriage and revolution rate during quasi steady experiment

5.1.3. Design of experiments

Ventilation thrust breakdown is researched by experiments. A serie of four deep water reference tests were conducted to obtain a thrust which is not influenced by ventilation, but is influenced by a variation in Reynolds number as described in section 2.4.2. The difference between experimental data and reference data is the ventilation thrust breakdown, which is used in the empirical model. A surrogate model was built to interpolate results at the advance ratio of interest.

Between runs, revolution rate and immersion depth were varied. Parameter variations were derived from scaling of full scale propellers. In their application over the years, diameters are increasing and rotation rates are decreasing. A propeller of 12.5m at 56rpm was assumed as largest full scale propeller, which has not been found in the maritime sector (yet). The applicable scaling for this phenomenon is Froude scaling, of which applicable scaling laws can be found in section 2.4.2. This leads to a minimum model scale revolution rate of 400rpm. Maximum model scale revolution rate is 800rpm. Although this value is arbitrary, scaling analysis shows that within this range also smaller coastal vessels as the Damen Combi Coaster can be taken in account, which have a smaller propeller of 2m rotating at 250rpm [11].

These low revolution rates, which were inevitable due to the small propeller, result in Weber numbers below the required Weber number as deduced by Shiba [72]. This reduction can be as substantial as a Weber number of only 90 (instead of minimum required Weber number of 180) at 400RPM, so inception delay can be expected (see section 2.4.3). Only at 800RPM, the Weber number exceeds the required Weber number. Therefore, one must take in account that model test suffer from overpredicted surface tension compared to full scale and inception might be delayed.

Immersion depth range is based on former research in propeller ventilation and applicable immersion depths. Califano [5] showed that for highly loaded propellers, ventilation started for immersion I of 0.3 at advance ratios only at J=0.1 and lower. As in this research higher advance ratios were evaluated, the maximum immersion rate was set to 0.3. This corresponds to the minimum clearance between the propeller and hull according DNV [13] and may be found in ballast condition.

Based on results of Shiba [72], where ventilation was still delayed at an immersion rate of 0, this lower boundary is therefore also interesting and thus chosen. Partially submerged propellers were out of the scope in this research.

Combinations of revolution rate and immersion depth were obtained through design of experiments using `DesignExpert`. This method derives a set of input variables which correlate in a certain order, in which the results can be derived; for this research it is third order. A higher order was nor assumed to be necessary, nor possible regarding the experimental time and costs. All combinations of revolution rates and immersion depth can be found in fig. 5.4 and table 5.1.

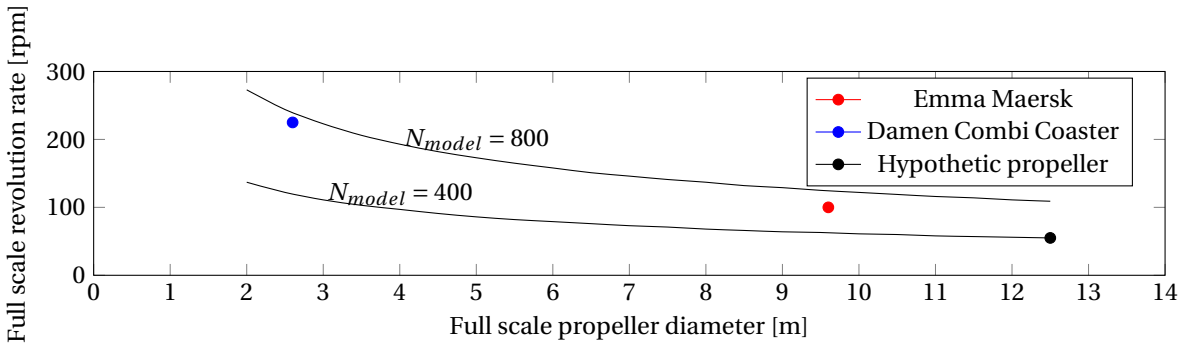

Figure 5.3: Full scale lower and upper bound of propeller experiments

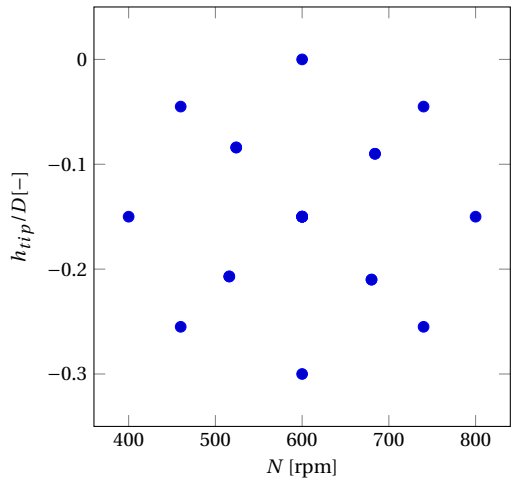

Figure 5.4: Design of Experiments

Table 5.1: Experimental tests, 'd' stands for deepwater reference

#	I [-]	h_{tip} [mm]	N [rpm]	$v_{a,max}$ [m/s]	measuring time[s]	a_{max} [m/s^2]
1	0.150	34.94	600	2.125	187	0.029
2	0.255	59.40	460	1.629	244	0.017
3	0.150	34.94	600	2.125	187	0.029
4	0.150	34.94	400	1.147	280	0.013
5	0.150	34.94	600	2.125	187	0.029
6	0.045	10.48	740	2.621	152	0.045
7	0.300	69.88	600	2.125	187	0.029
8	0.255	59.40	740	2.621	152	0.045
9	0.150	34.94	600	2.125	187	0.029
10	0.000	0.00	600	2.125	187	0.029
11	0.045	10.48	460	1.629	244	0.017
12	0.150	34.94	600	2.125	187	0.029
13	0.150	34.94	800	2.833	140	0.052
14	0.207	48.22	516	1.828	217	0.022
15	0.210	48.92	680	2.423	165	0.038
16	0.090	20.96	684	1.856	164	0.038
17	0.084	19.57	524	2.408	214	0.022
d	1.000	465.9	400	1.417	231	0.019
d	1.000	465.9	516	1.828	217	0.022
d	1.000	465.9	600	2.125	154	0.043
d	1.000	465.9	800	2.833	115	0.077

.

5.2. Experimental results

During the experiments, a HD camera was pointed at the propeller. These movies were used to distinguish the ventilation and inception regimes. With data from the 6-DoF sensor, severeness at the various inception and ventilation regimes could be assessed on thrust breakdown and predictability of the phenomenon. Also some hysteresis effects could be evaluated.

5.2.1. Thrust breakdown per ventilation regimes

Three ventilation regimes are shown in fig. 5.5. Also the thrust breakdown behaviour is given. From these three, it can be concluded that free surface ventilation incepts at the highest advance ratio and shows the largest thrust breakdown. The breakdown is fairly stable. Mixed ventilation is more unstable, and significant thrust breakdown may still occur. The most unstable is vortex ventilation. Thrust breakdown is hardly found, only when a vortex has enough capacity to exist, grow and draw air. On the other side, a (visually) large vortex does not necessarily lead to air ingress and thrust breakdown.

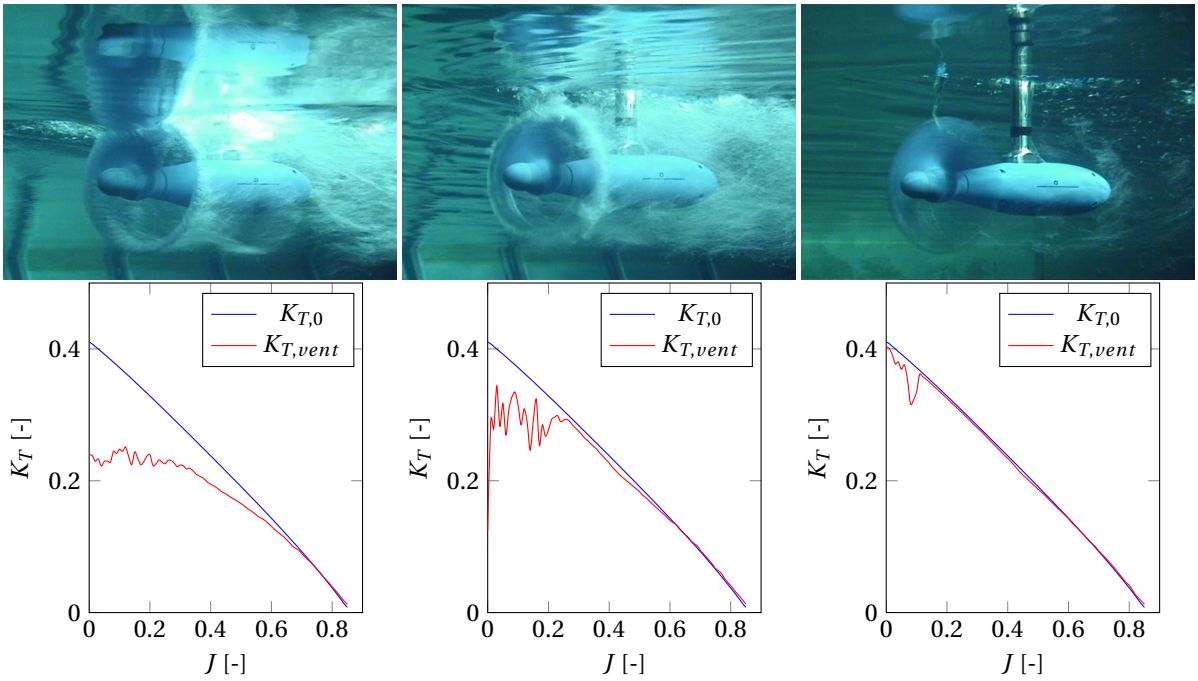

(a) I=0.00, N=600, J=0.1 (b) I=0.15, N=600, J=0.1 (c) I=0.30, N=600, J=0.0

Figure 5.5: Visualisation and force trace behaviour for three ventilation regimes; Free surface ventilation in (a), mixed ventilation in (b) and vortex ventilation in (c).

Ventilation regimes can be deduced as function of the immersion and revolution rate in fig. 5.6 and table 5.2. Free surface ventilation is found at shallow immersions, regardless of the rotation rate. Below $I = 0.1$, mixed and vortex ventilation is found, dependent on I and N, as shown in table 5.2. In vortex ventilation, a distinction based on thrust breakdown is made. Several runs show a vortex, but are not facing (significant) thrust loss. These are indicated by *(only visually)*. The distinction of ventilation regimes in terms of I and N is different with regards to the distinction of Olofsson [62] and Kozlowska and Steen [44] in J and I. Especially the usage of J (or C_T) is questionnable as in these experiments, a change in ventilation regime over J was not found. Moreover, it was said that fully submerged propellers would not ventilate, which appeared to be incorrect. Lastly, it is hard to distinguish at which J the propeller fully ventilates, as the interpretation of fully ventilation differ from research to research.

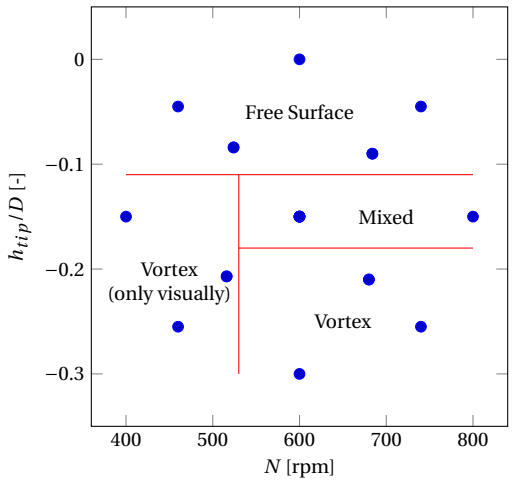

Figure 5.6: Design of Experiments

Table 5.2: criteria for ventilation regimes as found in the experiments

Ventilation regime	I	N
Free surface ventilation	|I|<0.1	-
Mixed Ventilation	0.1<|I|<0.17	N>530
Vortex Ventilation	|I|>0.17	N>530
Vortex (only visually)	|I|>0.1	N<530

Free Surface ventilation

Inception through free surface breaking is ascribed to the negative pressure gradient induced by the propeller's thrust, as it was derived in the actuator disk calculations and is a regular process, which can step-by-step be found in fig. 5.7. From an undisturbed free surface (a) the free surface is deformed, without air entering the propeller plane (b). This deformation costs energy and can be found in the force trace as the offset between the lines at high advance ratios. Afterwards, at increasing thrust loading, the free surface is broken (c). However, this does neither lead to ventilation, a loss of disk area is responsible for the slightly increased thrust breakdown. Increasing the thrust load even more, ventilation incepts from the propeller tip (d), similar to the T-type of Sato et al. [69], which extends to S-type (e) and probably, dependent on the blade design, to M-type (f) in high propeller loadings. From (e) on, it is believed that the propeller revolution rate is of influence on the thrust breakdown. Before (e), the thrust breakdown merely shows behaviour as derived using the actuator disk.

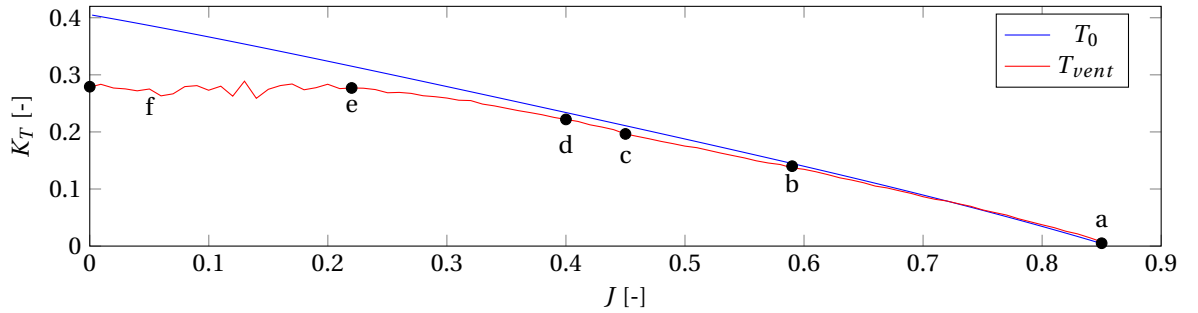

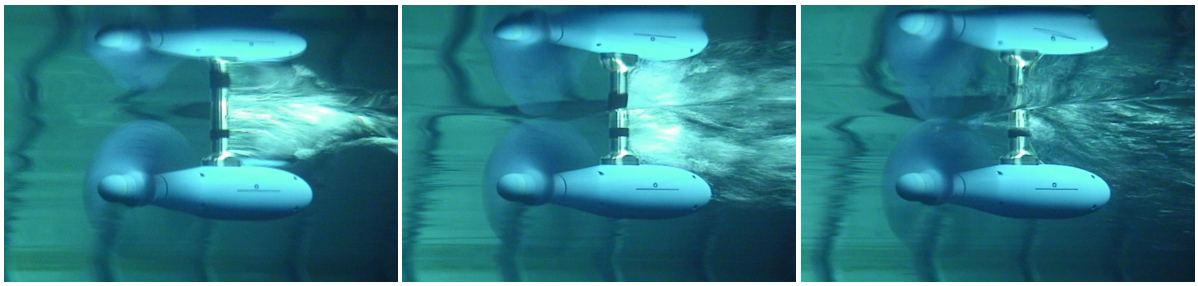

(a) $J = 0.85$ (b) $J = 0.59$ (c) $J = 0.45$

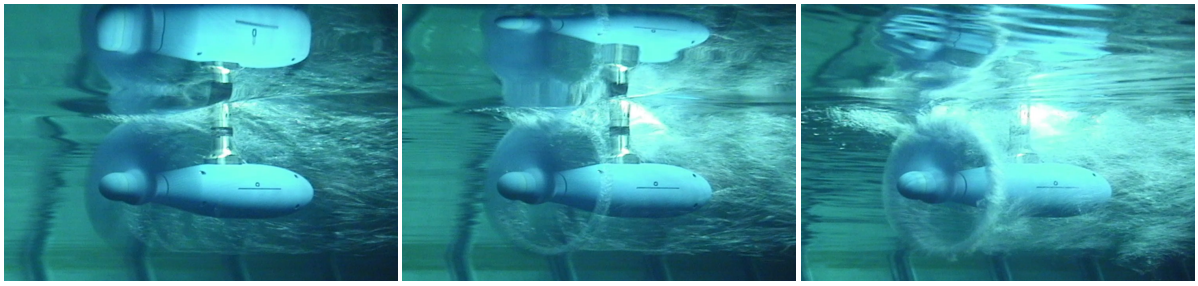

(d) $J = 0.40$ (e) $J = 0.22$ (f) $J = 0.0$

Figure 5.7: Step-by-step inception of free surface ventilation in run 17: $N = 524$ and $I = 0.084$.

Free surface ventilation appeared to be the most stable and repeatable regime. From six runs which showed free surface ventilation, data is further processed. In fig. 5.8, the thrust breakdown against the advance ratio for these runs is given. A clear distinction between (a) and (b), being the sharper thrust breakdown starting at $J = 0.3$ can be noticed.

Until $J = 0.3$, thrust breakdown is similar to the thrust loss found in the research using the actuator disk. The free surface is drawn and broken due to the high thrust loading of the propeller, formerly captured in eq. (4.4). Results for the propeller thrust breakdown were also plotted against $\sigma_V \cdot I \cdot Fr_{va}$, given in section 5.2.1. A similar trend is indeed found, but propeller data does not coincide the trend as the actuator disk results did.

Larger thrust breakdown for $J \leq 0.3$ is found for runs at a higher revolution rate. For an equal advance ratio J and thrust loading coefficient C_T, experiments showed a larger band of air rotating with the propeller (given

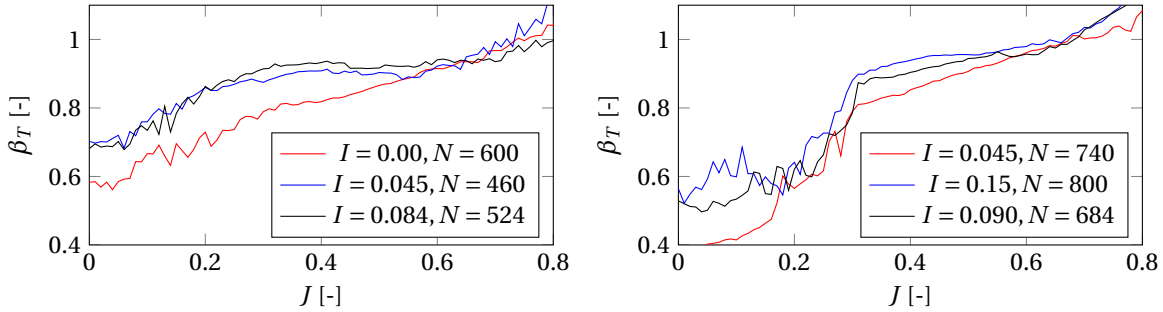

(a) Gradual thrust breakdown

(b) Increased thrust breakdown at $J \leq 0.3$.

Figure 5.8: Thrust breakdown for 6 free surface ventilation runs, showing a distinction.

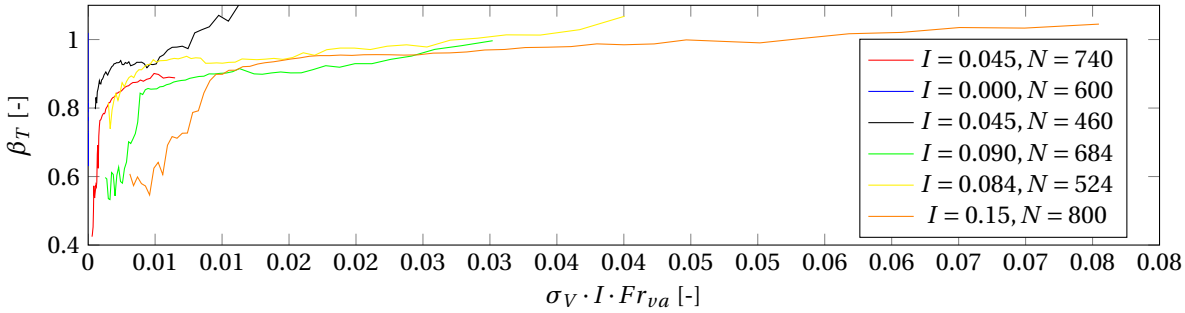

Figure 5.9: Thrust breakdown against $\sigma_V \cdot I \cdot Fr_{va}$

in fig. 5.10). Due to different advance velocity v_a and revolution rate N, the absolute thrust is different. As the propeller area cannot change, the pressure jump is governing for the increased thrust, which explains the larger band of air. The magnitude of the low pressure highly depends on the rotation rate, as the hydrodynamic pitch angle β and local blade velocity v_∞ are both dependent on N. It is expected that increased thrust breakdown must be captured as a function of N. Further research using other pitch ratios should indicate if the revolution rate dependency needs to be corrected for the pitch, as proposed by Gutsche [22] in eq. (2.37) and Pohl [66].

$$\Delta p = \frac{1}{2}\rho C_L(\theta(P/D) - \beta(N, v_a)) \cdot v_\infty^2(N, v_a) \tag{5.1}$$

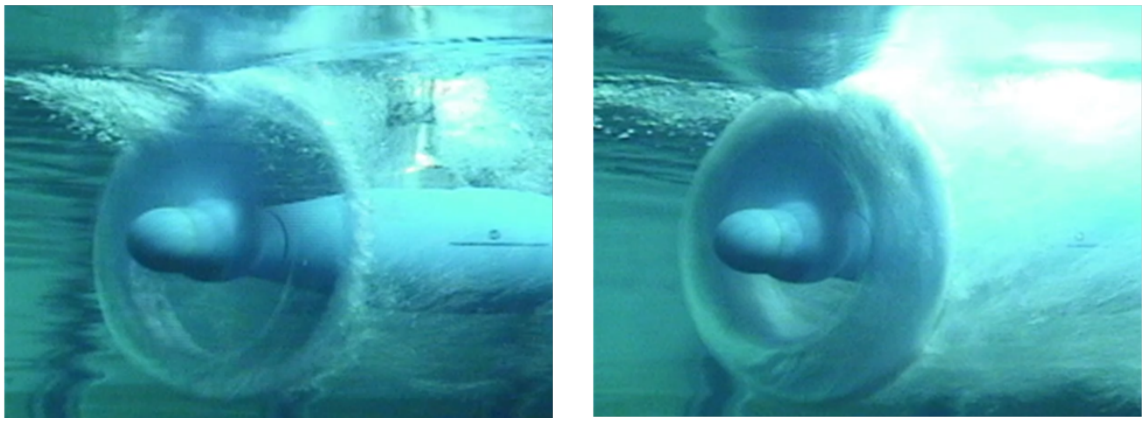

(a) I=0.084,N=524,J=0.1

(b) I=0.090,N=684,J=0.1

Figure 5.10: Visual difference in thrust breakdown extent dependent on rotation rate.

Vortex Ventilation

For vortex ventilation, inception is a irregular process. However, it is expected that vortex ventilation inception and extent follows requirements and observations set by Huse [29] and Sato et al. [70] for propeller-hull vortices. Observations of inception and extent can be found in fig. 5.11. The instability is shown by a vortex starting at the waterline (a), which appears not to be strong enough to reach the propeller blade. Not even a second later, the vortex reaches the propeller tip (b) and immediately leads to full ventilation, where the vortex moves to 0.7D (c). Severe ventilation is washed-out, which again indicates the unstable characteristic. The vortex originates from behind the propeller (d). At higher thrust loading, the vortex origin moves forward (e). This is also found by Sato et al. [70]. At J=0 in (f), the vortex hardly provides air, notwithstanding the fact that this was expected to be the heaviest situation and significant ventilation is found at the start of the run. Probable cause of this is the induced recirculation of the propeller, which does not allow the vortex to exist.

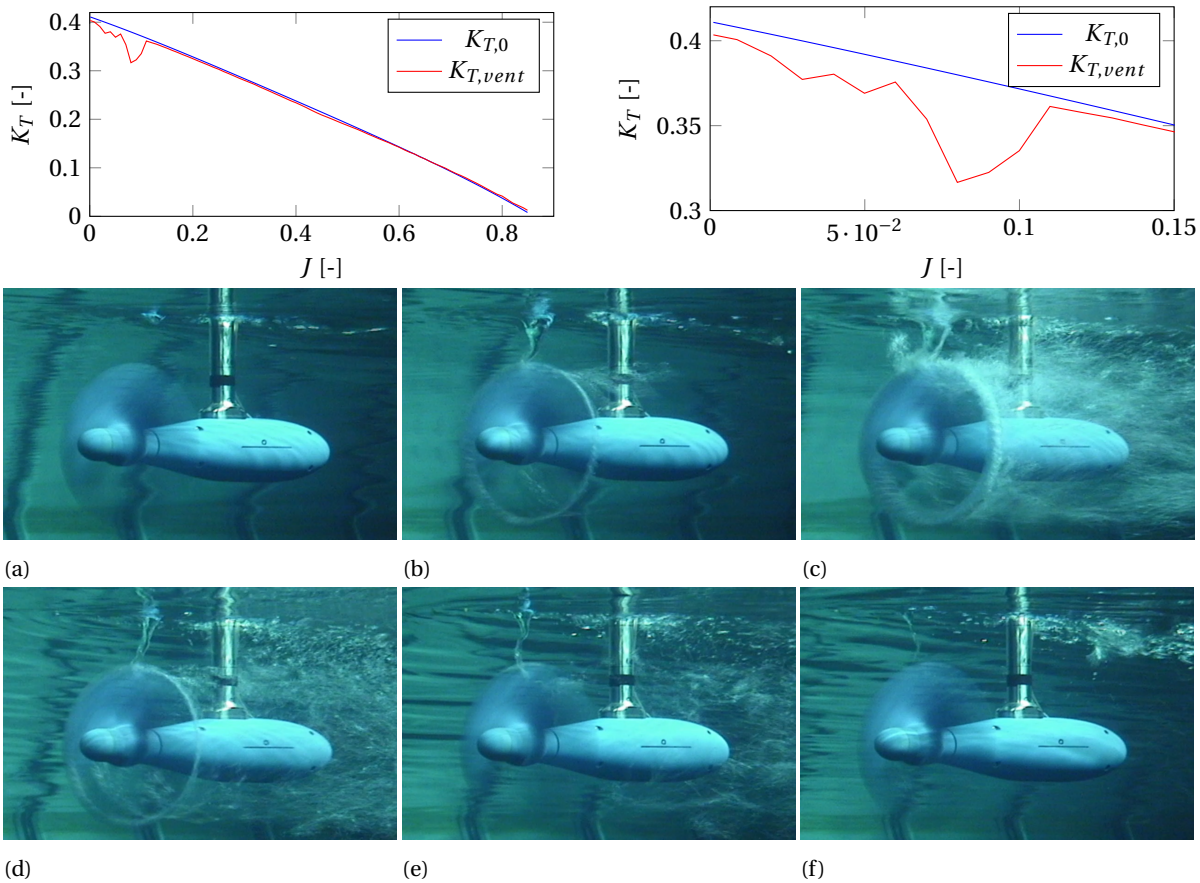

Figure 5.11: Step-by-step inception of vortex ventilation in run 7, $N = 600$ and $I = 0.3$

The vortex' rotation direction is equal to the circulation direction around the propeller blade. This coincides with the observation of Huse [29]. He hypothesized that the vortex initiated due to the circulation in the flow from the propeller, which ends on the free surface. As the vortex impinges at the propeller tip, this observation does not contradict the hypothesis.

After inception, the vortex can remain on the tip or move to 0.7D. If it remains at the tip, vortices are continuously washing-out and incepting, without significant thrust breakdown. When the vortex moves to 0.7D, thrust breakdown increases significantly. Movement of the vortex can be due to the low pressure area at 0.7D, but also the 'pirouette'-effect might be governing. Increased thrust breakdown is most probably due to entrapped air at 0.7D, where normally the largest thrust is generated. If air is entrapped for a longer time, the low pressure is diminished such that the vortex eventually moves back to the tip or directly washes out. As from that point pressure decreases and vortices might incept again at 0.7D, this may partially declare the vortex ventilations unstable characteristic. However, to derive clearer conclusions about the inception and existence of propeller vortices, high-speed video is necessary, such that the impingement on the blade around the 12 o'clock position is well captured.

Even at the deep water reference experiments, vortex ventilation is found after several seconds. No inception video is available. During available video, it is clearly visible that the vortex attaches to 0.7D (a) and moves to the tip when washing out (b).

The vortex seems quite powerful at the water surface (c) and shows resemblances to fully vortex ventilation in fig. 5.11 (b). However, at the propeller, only a weak vortex appears, found in fig. 5.12, which is barely powerfull enough to incept ventilation (b). Even when the vortex is no longer attached to the blade (c), the ventilating vortex still exists as in a bath tub. It is hypothesized that the vortex is washed out by the induced velocity around the propeller as it is moving downstream just before wash-out (b).

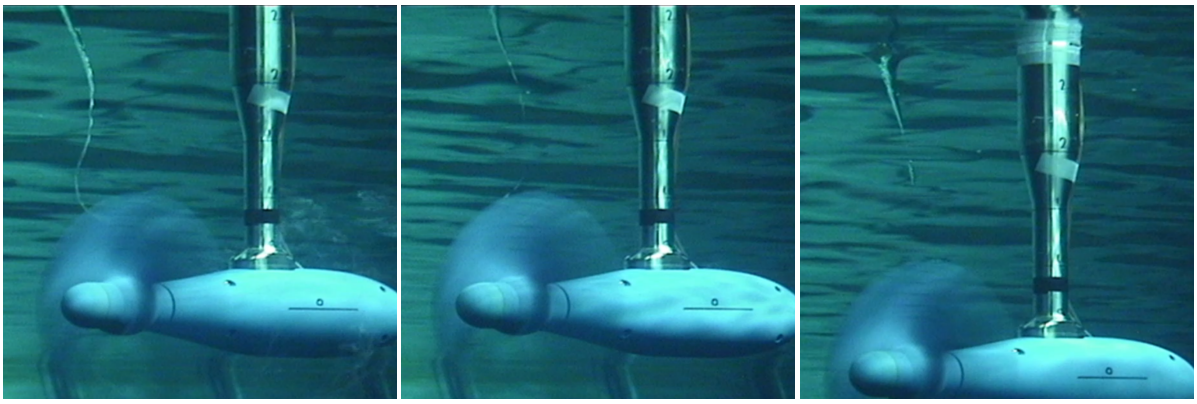

(a) (b) (c)

Figure 5.12: Vortex ventilation in deep water. $N = 800$, $I = 2.0$ and $J = 0.0$

Mixed Ventilation

Mixed ventilation is a combination of free surface and vortex ventilation. Thrust breakdown can be as high as in free surface ventilation, but also as low as in vortex ventilation. Highly fluctuating thrust and torque breakdown is found, what makes mixed ventilation of major importance for propulsive unit breakdown. On the other side, the immersion range of mixed ventilation is generally smaller than ship motions and therefore it is not expected that vessels are continuously working in the mixed ventilation zone.

Repetitive runs of mixed ventilation showed the unsteadiness of mixed ventilation in section 5.2.1, which makes inception prediction of thrust breakdown impossible. Also the upper and lower bound, corresponding to approximately vortex and free surface ventilation are shown.

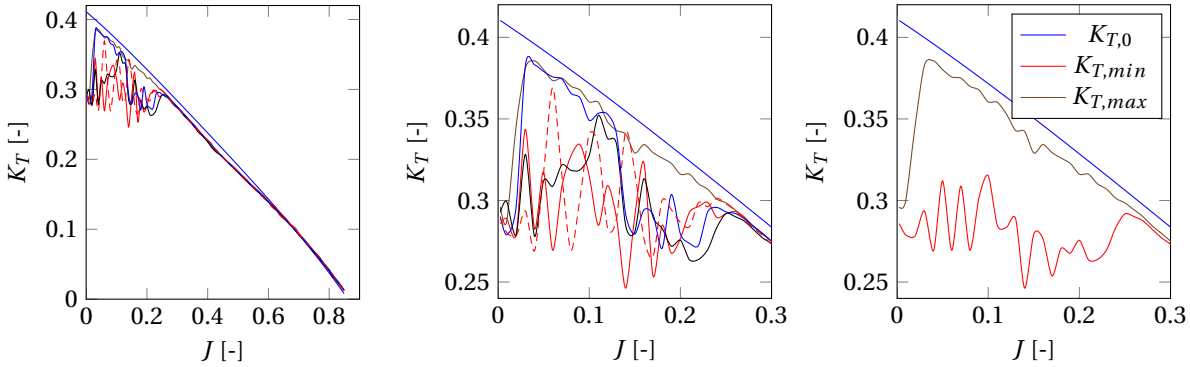

(a) Runs of I=0.15, N=600 (b) Runs of I=0.15, N=600 (zoomed) (c) Minimum and maximum

5.2.2. Torque and efficiency breakdown

Torque breakdown follows the thrust breakdown characteristic, both qualitatively and quantitatively. Figure 5.14 shows both trends for a single run. Other runs show the same trend and can be found in appendix C. Especially the fluctuation torque, most severly found in mixed ventilation due to continuous inception and wash-out of full ventilation, is stringent in terms of gearbox and engine breakdown.

During thrust loss, the resulting efficiency loss is only 5% w.r.t. the undistubed situation. Since this is far below the reduction of thrust, efficiency breakdown is of minor importance. It needs to be said that the torque demand of the propeller is used for the efficiency calculation. Dynamic behaviour of the engine due to unequal loading, i.a. axial acceleration of the propeller and application of anti-spin limiters [73] may increase the efficiency breakdown. It is advised to model engine and limiters as well to derive a conclusion about the overall efficiency loss in ventilation.

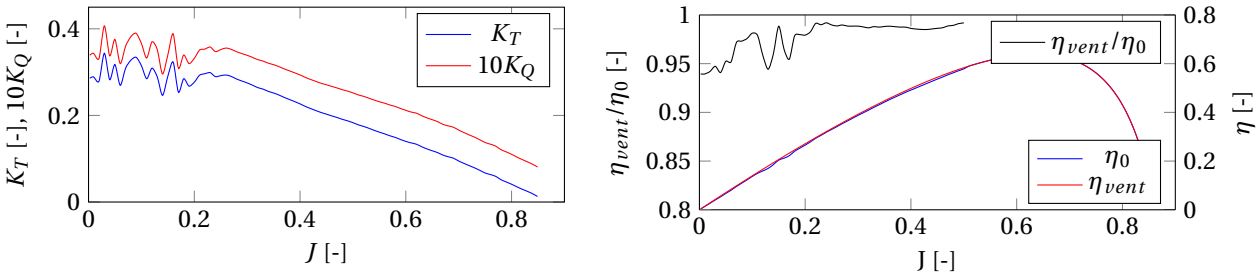

Figure 5.14: Torque breakdown follows same trend as thrust breakdown and thus efficiency is hardly influenced. Run 1: $I = 0.15[-], N = 600[rpm]$

5.2.3. Bistability

Since the advance ratio is first increased and later decreased, ventilation wash-out is found in the first phase and inception found in the second phase. This does not necessarily lead to equal ventilation (inception) points; due to different history in thrust loading until the work point bistability might occur, which might lead to hysterisis eventually. Results of Harwood et al. [25] showed bistable region for a ventilating surface piercing foil.

Results of this study shows no clear bistability and/or other influence for free surface ventilation. This might be due to the inception and wash-out mechanism; the free surface is broken before ventilation thrust breakdown is found and vice versa. Ventilation does not have any influence before the free surface breaks.

Inception via a vortex does show a slight dependency on the starting point; wash-out at a larger advance ratio than inception. The reason might be the low speed necessary for starting the vortex, while a vortex can exist in slightly higher water speed if already initiated.

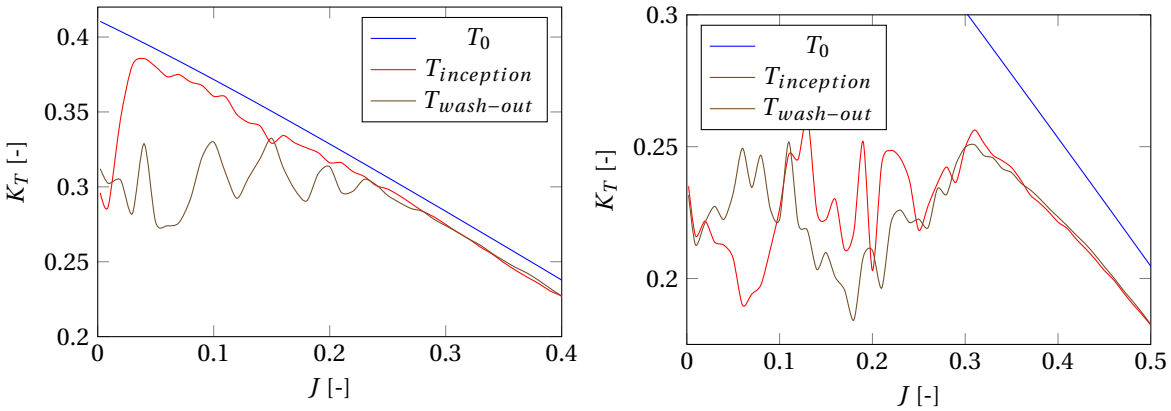

Figure 5.15: Left: Hysteresis in vortex ventilation. It is clearly visible that inception occurs at a lower advance ratio than wash-out. However it should be mentioned that not all vortex ventilation cases show this extremis of occurence. Right:Hysteresis in free surface ventilation. It is clearly visible that hysteresis does not occur.

5.2.4. Polynomial model

Experimental data is captured in polynomial models. Two models were made; one model specific for the C4.55 propeller and one generic model. The propeller specific model depends on I, J and N and delivers the absolute thrust breakdown. It uses all data acquired; 1462 data points. According to the Design of Experiments, a third order polynomial model, extended by higher powers for J (as the measurement resolution was higher) is fitted. Fitting coefficient r^2 equals 0.9267, so the polynomial model fits the data well. 3D-screenshots of the cubic model can be found in fig. 5.16. The model coefficients are given in table 5.3. Note that J, N and I are scaled to be between 0 and 1.

$$\hat{J} = \frac{J}{0.85} \qquad (5.2) \qquad \hat{N} = \frac{N-400}{800-400} \qquad (5.3) \qquad \hat{I} = \frac{I}{0.3} \qquad (5.4)$$

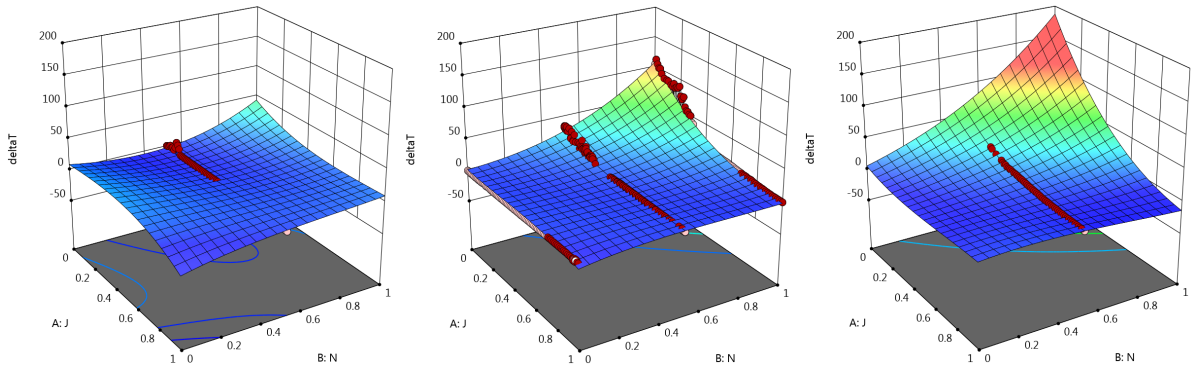

(a) (b) (c)

Figure 5.16: Polynomial model of the propeller specific thrust breakdown

Table 5.3: Equation for propeller specific polynomial model.

ΔT	3.54	8.13	85.45	15.74	-208.5	120.9	-146.2	-359.8	63.59	-86.05
$=\Sigma$		J	N	I	$J \cdot N$	$J \cdot I$	$N \cdot I$	J^2	N^2	I^2
r^2	189.7	150.7	-116.4	-136.4	-27.48	+1095	32.05	73.55	-1194	+446.1
0.9267	$J \cdot N \cdot I$	$J^2 \cdot N$	$J^2 \cdot I$	$J \cdot N^2$	$J \cdot I^2$	J^3	N^3	I^3	J^4	J^5

The polynomial model estimates the obtained thrust breakdown as if it is continuous. However, fluctuations are found in the experimental data. Figure 5.18 shows that the results of the polynomial model should always be used with care. At the low thrust breakdowns, the model is not accurate. In the application of the polynomial, this is of minor importance as low thrust breakdowns are generally not leading to majr safety issues. A more stringent drawback of the polynomial model is the inability to capture the unsteady mixed ventilation (fig. 5.18 (b)). In free surface ventilation conditions, the averaged thrust breakdown in captured sufficiently, but the model shows structural shortcomings in exactely capturing the trend between $J = 0$ and $J = 0.4$.

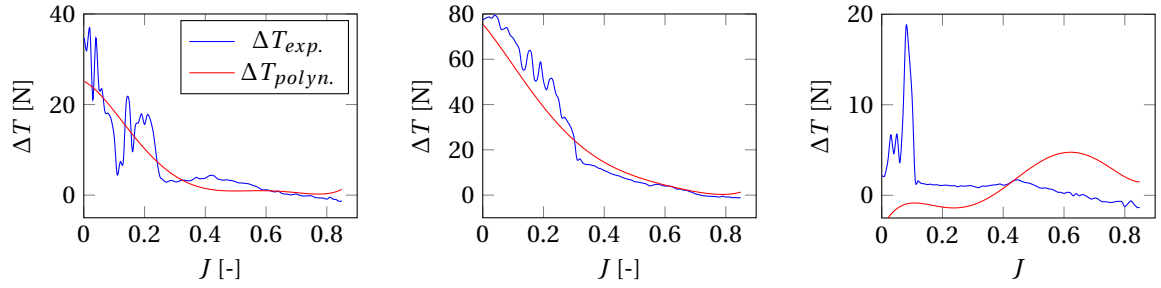

Figure 5.17: Comparison of the thrust breakdown between polynomial model and experimental data.

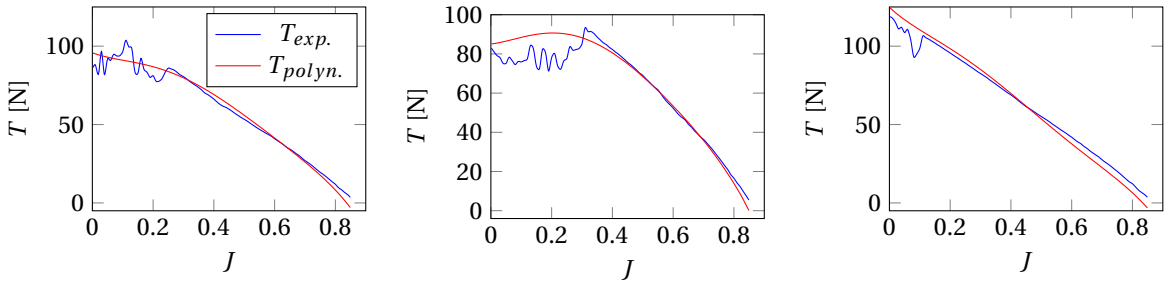

(a) Mixed: I=0.15, N=600 (b) Free Surface: I=0.090, N=684 (c) Vortex: I=0.30, N=600

Figure 5.18: Comparison of the reduced thrust between the polynomial model and experimental data.

For the generic model, data had to be processed to obtain parameters independent of the propeller characteristics. Inception is dependent on the immersion depth and loading of the propeller. The immersion depth is already propeller independent. The loading of the propeller in terms of advance ratio J is rewritten in the thrust loading coefficient C_T according eq. (2.18) and the propeller specific K_T. It is expected that using C_T, inception dependence on P/D-ratio is excluded. Since C_T goes to ∞ for J to zero, not all data could be used. Only data for which $C_T < 60$ is a used, since propellers hardly exceed this thrust loading in regular shipping.

The extent of ventilation is hypothesized to be dependent on the local velocity on the blade, and thus nD, but also on the blade area A_e/A_0 and pitch ratio P/D. The latter two were not varied and their influences are not taken into account. nD is taken into account by non-dimensionalizing them against the propeller diameter using the rotational Froude number of Shiba [72]: $Fr_{nD} = nD/\sqrt{gD}$. Thrust breakdown is given in ΔC_T. In total, 1020 data point are used. Results of the polynomial model are visible in section 5.2.4. The coefficents can be found in table 5.4. Note that the immersion ratio, rotational Froude number and thrust loading coefficient is spaced between zero and one. Comversion factors are also listed in table 5.3.

This polynomial model delivers the relative thrust breakdown and is such (theoretically) wider applicable. However, as only one propeller is studied, this model should be used with care. More propellers should be examined and processed to make a more thrustworthy generic polynomial model and to verify the (hypothesized) influence of P/D and A_e/A_0.

$$\hat{C_T} = \frac{C_T}{60} \qquad (5.5) \qquad \hat{Fr_{nD}} = \frac{Fr_{nD} - 1.03}{2.06} \qquad (5.6) \qquad \hat{I} = \frac{I}{0.3} \qquad (5.7)$$

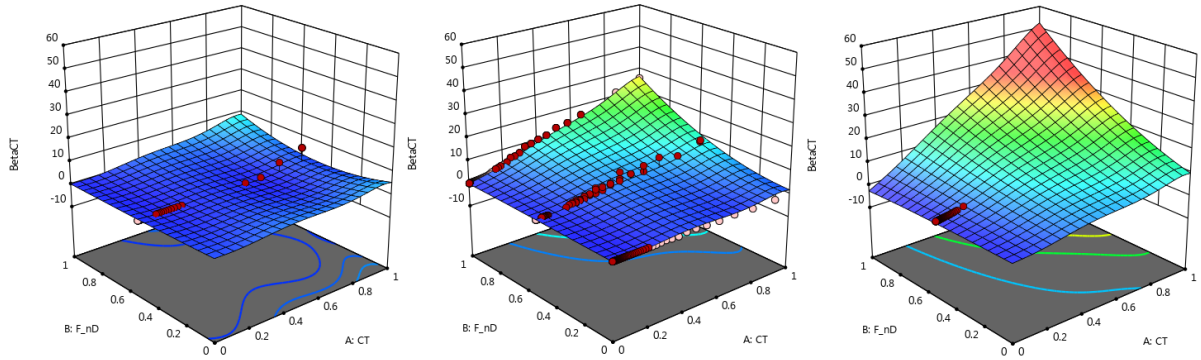

(a) (b) (c)

Figure 5.19: Polynomial model of the generic thrust breakdown

Table 5.4: Equation for generic polynomial model. $C_T = C_T/60$, $F_{nD} = (F_{nD} - 1.0273)/2.0546$ and $I = I/0.3$, R^2=0.9237

ΔC_T	0.107	5.70	-1.72	3.80	17.2	-26.6	7.78	-22.4	-0.672	-13.5
$= \Sigma$		C_T	F_{nD}	I	$C_T \cdot F_{nD}$	$C_T \cdot I$	$F_{nD} \cdot I$	C_T^2	F_{nD}^2	I^2
	-40.4	5.13	22.9	20.4	-6.39	334	10.6	-987	1108	-429
	$C_T \cdot F_{nD} \cdot I$	$C_T^2 \cdot F_{nD}$	$C_T \cdot F_{nD}^2$	$C_T \cdot I^2$	$F_{nD} \cdot I^2$	C_T^3	I^3	C_T^4	C_T^5	C_T^6

5.3. Reynolds scale effects

Deepwater tests were conducted to exclude the influence of different Reynolds numbers from the ventilation thrust breakdown. A short notice is given to the difference between the K_T-curves at N=400 and N=800 [rpm]. It was expected that a 5% smaller value of K_T for the low rotation rates would be found, due to laminar flow on the blade. Contrary to the expectations, only a difference of less than three percent for low advance ratios is found, while $K_{T,400}$ is even below $K_{T,800}$. In fig. 5.20, one can see that this trend is found in all deepwater tests. As fig. 5.21 and table 5.5 show; the relative error in fig. 5.20 is partially due to larger difference between K_T, but also due to the fact that $K_{T,400}$ decreases.

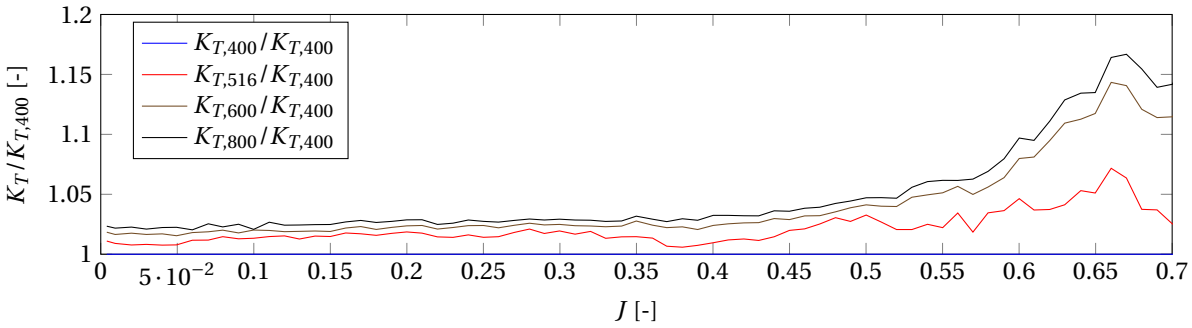

Figure 5.20: Relative difference of K_T with regard to $K_{T,400}$. Against expectations, K_T is increasing with larger rotation rates.

Table 5.5: Differences between K_T at different number of revolutions.

J[-]	$K_{T,400}$[-]	$K_{T,800}$[-]	ΔK_T [-]	$\Delta K_T/K_{T,400}$ [%]
0.00	0.399	0.408	-0.009	2.3%
0.05	0.383	0.391	-0.009	2.2%
0.10	0.362	0.369	-0.008	2.0%
0.15	0.341	0.349	-0.008	2.4%
0.20	0.319	0.328	-0.009	2.8%
0.25	0.297	0.305	-0.008	2.7%
0.30	0.275	0.283	-0.008	2.8%
0.35	0.253	0.261	-0.008	3.1%
0.40	0.231	0.239	-0.007	3.1%
0.45	0.208	0.216	-0.007	3.5%
0.50	0.184	0.193	-0.009	4.5%
0.55	0.160	0.170	-0.010	5.8%
0.60	0.135	0.148	-0.013	8.8%
0.65	0.109	0.123	-0.015	11.9%
0.70	0.087	0.099	-0.012	12.4%
0.75	0.059	0.072	-0.014	18.7%
0.80	0.031	0.044	-0.013	-
0.85	0.003	0.015	-0.012	-

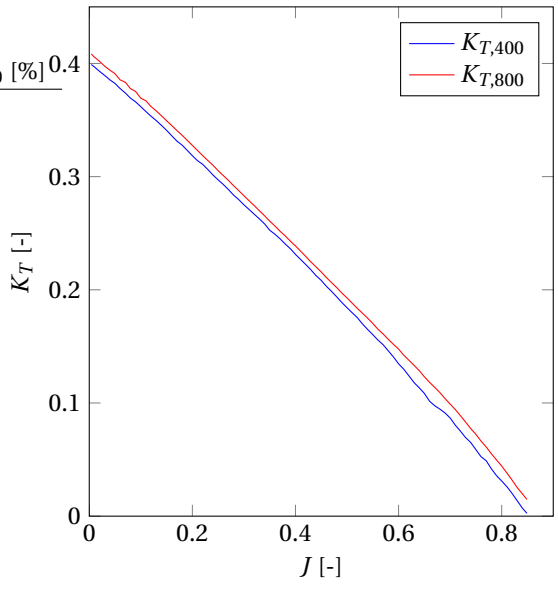

Figure 5.21: Difference in K_T dependent on revolution rate.

6

Computational research and comparison

6.1. Grids and numerical settings

6.1.1. Research cases

Numerical ventilation calculations appeared to be heavy and expensive. For that reason, only a small number of calculations were performed. Based on experimental research, interesting work points were chosen to use in CFD calculations. These calculations are such that multiple ventilation regimes in various severeness and inception modi were evaluated on their ability to be predicted. Free surface ventilated cases were mostly simulated. To improve convergence behaviour, the convective velocity is not zero. Cases are listed in table 6.1.

Table 6.1: Workpoints and ventilation regimes of numerical cases

Case				
I	N	J	Ventilation regime	turbulence model
0.15	600	0.2	Mixed Ventilation	$k-\omega TNT$
0.30	600	0.1	Vortex Ventilation	$k-\omega TNT-XLES$
0.084	524	0.2	Free Surface Ventilation	$k-\omega TNT$
0.084	524	0.1	Free Surface Ventilation	$k-\omega TNT$
0.09	684	0.1	Free Surface Ventilation	$k-\omega TNT$

6.1.2. Grids

Geometry of the thruster is comparable to the thruster used in the experiments. Around the geometry, an unstructured `Hexpress`-grid was built. As both the free surface [36] and propeller axis needs to be on a grid line, initial grid size is determined by this distance. Viscous layers such that the y^+ is lower than 1 were inserted. The by B. Schuiling provided propeller grid 3 from the verification study is used. This grid still shows deviation from the grid independent solution found in the uncertainty study, but hardly deviates from the finer propeller grid 4. At the grid interfaces, grid cell sizes are of similar size to improve grid interpolation. Grid specifications are listed in table 6.2

Table 6.2: Grid specifications

	Cases				**Refinement level**
I	Number of cells	Initial cell size	Free Surface	around body coarse/fine	above propeller
0.15	12.9	0.15145	6	3/6	8, h=0.73D
0.084	7.79	0.13607	6	3/6	7, h=0.73D
0.09	7.32	0.13743	6	3/6	7, h=0.73D
0.30	7.79	0.12423	6	3/5	7, h=0.94D

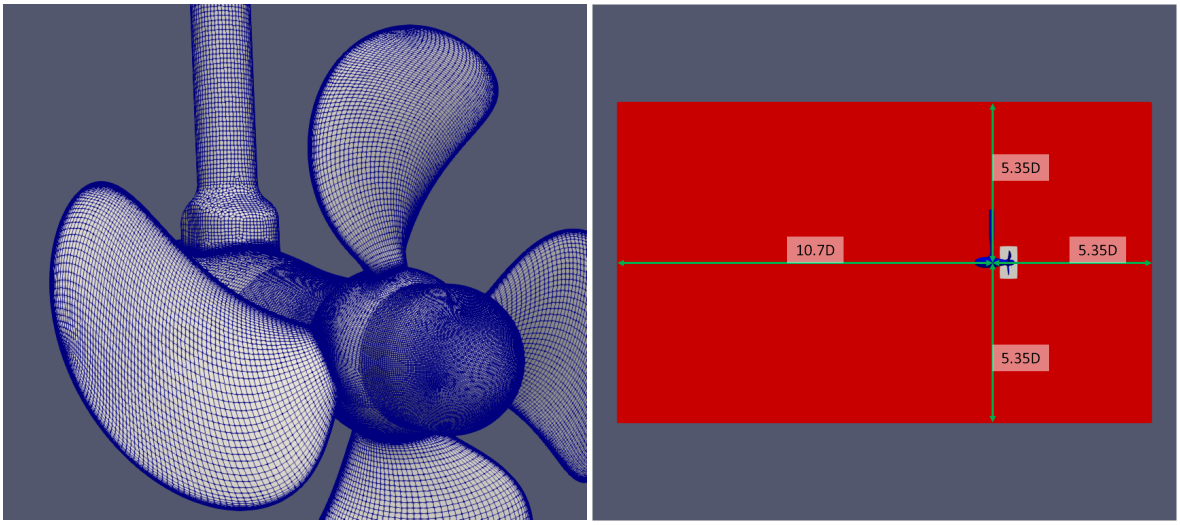

Figure 6.1: Left: Geometry of the thruster and propeller as used in the ventilation calculations. Right: Domain size as used.

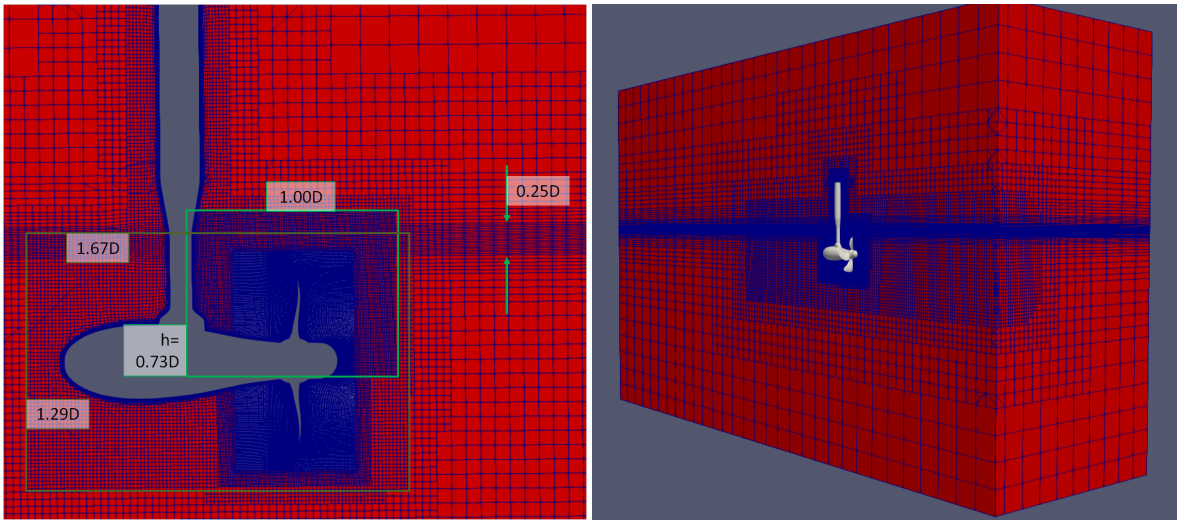

Figure 6.2: Refinement in the domain for I=0.15. Especially above the propeller and at the free surface, small cell are placed. Note that the exact size and placement of the refinement boxes are dependent on the immersion depth as well. Latter grids do not have the elongation of the refinement to the inflow as is shown in the right figure.

6.1.3. Numerical settings

`ReFRESCO` version 2.5.0 was used in the propeller calculations. Propeller rotation is modeled by application of a moving propeller grid. The rotation increment per timestep was 0.5 °, corresponding to timesteps smaller than $2 \cdot 10^{-5}$s. Second order timestepping is applied using `ReFRESCO`s implicit backward `three time level` scheme [53]. All convective quantities are also second order discretized using van Leer's flux limited TVD Scheme, except for the free surface equation, for which ReFRICS is used. 100 iterations per outerloop were performed. All numerical settings and material properties can be found in appendix D.2.

6.1.4. Start-up method

Starting the calculation should require a minimum of computational effort, while divergence is to be prevented. Secondly, during start-up, the propeller loading should not be higher than the expected work point to prevent early inception. Divergence may occur in the free surface, as pressure difference due to immediate acceleration of velocity leads to a unphysical disturbance of the free surface, as also found in the application of the actuator disk. In `ReFRESCO`, it is possible to prevent start-up divergence of the free-surface by gradual acceleration of the body, or by imposing the velocity and using body force to damp the unphysical waves. The latter is used as this method is usually computationally more efficient and leads to an initial low thrust

loading. This comes at the cost of a higher chance of instability, although the method showed to be stable enough for the start-up, as waves are hardly generated by the body and strut.

Two methods of propeller thrust start up have been evaluated. The first method is taking the propeller into account using a frozen rotor application. If the interaction between free surface, thruster and propeller is sufficiently converged, a restart is done, where the propeller rotation is then taken into account using a moving grid. The result is acceptable, but the starting procedure requires for two separate simulations and a long simulated time is necessary to wash-out unphysical flow phenomena from the AFM-calculation.

Secondly a method solely using moving grid approach is used. This method is developed by B. Schuiling for behind ship conditions. Slight adaptations were necessary such as lowering the maximum rotation angle per timestep and decreasing the end timestep. Figure 6.3 shows the procedure over time. In the first phase, the propeller is accelerated from zero rotation rate to the desired revolution rate at a large rotation angle per timestep. In the second phase, several propeller rotations are simulated to obtain correct interaction between free surface, thruster and propeller. Furthermore, incorrect wake due to the start up can convect downstream. A periodic solution expected after this phase. In the third and last phase, timestep and rotation angle per timestep are diminished equally (such that the rotation rate is constant) to obtain results at a higher temporal discretization and so being able to simulate highly unsteady fluctuations. Only a single simulation is necessary and the propeller is in exactly in (a multiple of) the top position after phase 1 in this start-up method.

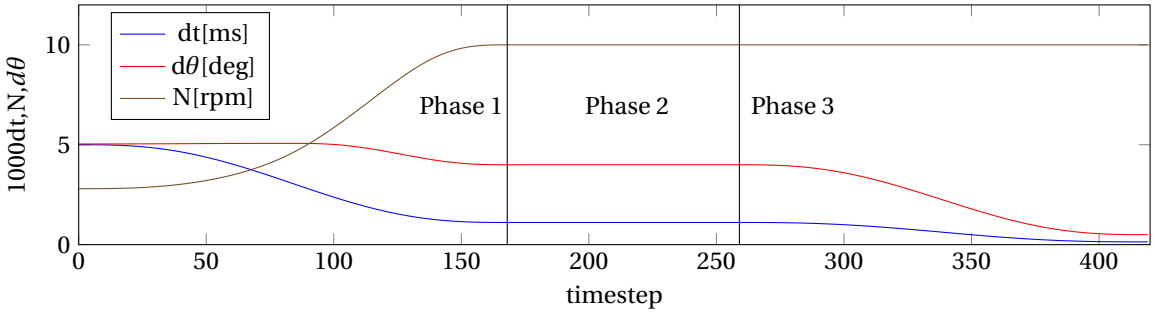

Figure 6.3: Start-up procedure for solely moving grid

6.2. Computational results and comparison

Calculations of three ventilation regimes were performed. For these calculations, iterative processes, inception behaviour and thrust extent are presented.

6.2.1. Iterative processes

In fig. 6.4, $L2$-iterative convergence can be found for $I = 0.090$, which is also representative for the other calculations. Other iterative behaviour can be found in appendix D.3. The start-up phase, from timestep zero to 1300 is characterized by it's chaotic convergence. When timestep size is reduced, iterative convergence improves, slowly. Figure 6.5 shows the unsteady iterative convergence for five timesteps. One can find that only ω stagnates and all other quantities are still converging. That the ω-equation stagnates is a common issue for multiphase flows. To decrease the computational effort, the maximum amount of outerloops was set to 100. As iterative behaviour is well, one could probably decrease the under-relaxation to decrease the number of outerloops.

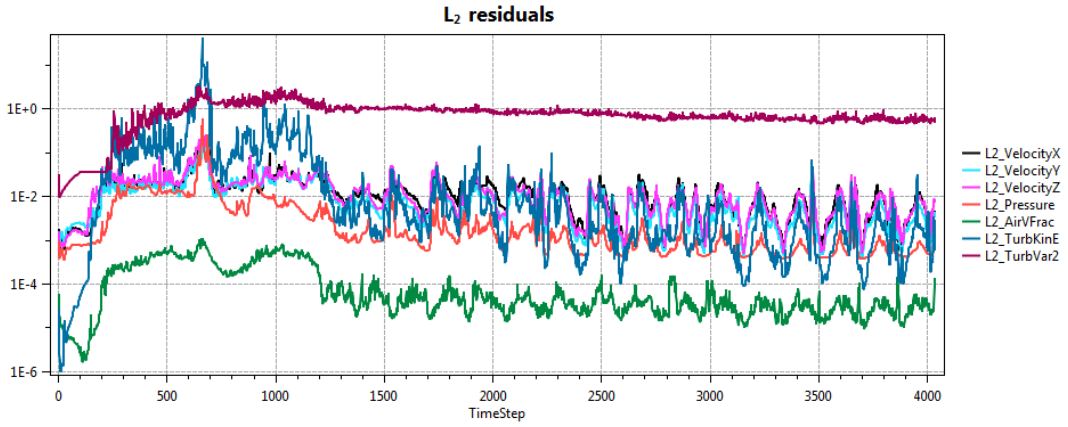

Figure 6.4: L_2-residuals of $I = 0.090$, $J = 0.1$, which is illustrative for other calculations.

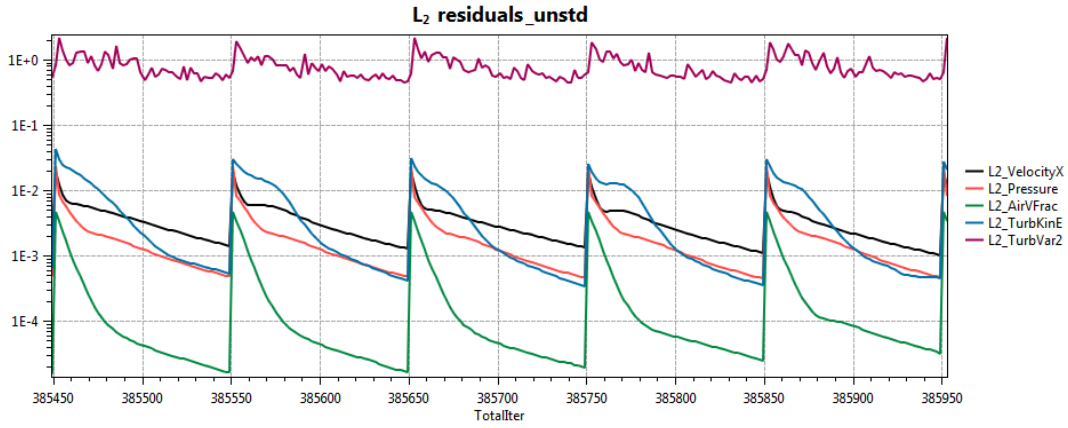

Figure 6.5: Unsteady L_2-residuals of $I = 0.090$, $J = 0.1$, which is illustrative for other calculations

Force convergence can be found below. Whereas in non-ventilating simulatiosn 100 outerloops were sufficient for force convergence section 4.3.5, this was not for the ventilating case. After 100 outerloops, the thrust and torque is still changing, although it seems to be nearly converged.

In the rotating disk, a problem regarding the interpolation between two grids was found. Also in the ventilating propeller, it can be found in fig. 6.7 that air is prevented from flowing out the propeller domain, visualized by the accumulation of air on the red-white interface behind the propeller. It does not seem to harm the result, but a note should be given to this.

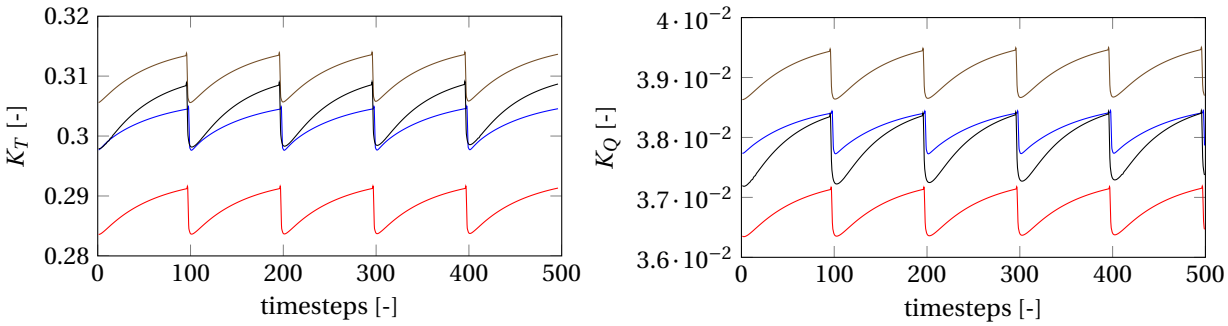

Figure 6.6: 4 total propeller moments convergence in the last top blade passage for ventilating cases. It can be found that forces are not yet fully converged, even when 100OL are used.

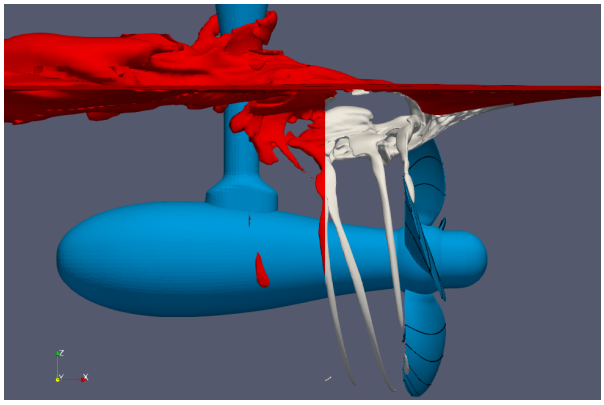

Figure 6.7: Air is prevented by flowing out of the white propeller domain into the red outer domain.

6.2.2. Inception

Ventilation inception was not found for vortex ventilation. It showed a deforming water surface and a dead water area above the propeller, but using streamlines the vortex was not found in the numerical simulations (fig. 6.8). This is most likely due to the application of Boussinesq's assumption, which leads to production of turbulence in areas of high velocity gradient. The influence of the $k-\omega TNT-XLES$ turbulence model can be seen as the increased resolution of the air volume fraction plot above the propeller.

Inception via free surface breaking was captured in CFD. The trough before the propeller was accurately found, given in fig. 6.9. This was as expected as inception due to free surface breaking was already found in the ventilating actuator disk.

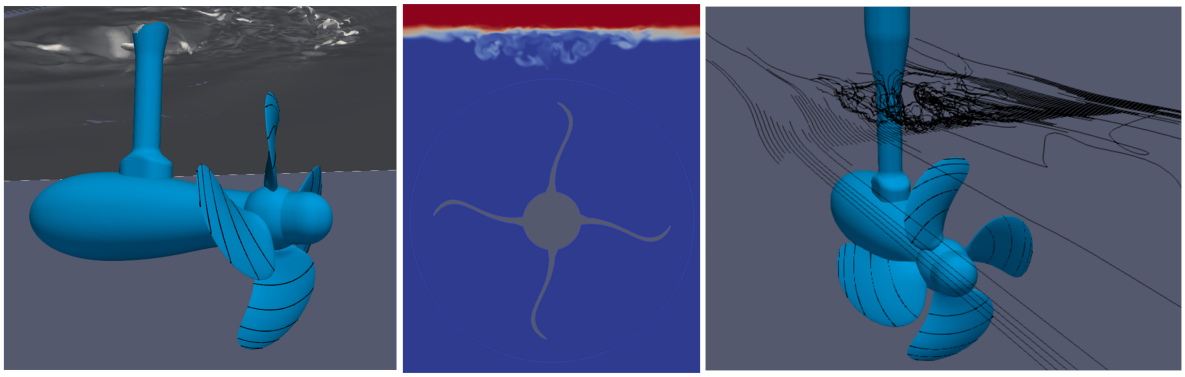

(a) contour of $\alpha = 0.5$

(b) YZ-cross section of α at the heart of the propeller

(c) streamlines above the propeller just below the water surface.

Figure 6.8: Numerical result for vortex ventilation shows no vortices or ventilating inception.

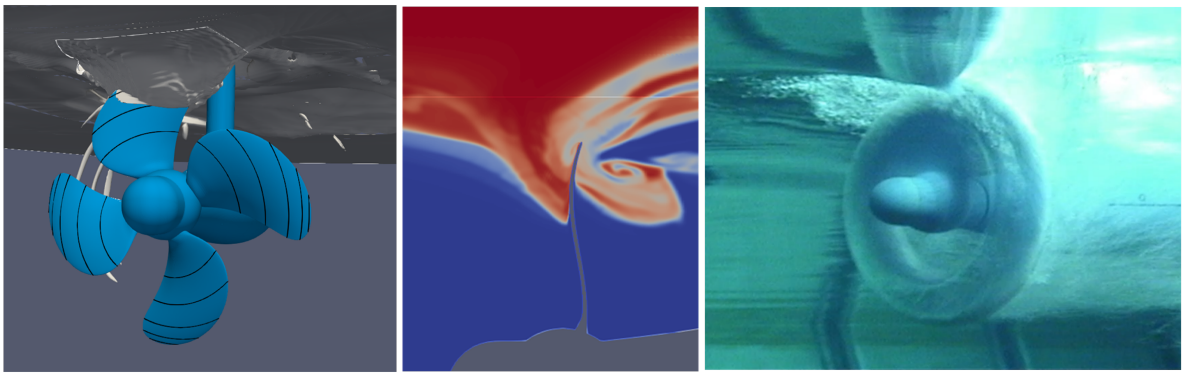

(a) contour of $\alpha = 0.5$

(b) XZ-cross section of α at the heart of the propeller

(c) Experimental results corresponding to the numerical case.

Figure 6.9: Free surface breaking inception in experiments vs. numerical simulations for I=0.090

6.2.3. Thrust loss

Propeller thrust breakdown can be deduced from monitor data of the calculations. In fig. 6.10, the thrust breakdown for the propeller can be found. A periodic solution is not yet found, but it is nor necessary as in this assessment preliminary conclusions can already be derived. Obtaining a periodic solution would need excessively more computational hours, at the cost of more calculations at different working points. The reduced thrust shows a strong dependency to the blade position. Furthermore it is noticable that $I = 0.084, N = 524, J = 0.2$ shows a slightly higher thrust than $J = 0.1$, which is contradictory to the non-ventilating case. The largest thrust loss is found for $I = 0.090, N = 684, J = 0.1$

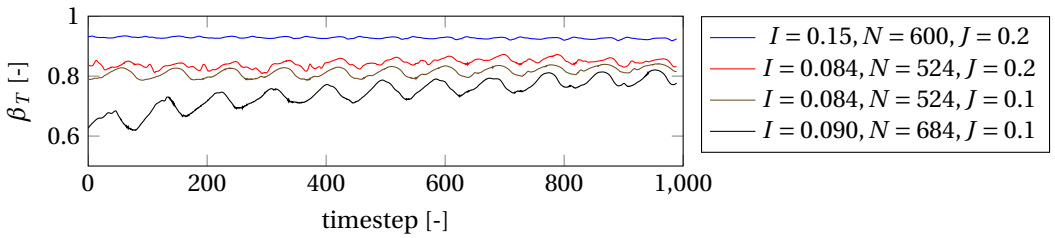

Figure 6.10: Propeller thrust breakdown over time in CFD.

Experimental and numerical results do not coincide. Table 6.3 and fig. 6.10 both show the differences. The uncertainty of the experimental result is set to 1%, equal to the experimental result in the grid refinement study and, as explained, questionable. Only for $I = 0.15, N = 600, J = 0.1$, the uncertainty is larger, as from multiple runs an uncertainty due to the highly varying thrust breakdown in the mixed ventilating regime could be estimated. Experimental research shows a difference in K_T of 0.1, 30% of the average value. No uncertainty is known for the numerical results, as no grid refinement study is executed for the ventilating propeller. Based on the grid refinement study for the non-ventilating propeller, uncertainties of at least 0.4% on K_T and 0.2% on K_Q can be postulated. It is expected that due to the unstable characteristic, the uncertainty is higher than for the non-ventilating case.

Table 6.3: Comparison between experimental and numerical thrust and torque values.

Case			Experiment				Numeriek				Comparison	
I	N	J	K_T	T	K_Q	Q	K_T	T	K_Q	Q	K_T	K_Q
0.15	600	0.2	0.255	75.218	0.0353	2.4233	0.304	89.66	0.0384	2.638	16.0%	8.0%
0.084	524	0.2	0.273	61.310	0.0323	1.6885	0.287	64.5	0.0367	1.92	4.8%	12.0%
0.084	524	0.1	0.284	63.671	0.0339	1.7744	0.309	69.5	0.0393	2.06	8.3%	13.8%
0.09	684	0.1	0.198	75.911	0.0239	2.1296	0.2978	114.1	0.0370	3.304	33.4%	35.5%

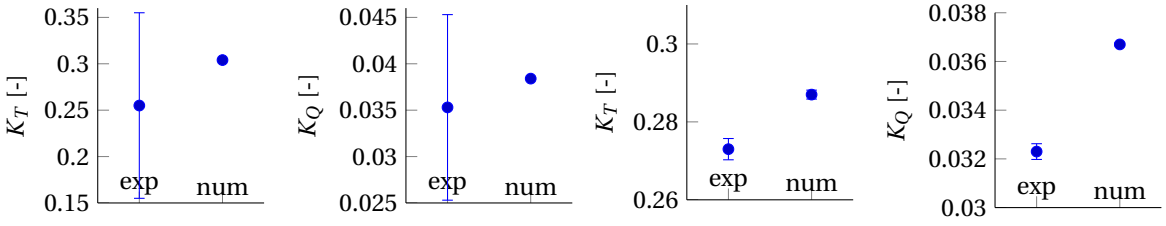

(a) $I = 0.15$, $N = 600$, $J = 0.2$, left: K_T, right: K_Q

(b) $I = 0.084$, $N = 524$, $J = 0.2$, left: K_T, right: K_Q.

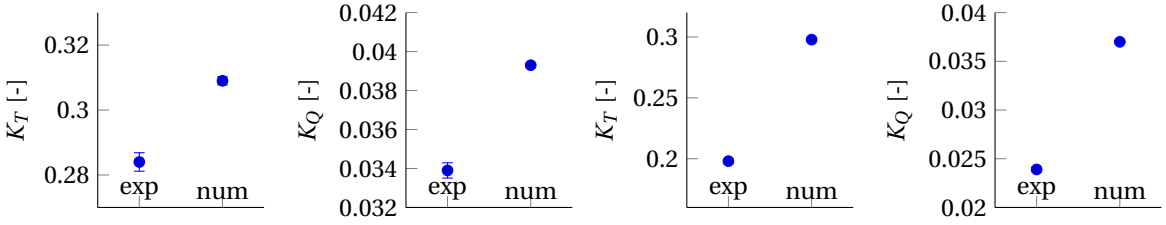

(c) $I = 0.084$, $N = 524$, $J = 0.1$, left: K_T, right: K_Q.

(d) $I = 0.090$, $N = 684$, $J = 0.1$, left: K_T, right: K_Q.

Figure 6.11: Uncertainty bands of numerical results are taken from open water validation study and probably underestimated.

Periodic thrust loss as found in fig. 6.10 is due to pressure loss when the propeller blade is (nearly) surface-piercing. As the propeller is hardly surface-piercing in I=0.15, the periodic thrust loss is smaller than in other cases, which are nearly equally immersed and show nearly the same thrust breakdown. Figure 6.12 shows the thrust per angle for four free surface ventilation cases. At 0°, the blade is in top position and the largest thrust loss is found for all cases. This corresponds to fig. 6.14, where positive and negative pressure is reduced if the blade is nearly surface-piercing.

According to fig. 6.12, thrust is rapidly building up after 0°. This increase is unexpected according Wagner [77], which states that thrust is fully build-up after several chord lengths/rotations.

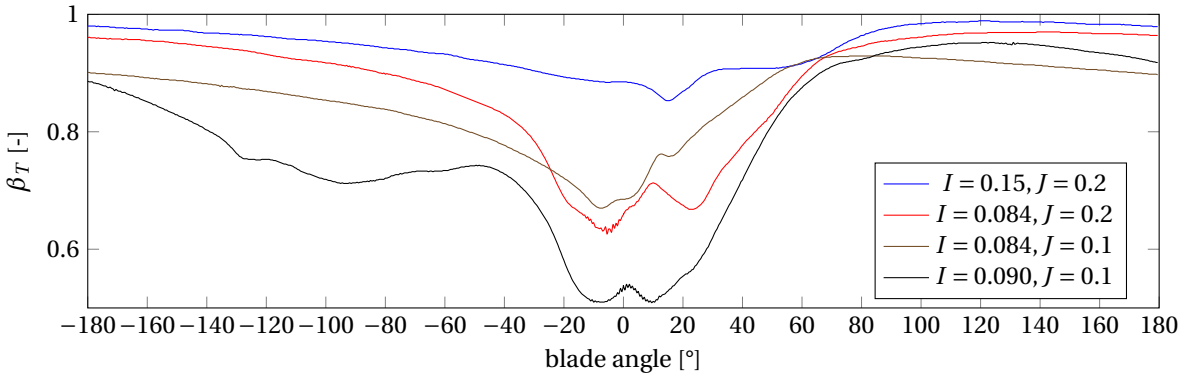

Figure 6.12: Thrust per angle. The non-dimensional thrust is derived by the deep water thrust at the same J. At 0°, the propeller blade is in top position.

The smooth signal and error in thrust loss in fig. 6.10 is ascribed to insufficient air entrainment. Whereas the blades are continuously covered in air in experiments, hardly any air is transported on the blade after 90 °in CFD. Only thrust breakdown due to surface piercing was found and the ventilating tip vortex does not reach the blade. (fig. 6.13).

Two simulations at equal C_T corresponding to $J = 0.1$ and nearly equal immersion($I = 0.090$ and $I = 0.084$) showed equal thrust breakdown, whereas the pressure on the blade was different (see fig. 6.14. This indicated that thrust breakdown due to surface piercing, initiated by the thrust loading coefficient of the propeller, was accurately found.

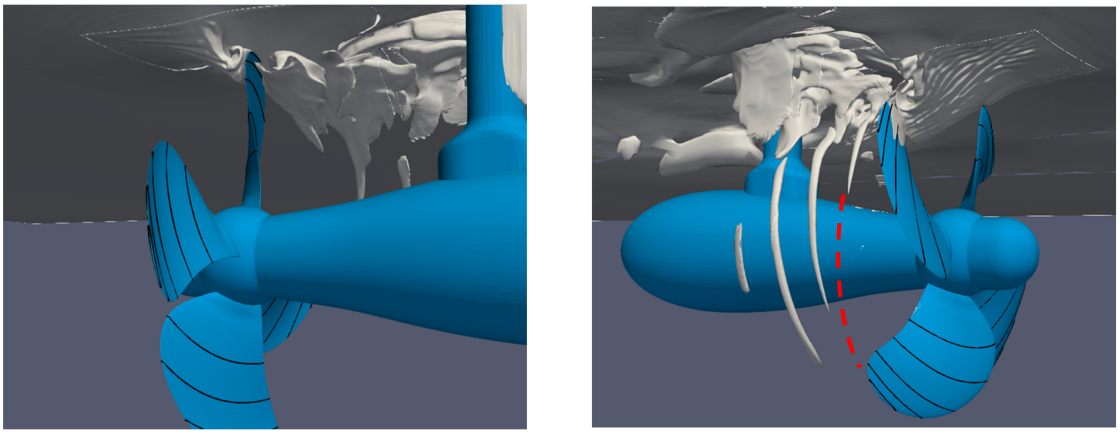

Figure 6.13: Insufficient air advection in $I = 0.084, J = 0.2$(left) and $I = 0.090, J = 0.1$(right). In the center figure it can be seen that the ventilated tip vortex does not ventilate on the blade itself.

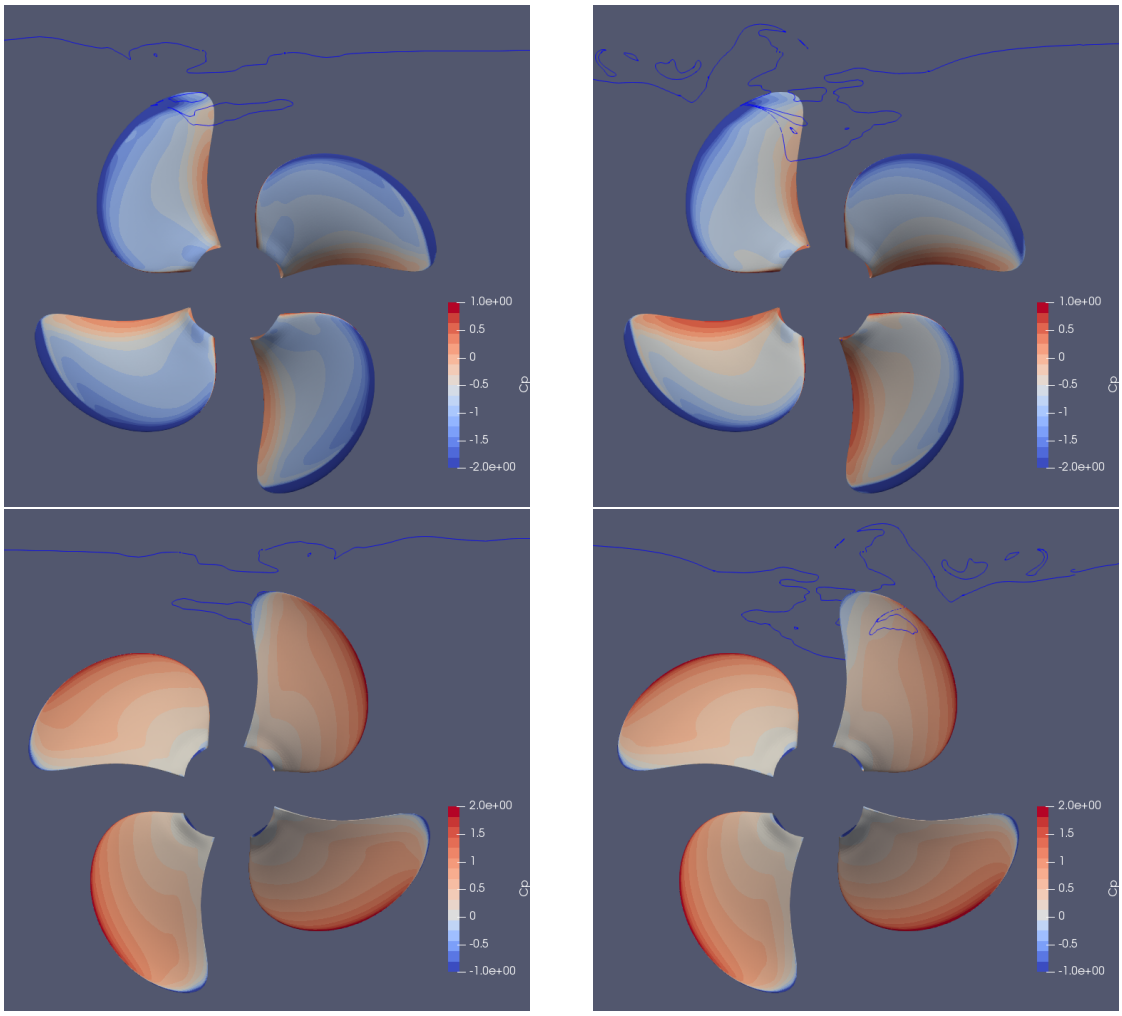

(a) Pressure on propeller blades for $I = 0.15[-], N = 524[rpm]$, timtestep 4364

(b) Pressure on propeller blades for $I = 0.15[-], N = 684[rpm]$, timtestep 4912

Figure 6.14: Suction and pressure side of the propeller at surface-piercing ventilation. $C_p = (p - \rho_w g z)/(0.5 * \rho_w * (nD)^2$.

6.3. Improvements of computations

Unsimilarities were found between the experiments and numerical simulations with regard to thrust breakdown and air advection. Further calculations were conducted to improve calculations. These include application of other turbulence models and boundary conditions on the propeller blade walls.

6.3.1. Turbulence modeling

It was expected that Boussinesq's assumption is too restrictive for the correct simulation of vortices. As already proposed in section 4.4 and indicated by Pereira et al. [64], $TNT-EARSM$ was applied, which does not assume linear dependency on the velocity gradient for turbulence production. According [64] and [1], also scale resolving simulations ($XLES$ or improved Delayed Detached Eddy Simulation, $IDDES$) would be profitable. Result for $XLES$ were however not obtained as for the stability necessary omega-limiter prevented the change from RaNS to LES-mode. It was assumed that the same problem would hold for $IDDES$. Unnecessity of the omega-limiter may be obtained when multi-phase turbulence corrections such as the Reboud-correction [37], [9], [67] and Gaussiamn corrections [68] were applied. Klapwijk [38] showed improved behaviour in terms of instability and shedded air pockets for the $k-\epsilon$ SST-model. For $EARSM$, the correction showed no improved behaviour.

Comparable to the results found in the single-phase calculation; a longer ventilating tip vortex was found when $EARSM$ was applied, see fig. 6.15. This is ascribed to the calculated lower pressure in the vortex core. It hardly had influence on the overall thrust loss, which still shows only thrust loss on the blade in the upright position. Small deviatons are slightly more unsteadiness, but higher thrust in case of $EARSM$, as shown in fig. 6.16. The higher thrust in $EARSM$ may be due to lack of a periodic solution.

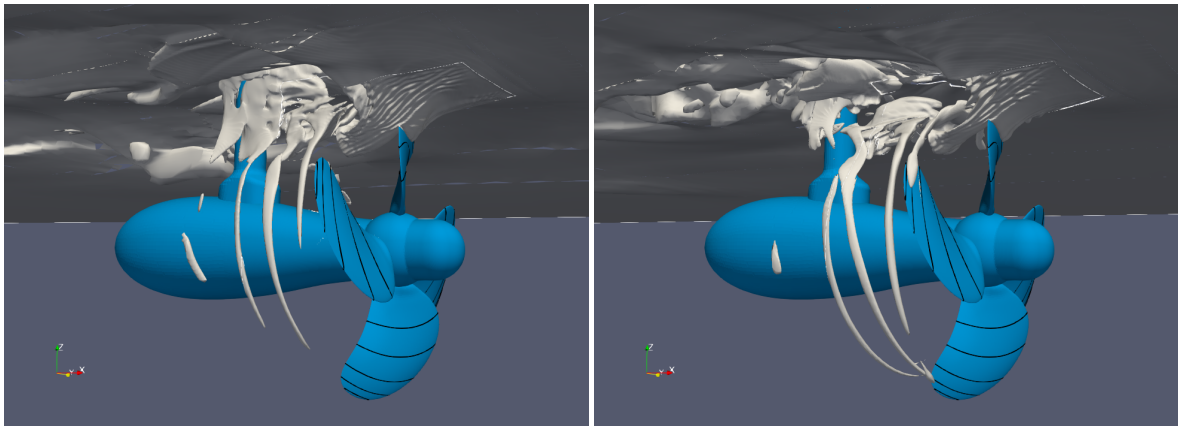

(a) $k-\omega-TNT$ (b) $TNT-EARSM$

Figure 6.15: Application of $EARSM$ shows a longer ventilating tip vortex due to modeled lower pressure in the vortex core.

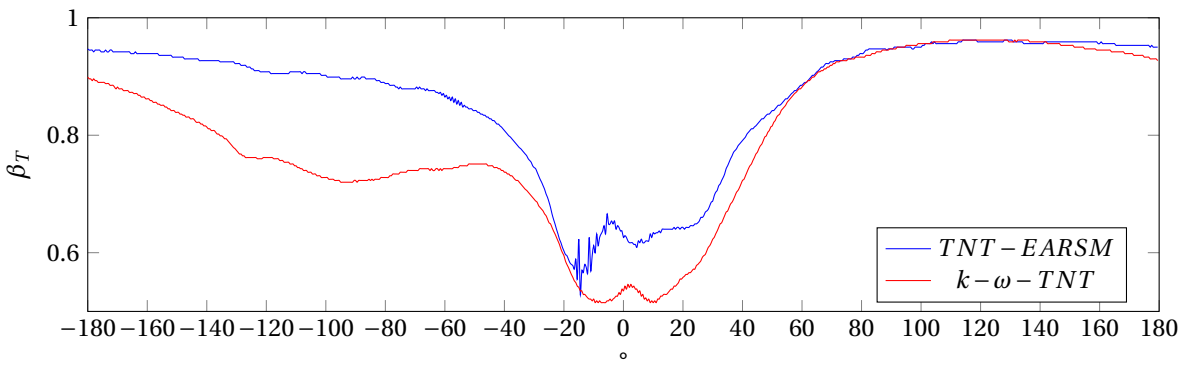

Figure 6.16: Difference in thrust dependent on blade angle. $EARSM$ is slightly more unsteady in the 12 o'clock peak. $k-\omega-TNT$ shows a higher thrust before and in the top position, but this may be due to insufficient force convergence as shown in fig. 6.10 .

6.3.2. Layer of water on the blade

Next to the influence of turbulence, it was found that a thin layer of water was apparent at the blade surface when air was visually attached to it. This may be due to insufficient iterative convergence, such that air has not had the chance to convect through the viscous layer refinement cells. The insufficiency of air transported may be the result, as it is not attached to the blade. It however seems that the thin layer of water is not harming the pressure difference where the blade separates water and air if it is surface breaking, given in the XY-view of the surface piericing blade in fig. 6.17. The thin layer of water (in red in (a)) at the blade surface between air and the blade itself, is not resulting in a similar jump of pressure on the down side of the blade (b). In fig. 6.18, it can be found that pressure is reduced where atmospheric air is found in the areas outside the yellow circle.

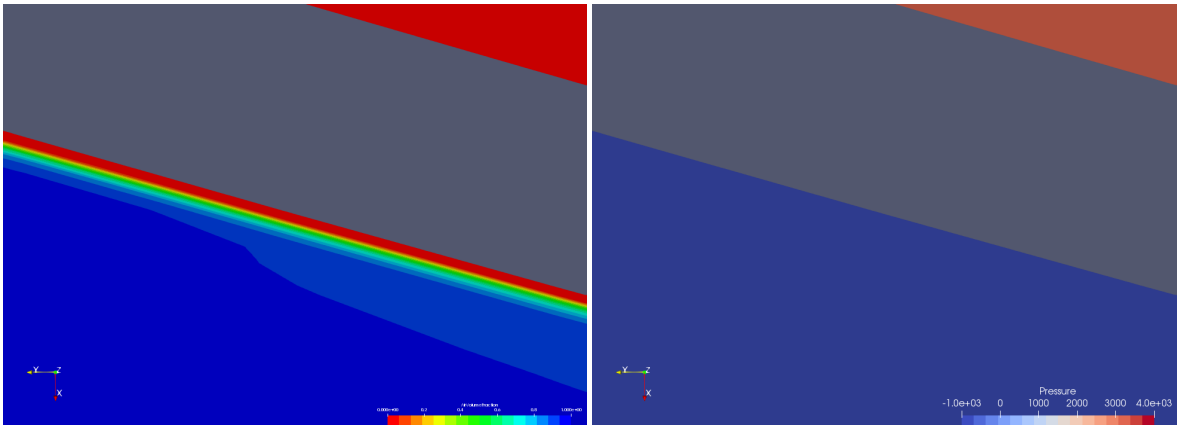

(a) Air-volume fraction

(b) Pressure

Figure 6.17: Zoomed XY-blade cross section of the top blade in surface piercing condition.

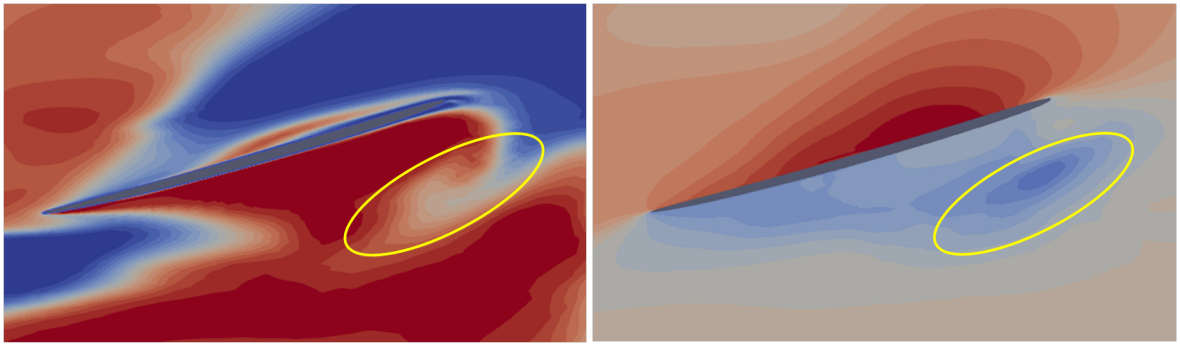

(a) Air-volume fraction; red is air, blue is water.

(b) Pressure; blue is sub-atmospheric, red is super-atmospheric

Figure 6.18: XY-blade cross section of the top blade in surface piercing condition.

It was proposed by Klaij to run the problem using Euler's equations without viscosity, turbulence modeling and a viscous grid layer to solve the equations correctly until the wall. With regard to time, this was not possible, but recommended in further research. In an attempt to obtain correct simulation until the blade wall, contactline correction (extrapolation of the air-volume fraction through the boundary layer cells to the body surface) was applied. As the contactline correction is not developed (and apparently neither suitable) for this problem, the simulation diverged. An other attempt of not resolving the boundary layer by imposing slip-conditions on the propeller blade showed no improved thrust loss and air entrainment.

6.3.3. Ventilation capturing in VoF-solver

Turbulence modeling was shown to not have a key influence on predicting ventilation thrust breakdown. Also regarding the different first and second order convective discretization schemes used in former research; Rotte et al. [68] used SuperBEE, Califano [5] HRIC (which is FOU) and Paik [63] used Harmonic, it may be foreseen that the convective flux discretization of the air-volume ratio neither has a major influence. One may

wonder in what extend the VoF-modeling assumption is limiting in the simulation of ventilation.

It is known that due to the mixing-fluid assumption, bubbly flow is insufficiently simulated. As air is mostly transported in bubbles, it was foreseen to obtain a flow with consists (numerically) out several percents of air. Instead no air is found. One hypothesis is the application of the interpolated density in the VoF-assumption (ref. eq. (3.54)). 5% of air in a cell increases the local density by factor 40. The pressure gradient, underline in ref. eq. (3.19), cannot transport the fluid of higher density anymore. The extend of air may therefore be limited. The hypothesis is supported by improved surface piercing propeller simulations [63], [5], [27], where a significantly more air is drawn, such that air volume in the cell is close to 1 and local density is close to the air density. In those simulations, improved air entrainment and thrust loss was found.

$$\rho(\alpha) = \alpha\rho_a + (1-\alpha)\rho_w \qquad \text{(ref. eq. (3.54))}$$

$$\underline{\rho\frac{D\mathbf{u}}{Dt}} = -\nabla p + \rho\mathbf{g} + \mu\nabla^2\mathbf{u} \qquad \text{(ref. eq. (3.19))}$$

7

Conclusion & recommendation

7.1. Conclusions

Ventilation can be of substantial effect on the usage of vessels, associated with loss of thrust, efficiency and steerability and highly unsteady loading of the propulsor units. Consequences are varying from safety issues to higher fuel consumption. This work mainly focussed on the loss of thrust in an open water application for regular, submerged propellers in low loaded conditions. Effects of a ship hull, oblique inflow, waves and ship motions were excluded from this research. Three major questions were set:

1. What are the major parameters in propeller ventilation and how do those parameters influence the inception and thrust breakdown?
2. To what extend is it possible to predict thrust breakdown experimentally?
3. To what extend is it possible to predict thrust breakdown numerically?

7.1.1. Major parameters

From literature review, it was expected that propeller immersion was the most important parameter. Multiple researches characterized the ventilation regime based on the immersion. In this research, a clear distinction of the ventilation regime on the tip immersion rate was found, but an influence of the thrust loading was also found.

For free surface ventilation inception, a so-called critical advance ratio was used in many works. The critical advance ratio was the advance ratio where severe ventilation thrust breakdown started in the open water diagram, an is a propeller-specific parameter. In a attempt to generalize this parameter, it was shown that the thrust loading coefficient C_T could be used instead. A simple formula for C_T dependent on K_T and J exists.

Using the depth and advance velocity, the non-dimensional pressure gradient or ventilation inception number σ_v was derived. From literature there was however no agreement on which driving pressure at the propeller should be used. Research using an actuator disk in CFD showed that the pressure jump over the propeller plane is governing for free surface ventilation inception, instead of e.g. local pressure on the blade. Therefore the ventilation number is referred to as the ventilation *inception* number and defined according:

$$\sigma_V = \frac{2gh_{tip}}{C_T v_a^2} \qquad \text{(ref. 2.21)}$$

Furthermore free surface ventilation inception was shown to be depending on the immersion rate of the propeller tip and the ability to draw the free surface. The latter is parametrized by the Froude number.

$$I = \frac{h_{tip}}{D} \qquad \text{(ref. 2.14)}$$

$$Fr = \frac{v_a}{\sqrt{gD}} \qquad \text{(ref. 2.25)}$$

Free surface ventilation thrust breakdown showed a similar trend between different runs. A distinction between thrust breakdown due to surface piercing and due to air entrainment was found. In surface-piercing condition, thrust breakdown appeared to be depending on the thrust loading coefficient C_T, comparable to the thrust breakdown derived using the actuator disk model in CFD.

$$\beta = f(\sigma_V \cdot I \cdot Fr) \qquad \text{(ref. 4.4)}$$

Increased ventilation thrust breakdown was found to be different for an equal thrust loading coefficient at different revolution rates, so depending on absolute thrust. As the propeller area is equal, this indicates a dependency on the pressure jump over the propeller plane. The pressure jump and low pressure mainly depends on the local flow velocity, which mainly depends on the propeller rotation rate N. Increased thrust breakdown may therefore be captured in a function of N. Whereas former works showed ventilation numbers and Froude numbers defined using N, a (non-dimensional) number capturing the trend was not found in this work. Furthermore, as only one propeller was studied, a conclusion on the influence of the pitch ratio was neither yield. It is expected that an influence of P/D will be found, which may also leads to further knowedge to derive the dependency on N.

Vortex ventilation inception was the most unstable regime in the experiments. A clear dependency on the thrust loading coefficient C_T, as was in free surface ventilation, was not found. It seems that inception merely depends on local flow phenomena, such as low advance velocity and recirculation of water above the propeller, and on propeller characteristics, such as the tip vortex strength and circulation around the propeller blade. Even more than $1D$ immersed, vortex ventilation inception was found after some time. Later in the experiment (without changing anything), the vortex washed out, indicating a probable time dependency of vortex ventilation. Also a bistability effect was found for vortex ventilation; vortices are washing out at higher velocities than necessary for inception. Vortex ventilation thrust breakdown was found to be small and could not be captured. Mixed ventilation showed the largest variatoions in thrust breakdown and is therefore the most limiting case for propulsive unit breakdown.

7.1.2. Experimental based prediction

Experimental parameters were varied according a statistical research planning, to be able to fit emperical models to the results. For the propeller specific model, third order polynomials in N, I and J, extended with higher order of J as the measurement resolution was higher, were built. It used all data acquired and delivers the absolute thrust breakdown. The generic model used C_T instead of J (according the findings of the actuator disk) and Fr_{nD} instead of N (according Shiba [72]) and delivered the relative thrust breakdown β_T. The generic model used only part of the data. Both models showed a sufficient fit indicated by r^2 exceeding 0.9.

The polynomial model estimated thrust breakdown as if it is continuous. Average thrust breakdown is captured well, although the highly unsteady thrust breakdown due to vortex and mixed ventilation and exact trends of free surface ventilation is not accurate.

7.1.3. Effect of ventilation on vessels

Loss of thrust is found to be substantial. Losses of 60% were found in the performed experiments. Free surface ventilation appeared to give the largest thrust breakdown, showing a major dependence on the immersion of the propeller and propeller thrust loading coefficient. Also the revolution rate seems to be of (minor) influence. As class societies [13] prescribe a minimum clearance of 0.3D to the hull, it is expected that a ship propeller is sufficiently immersed to exclude free surface ventilation. Increasing the propeller diameter at the cost of clearance is increasing probability of free surface ventilation, but still the immersion is expected to be sufficient. Lastly, the working point of a regular propeller, for the C4.55 $P/D = 0.8$ propeller being $J = 0.6$, is in sailing conditions too high to induce ventilation. It is therefore not expected that in normal conditions, (continuous) free surface ventilation thrust breakdown of 60% will be found. Reduced immersion due to waves and ship motions, as well as increased thrust loading in heavy weather of due to a wake peak, make it however more likely to encounter circumstances in which ventilation thrust breakdown can be dangerously large. As wash-out may be slower than a new inception in seagoing timescales, which is the research of Dallinga and Moulijn [10], continuous inception and wash-out might still lead to significant thrust loss. When (near) bollard pull working points are considered, ventilation thrust breakdowns of 60% can be found.

Unsteady torque loading is found simultaneously with thrust breakdown, and showed the largest fluc-

tuations in mixed ventilation, as the thrust breakdown fluctuates between thrust in free surface ventilation and the undisturbed propeller thrust. However, the immersion domain in which mixed ventilation occurs is small with regard to ship motions and highly fluctuating loading are not expected from mixed ventilation. Ship motion leading to continuous surface-piercing, followed by deep immersion may introduce unit breakdown. Most suddenly inception was found in vortex ventilation.

As thrust and torque regularly break down simulaneously, efficiency losses found in this work were small and mostly occuring at high thrust loadings. On the other side, reductions up to 5% are still significant. It needs to be said that efficiency is calculated using torque demand and not engine torque output. Real reduction might even be far higher as torque surplus is axially accelerating the propeller without any increase of thrust due to the fact that engine regulation and revolution limiters are not (rapidly enough) adapting to the unsteady torque load.

7.1.4. Numerical based prediction

Numerically, ventilation thrust breakdown is predicted in model scale by application of CFD. The incompressible viscous fluid solver `ReFRESCO` was used to assess the ability to simulate ventilation. Ventilation and thrust breakdown was found in free-surface and mixed ventilation cases by breaking the free surface, but not in vortex ventilation. However, it appeared that air entrainment and ventilation thrust breakdown was underestimated and pressure build up after ventilation overestimated. If ventilation is found in CFD, one must take it seriously, as higher values of thrust breakdown are most probably to be found.

From literature, it is foreseen that convective flux discretization of the air-volume transport equation was not governing for incorrect thrust breakdown, as multiple different schemes all showed the same trend. With regard to turbulence modeling, application of $EARSM$ instead of a $k-\omega$ and thus excluding Boussinesq's assumption was not changing thrust breakdown. It however showed extended ventilating vortices. Results of scale resolving simulations ($k-\omega-TNT-XLES$ and $SST2003-IDDES$) were not obtained due to difficulties in the convergence of ω at the mixed flow areas, which is a common issue. Overproduction of ω prevented the change from $RaNS$ to LES in the near blade areas.

The origin of insufficient simulation of ventilation may be in the continuous phase assumption of the VoF-model. As ventilation is an advection problem, correct air velocities are of importance. Overestimated local density prevents in the momentum equation from correct velocity, leading to insuffiently convected amount of air.

$$\rho(\alpha) = \alpha\rho_a + (1-\alpha)\rho_w \qquad \text{(ref. eq. (3.54))} \qquad \underline{\rho\frac{D\mathbf{u}}{Dt} = -\nabla p + \rho\mathbf{g} + \mu\nabla^2\mathbf{u}} \qquad \text{(ref. eq. (3.19))}$$

7.2. Recommendations

7.2.1. Major parameters

All conclusions and trends derived in this work are based on only one propeller design. One propeller was sufficient to indicate important parameters and derive relations, but more propellers are required to further improve knowledge and prediction models. Especially in the ventilation extent, a dependency on the revolution rate seems to exist. A similar propeller of different P/D-ratio may support or reject the statement set, as the thrust is not equal for the same revolution rate.

Also propellers designed for higher thrust loadings, which in general have higher tip loadings, are interesting. These propellers are foreseen to be more likely to ventilate. Nozzled propellers are even more likely as the tip loading is increased even more. Next to that, in the working principle of a nozzle, it draws water from even closer to the free surface into the propeller. As ventilation occurred mostly in (near) bollard pull working points, it is interesting to know the effects on bollard pull performances.

7.2.2. Experimental based prediction

Experiments were conducted quasi-steady to obtain ventilation data for various advance ratios. This gave a sufficient amount of data to fit the polynomial models to and to research the ventilation thrust breakdown and inception behaviour in free surface and mixed ventilation. For vortex ventilation, inception was irregular and the quasi-steady approach was not suitable for researching the inception behaviour. Steady calculations may be necessary for fundamental research. Current quasi-steady results can be used to find the inception point.

The parameter variations were based on a Design of Experiment. By using a statistical tool, a proper polynomial model was fitted. As this was one of the goals of this research, application of a DoE was justified.

When applying a DoE, one should be careful that sufficient orders of parameters are included and that orders are nearly equal. However, application of a DoE comes at the cost of multiple runs (mostly deeply immersed) which were not interesting with regard to the free surface ventilation research. One should always be careful if the DoE is a proper tool in the research, as the necessity for a lot of (not interesting) runs can be stringent in the ability to obtain interesting data.

To compare experimental results to numerical simulations, clear camera view of a single blade position is of interest. Whereas during this research no high-speed camera was used, it is recommended to install one during further experiments.

7.2.3. Effect of ventilation on vessels

This research was bound by perfect conditions. An open water set-up with uniform inflow was used and ship motion and waves were excluded. However, in behind conditions, especially for full vessels, a large area around the propeller 12 o' clock position is apparent where flow velocity is reduced. In those areas, likeliness of ventilation increases. Water is drawn from farther above the propeller and vortices might incept in the low speed area. In behind conditions in calm water might be of interest to indicate the influence of the ships wake in the ventilation inception.

Ship motions and waves are reducing the clearance to the free surface. Even surface piercing conditions might occur in heavy seas. Inception is expected regularly and more often in heavy seas. Secondly the orbital motion in waves might transport air to the propeller, when air is dissolved due to wave breaking. Lastly, the propeller is higher and more discontinuously loaded in heavy seas, increasing the ventilation likeliness. Therefore also ship motions and/or waves needs to be taken into account to indicate the increased likeliness of ventilation in heavy seas.

Bollard pull conditions were found to be the most stringent. Tunnel thrusters are normally working in these conditions. These tunnels are normally sufficiently immersed and no contact to the free surface could be made, but severe ship motions could empty the tunnels and ventilation then incepts. The most interesting is wash-out; a large amount of air is apparent when the tunnel is immersed and that air needs to wash-out before the thruster can be used, which might take some time. It is expected that in severe seas, tunnel thrusters can not (reliably) be used. Although this is not ventilation as researched in this work, severe safety issues may result from this ventilation.

To identify the influence of ventilation on efficiency loss, the engine including (anti-spin) limiters should be modeled. Only then one could obtain the efficiency based on torque output of the engine instead of torque demand of the propeller. Anti-spin limiters were already designed by i.a. Smogeli [73].

7.2.4. Numerical based prediction

Scale resolving simulations were not succesful due to overproduction of ω at the mixed fluid areas in k-equation turbulence models, which prevented the switch to scale resolving modes. Several corrections are available, such as the Reboud correction ([9],[67], applied by [37]) and Gaussian correction (by [68]). These corrections may support the change to SRS. However, as excluding Boussinesq's assumption did not change the thrust breakdown, one may wonder if SRS will give a better predicted thrust breakdown.

If the origin of the the insufficient simulations is in the VoF-assumption, then two-fluid approach needs to be considered. In an Euler-Euler simulation, the momentum and mass equations are solved for air and water seperately, instead of once for the assumed mixed flow. This is however not (yet) possible in `ReFRESCO`.

The domain constists of a stationary grid containing the free surface and strut, and a rotating grid containing the propeller. Parameter values are interpolated from one to another at the grid boundaries. For a simplified case of an empty grid, it was found that data interpolation over the grid boundaries was insufficient. Also residuals were high at the boundary. Lemaire [50] showed that for smooth interpolation, the interpolation order should be at least one order higher than discretization orders. A third order interpolation scheme may then be necessary. However, higher order models increase overhead costs significantly. Furthermore issues of interpolation are mostly found behind the propeller and seem not to harm the solution.

Between timesteps, force needs to be sufficiently converged. Most calculations were not fully converged, as this took an excessive amount of outerloops (>150). The maximum number of outerloops is set to 100, to decrease numerical effort. In the scope of this work is was not necessary to fully converge the force, but care needs to be taken if validation or verification studies are conducted.

The domain stretched 5D around the propeller and 10D at the outflow. Still an effect of the boundary conditions was found at the propeller. It is recommended to increase the domain.

Bibliography

[1] M. van den Boogaard. Msc thesis research. 2019.

[2] H. Brandt. Ventilation or cavitation: An experimental study to determine dynamic loads on controllable pitch propellers. *Schiff und Hafen*, 25(5):415–503, 1973.

[3] C. E. Brennen. *Fundamentals of multiphase flow*. Cambridge university press, 2005.

[4] J. Brouwer and G. Hagestein. Experimental investigation of the effect of waves and ventilation in depressurised conditions on a pod-propeller of a cruise liner model, 2013.

[5] A. Califano. Dynamic loads on marine propellers due to intermittent ventilation, phd thesis, 2010.

[6] A. Califano and S. Steen. Analysis of different propeller ventilation mechanisms by means of rans simulations. In *Proceedings of The First International Symposium on Marine Propulsors*, 2009.

[7] A Califano and S Steen. Identification of ventilation regimes of a marine propeller by means of dynamic-loads analysis. *Ocean Engineering*, 38(14-15):1600–1610, 2011.

[8] A Califano and S Steen. Numerical simulations of a fully submerged propeller subject to ventilation. *Ocean engineering*, 38(14-15):1582–1599, 2011.

[9] Olivier Coutier-Delgosha, R Fortes-Patella, and Jean-Luc Reboud. Evaluation of the turbulence model influence on the numerical simulations of unsteady cavitation. *Journal of Fluids Engineering*, 125(1): 38–45, 2003.

[10] R. Dallinga and J. Moulijn. Influence of ventilation in seagoing timescales. 2019.

[11] Damen. Combi coaster 2750, 2017. URL `https://products.damen.com/-/media/Products/Images/Clusters-groups/Shipping/Combi-Coaster/CC-2750/Documents/Product_Sheet_Damen_Combi_Coaster_2750_09_2017.pdf`.

[12] J. Dang, H.J.J. Van den Boom, and J.T. Ligtelijn. The wageningen c-and d-series propellers. In *12th International Conference on Fast Sea Transportation FAST*, 2013.

[13] DNV. *Rules for classification of ships*, chapter 3.3.2, page 9. DNV, January 2000.

[14] H Dol, J Kok, and B Oskam. Turbulence modelling for leading-edge vortex flows. In *40th AIAA Aerospace Sciences Meeting & Exhibit*, page 843, 2002.

[15] L. Eça and M. Hoekstra. Evaluation of numerical error estimation based on grid refinement studies with the method of the manufactured solutions. *Computers & Fluids*, 38(8):1580–1591, 2009.

[16] L. Eça and M. Hoekstra. A procedure for the estimation of the numerical uncertainty of cfd calculations based on grid refinement studies. *Journal of Computational Physics*, 262:104–130, 2014.

[17] L. Eça, G. Vaz, and M. Hoekstra. On the role of iterative errors in unsteady flow simulations. *n.n.*, 2018.

[18] K.P. Fleischer. *Freifahrtversuche bei Unterdruck mit teilgetauchten Propellern*. Forschungszentrum des Dt. Schiffbaus, 1979.

[19] Kuiper. G. *The Wageningen Propeller Series*. MARIN, 1992.

[20] DNV GL. Tip vortex and ventilation inception on a surface-piercing hydrofoil, 2005. URL `https://www.youtube.com/watch?v=NefnpuxS2uM`.

[21] W. Guoqiang, J. Dashan, C. Meiliang, and S. Zhenbang. Propeller air ventilation and performance of ventilated propeller. In *Fourth international symposium on Practical Design of Ships and Mobile Units*, volume 1, pages 6–1, 1989.

[22] F. Gutsche. Einfluss der tauchung auf schub und wirkungsgrad von schiffspropellern. *Shiffbauforschung*, 6(5):6, 1967.

[23] J.B. Hadler and R. Hecker. Performance of partially submerged propellers. *7th ONR Symposhium on Naval Hydrodynamics-Rome,(August 1968)*, 1968.

[24] G.P.J.J. Hagesteijn and J. Brouwer. The relation between propeller ventilation and loss of thrust and torque, august 2016.

[25] C. M. Harwood, K.A. Brucker, F. Miguel, Y.L. Young, and S.L. Ceccio. Experimental and numerical investigation of ventilation inception and washout mechanisms of a surface-piercing hydrofoil. In *30th Symposium on Naval Hydrodynamics, Hobart, Australia, Nov*, pages 4–7, 2014.

[26] A.D. Hay. Flow about semi-submerged cylinders of finite length. *Princeton University: Princeton University*, page 178, 1947.

[27] K. Himei. Numerical analysis of unsteady open water characteristics of surface piercing propeller. In *The Third International Symposium on Marine Propulsors smp*, volume 13, 2013.

[28] E. Huse. Propeller-hull vortex cavitation. Technical report, Technical University of Norway, 1971.

[29] E. Huse. Propeller–hull vortex cavitation. *International Shipbuilding Progress*, 19(212):111–125, 1972.

[30] ITTC. Notes of 1934 international towing tank conference, londen. Technical report, International Towing Tank Conference, 1934.

[31] H. Johansen. Windsurf - spin out, 2005. URL `https://www.youtube.com/watch?v=zD34ER4eVeo`.

[32] jorodmon. General carge ship arklow wave leaving a coruna, 2015. URL `https://www.youtube.com/watch?v=pfueinOgX1I`.

[33] J. auf 'm Keller. Enige aspecten bij het ontwerpen van scheepsschoeven. *Schip en Werf*, 1966.

[34] K. Keller, T.and Hochkirch, J Henrichs, and A. Cura-Hochbaum. Numerical simulations of a surface piercing a-class catamaran hydrofoil and comparison against model tests. *The 22nd Chesaopake Sailing Yacht Symposium*, 2016.

[35] G. Kempf. *Immersion of propellers*. North East Coast Institution of Engineers and Shipbuilders, 1934.

[36] C.M. Klaij, M. Hoekstra, and G. Vaz. Design, analysis and verification of a volume-of-fluid model with interface-capturing scheme. *Computers & Fluids*, 170:324–340, 2018.

[37] M. Klapwijk, G. Rotte, M. Kerkvliet, and T. van Terwisga. Modelling of the plume of a submerged exhaust system. In *Proceedings of the 20th numerical towing tank symposium*, pages 2–3, 2017.

[38] M.D. Klapwijk. Msc thesis research. 2017.

[39] H. Klein Woud and D. Stapersma. *Design of propulsion and electric power generation systems*. IMarEST, 2002.

[40] J. C. Kok. Resolving the dependence on freestream values for the k-turbulence model. *AIAA journal*, 38 (7):1292–1295, 2000.

[41] J.C. Kok, H. Dol, B. Oskam, and H. van der Ven. Extra-large eddy simulation of massively separated flows. In *42nd AIAA Aerospace Sciences Meeting and Exhibit*, page 264, 2004.

[42] K. Koushan. Dynamics of ventilated propeller blade loading on thrusters due to forced sinusoidal heave motion. In *26th Symposium on Naval Hydrodynamics, Rome, Italy, Sept*, pages 17–22, 2006.

[43] A. M. Kozlowska, S. Steen, and K. Koushan. Classification of different type of propeller ventilation and ventilation inception mechanism. In *First International Symposium on Marine Propulsor, Trondheim, Norway, June*, volume 9, pages 342–349, 2009.

[44] A.M. Kozlowska and S. Steen. Experimental analysis on the risk of vortex ventilation and the free surface ventilation of marine propellers. *Applied Ocean Research*, 67:201–212, 2017.

[45] A.M. Kozlowska, K. Wöckner, S. Steen, T. Rung, K. Koushan, and S. Spence. Numerical and experimental study of propeller ventilation. In *Proceedings of the 2nd International Symposium on Marine Propulsors (SMP'11)*, 2011.

[46] C. Kruppa. Testing of partially submerged propellers. Technical report, International Towing Tank Conference, 1972.

[47] P. Kundu, I. Cohen, and Dowling D. *Fluid Mechanics*. Academic Press, 6th edition, 2015.

[48] J. Lafeber, F.H.and Brouwer and J. Dang. A quasi-steady method for efficiently conducting open water model tests. In *Proceedings of 3rd International Conference on Advanced Model Measurement–Technologies for the Maritime Industry*, 2013.

[49] W. van Lammeren. Weerstand en voortstuwing van schepen, 1942.

[50] S. Lemaire. Presentation overset grids and interpolation, mei 2019.

[51] T. Lloyd, G. Vaz, D. Rijpkema, and A. Reverberi. Computational fluid dynamics prediction of marine propeller cavitation including solution verification, 2017.

[52] MARIN. Depressurized wave basin, 2018. URL `http://www.marin.nl/web/Facilities-Tools/Basins/Depressurised-Wave-Basin.htm`.

[53] MARIN. *ReFRESCO Theory Manual*, 2019.

[54] J.i Martio, T. Sipilä, A. Sanchez-Caja, I. Saisto, and T. Siikonen. Evaluation of the propeller hull vortex using a rans solver. In *Second International Symposium on Marine Propulsors smp*, volume 11, 2011.

[55] F.R. Menter. Improved two-equation k-omega turbulence models for aerodynamic flows. Technical report, NASA, 1992.

[56] F.R. Menter. Influence of freestream values on k-omega turbulence model predictions. *AIAA journal*, 30 (6):1657–1659, 1992.

[57] M. Merkens. The numerical b-series propellers, 2018.

[58] K. Minsaas, O. Faltinsen, and B. Persson. On the importance of added resistance, propeller immersion and propeller ventilation for large ships in a seaway. *n.n.*, 1983.

[59] Anthony F. Molland, Stephen R. Turnock, and Dominic A. Hudson. *Propeller Characteristics*, page 277–312. Cambridge University Press, 2 edition, 2017. doi: 10.1017/9781316494196.014.

[60] T.M. Nieuwstadt, J. Westerweel, and B.J. Boersma. *Turbulence*. Springer, 2016.

[61] H. Oberembt. Zur bestimmung der instationären flügelkräfte bei einem propeller mit aus dem wasser herausschlagenden flügeln, 1968.

[62] N. Olofsson. *Force and flow characteristics of a partially submerged propeller*. Chalmers University of Technology, 1996.

[63] K. Paik. Numerical study on the performance of a partially submerged propeller in bollard condition. In *Fifth International Symposium on Marine Propulsors smp*, 2017.

[64] F.S. Pereira, L. Eça, and G. Vaz. Simulation of wingtip vortex flows with reynolds-averaged navier–stokes and scale-resolving simulation methods. *AIAA Journal*, pages 1–17, 2019.

[65] M. Pohl. Untersuchung des lufteinbruchs bei schiffspropellern. *Jahrbuch der Schiffbautechnischen Gesellschaft*, 81, 1986.

[66] M. Pohl. Untersuchung des lufteinbruchs bei schiffspropellern, 1986.

[67] Jean-Luc Reboud, Benoit Stutz, and Olivier Coutier. Two phase flow structure of cavitation: experiment and modeling of unsteady effects. In *3rd International Symposium on Cavitation CAV1998, Grenoble, France*, volume 26, 1998.

[68] G. Rotte, M. Kerkvliet, and T. van Terwisga. On the influence of eddy viscosity in the numerical modelling of air cavities, 2018.

[69] K. Sato, J. Matsuba, and Yoshinari K. Air draw phenomena on a propeller. *Shipbuilding Research Centre of Japan*, 2, 1984.

[70] K. Sato, R. Tasaki, and S. Nishivama. Observation of flow on a horizontal flat plate above a working propeller and physics of propeller-hull vortex cavitation. *Proceedings of International Sumposium on Propeller and Cavitation*, 1986.

[71] H. Schlichting and K. Gersten. *Boundary-layer theory*. Springer, 2016.

[72] H. Shiba. Air-drawing of marine propellers. *Report of transportation technical research institute*, 9:1–320, 1953.

[73] Ø. N. Smogeli. *Control of marine propellers: from normal to extreme conditions*. Fakultet for ingeniørvitenskap og teknologi, 2006.

[74] P.D. Swales, A.J. Wright, R.C. McGregor, and R. Rothblum. The mechanism of ventilation inception on surface piercing foils. *Journal of Mechanical Engineering Science*, 16(1):18–24, 1974.

[75] T. Van Beek and T. Van Terwisga. Ventilation or cavitation: An experimental study to determine dynamic loads on controllable pitch propellers. *CAV2006*, 2006.

[76] A. van der Ploeg. On grid dependence and iterative convergence of refresco computations, februari 2019.

[77] H. Wagner. Über die entstehung des dynamischen auftriebes von tragflügeln. *ZAMM-Journal of Applied Mathematics and Mechanics/Zeitschrift für Angewandte Mathematik und Mechanik*, 5(1):17–35, 1925.

[78] H. Weller. 7.5 total variation diminishing advection schemes, 2016. URL `https://www.youtube.com/watch?v=5x6vVKhgzgU`.

[79] F.M. White. *Viscous Fluid Flow*. McGraw Hill Education, 3rd edition, 2011.

[80] V.A. Wieleman, B. Schuiling, and P. Crepier. Research for 'verification and validation of full-scale propulsion analysis using cfd', msc thesis, 2018.

[81] Wikipedia. Compressible flow, 2018. URL `https://en.wikipedia.org/wiki/Compressible_flow`.

[82] Wikipedia. Momentum theory, 2019. URL `https://en.wikipedia.org/wiki/Momentum_theory`.

[83] D.C. Wilcox. Reassessment of the scale-determining equation for advanced turbulence models. *AIAA journal*, 26(11):1299–1310, 1988.

[84] A.B. Wood. *Textbook of sound: being an account of the physics of vibrations with special reference to recent theoretical and technical developments*. G Bell And Sons, London, 1930.

[85] E. Yari and H. Ghassemi. Numerical analysis of surface piercing propeller in unsteady conditions and cupped effect on ventilation pattern of blade cross-section. *Journal of Marine Science and Technology*, 21(3):501–516, 2016.

[86] Y.L. Young and B.R. Savander. Numerical analysis of large-scale surface-piercing propellers. *Ocean engineering*, 38(13):1368–1381, 2011.

[87] Y.L. Young, C.M. Harwood, F.M. Montero, J.C. Ward, and S.L. Ceccio. Ventilation of lifting bodies: Review of the physics and discussion of scaling effects. *Applied Mechanics Reviews*, 69(1):010801, 2017.

A

Derivation of RaNS-equations

Derivation of the RaNS-equations is being performed by substituting the sum of a average value and its fluctuations for several quantities in the Navier-Stokes equations and then time averaging the equations.

The average is defined as the time average over the time domain of the simulation. Fluctuations are defined as the difference between the time dependent value and the average. Due to this definition, the time average of the fluctuating part is zero. To show this, averaging identities are given and used.

$$\overline{Q} = \lim_{T\to\infty} \frac{1}{T} \int_T Q(t)\,dt$$
$$Q' = Q(t) - \overline{Q}$$

Averaging identities:

1. $Q_1 = Q_2$ gives $\overline{Q_1} = \overline{Q_2}$
2. $\overline{Q_1 + Q_2} = \overline{Q_1} + \overline{Q_2}$
3. $\overline{\overline{Q}} = \overline{Q}$
4. $\overline{\overline{Q_1} \cdot Q_2} = \overline{Q_1} \cdot \overline{Q_2} \neq \overline{Q_1 \cdot Q_2}$
5. $\overline{\frac{dQ}{ds}} = \frac{d\overline{Q}}{ds}$

It can be shown using the identities above that the average of Q' equals 0:

$$Q = \overline{Q} + Q'$$
$$\overline{Q} = \overline{\overline{Q} + Q'} \qquad id.1$$
$$\overline{Q} = \overline{\overline{Q}} + \overline{Q'} \qquad id.2$$
$$\overline{Q} = \overline{Q} + \overline{Q'} \qquad id.3$$
$$\overline{Q'} = \overline{Q} - \overline{Q} = 0$$

Substitution of the following quantities in the mass and momentum conservation equations is applied. Note that the temperature θ and density ρ are already considered constant and thus these are not seperated.

$$u_i = \overline{u_i} + u_i'$$
$$p = \overline{p} + p'$$

A.1. Mass Conservation

To derive the mass conservation in RaNS-equations, the mass conservation equation is averaged over time.

$$\begin{aligned}
\overline{\nabla \cdot u_i} &= \\
\overline{\nabla \cdot (\overline{u_i} + u_i')} &= \\
\overline{\nabla \cdot \overline{u_i} + \nabla \cdot u_i'} &= \\
\overline{\nabla \cdot \overline{u_i}} + \overline{\nabla \cdot u_i'} &= && id.2 \\
\nabla \cdot \overline{\overline{u_i}} + \nabla \cdot \overline{u_i'} &= && id.5 \\
\nabla \cdot \overline{u_i} + 0 &= \nabla \cdot \overline{u_i} && id.3
\end{aligned}$$

A.2. Momentum Conservation

The same principle is applied for the momentum equation. Recall eq. (3.19).

$$\rho \frac{D\mathbf{u}}{Dt} = -\nabla p + \rho \mathbf{g} + \mu \nabla^2 \mathbf{u} \qquad \text{(ref. 3.19)}$$

$$\rho\left(\frac{\partial \mathbf{u}}{\partial t} + \mathbf{u} \cdot \nabla \mathbf{u}\right) = -\nabla p + \rho \mathbf{g} + \mu \nabla^2 \mathbf{u} \qquad \text{(A.1)}$$

Then the time average can be found below. Please note that ρ is equal to $\overline{\rho}$, such that identity 4 may be used.

$$\begin{aligned}
\overline{\rho\left(\frac{\partial \mathbf{u}}{\partial t} + \mathbf{u} \cdot \nabla \mathbf{u}\right)} &= \overline{-\nabla p + \mathbf{F} + \mu \nabla^2 \mathbf{u}} \\
\overline{\overline{\rho}\left(\frac{\partial \mathbf{u}}{\partial t} + \mathbf{u} \cdot \nabla \mathbf{u}\right)} &= \overline{-\nabla p + \mathbf{F} + \mu \nabla^2 \mathbf{u}} \\
\overline{\rho}\left(\frac{\partial \mathbf{u}}{\partial t} + \mathbf{u} \cdot \nabla \mathbf{u}\right) &= \overline{-\nabla p + \mathbf{F} + \mu \nabla^2 \mathbf{u}} && id.4 \\
\overline{\rho}\left(\frac{\partial \overline{(\overline{\mathbf{u}} + \mathbf{u}')}}{\partial t} + \overline{\mathbf{u} \cdot \nabla \mathbf{u}}\right) &= -\nabla(\overline{p + p'}) + \overline{\mathbf{F}} + \mu \nabla^2 (\overline{\mathbf{u} + \mathbf{u}'}) && id.2,3,5 \\
\overline{\rho}\left(\frac{\partial \overline{\mathbf{u}}}{\partial t} + \overline{\mathbf{u} \cdot \nabla \mathbf{u}} + \overline{\mathbf{u'} \cdot \nabla \mathbf{u'}}\right) &= -\nabla \overline{p} + \mathbf{F} + \mu \nabla^2 \overline{\mathbf{u}} \\
\overline{\rho}\left(\frac{\partial \overline{\mathbf{u}}}{\partial t} + \overline{\mathbf{u} \cdot \nabla \mathbf{u}}\right) &= -\nabla \overline{p} + \mathbf{F} + \mu \nabla^2 \overline{\mathbf{u}} - \overline{\rho} \overline{\mathbf{u'} \cdot \nabla \mathbf{u'}} \\
\rho \frac{D\overline{\mathbf{u}}}{Dt} &= -\nabla \overline{p} + \mathbf{F} + \mu \nabla^2 \overline{\mathbf{u}} - \overline{\rho} \overline{\mathbf{u'} \cdot \nabla \mathbf{u'}}
\end{aligned}$$

The last term on the RHS, $-\overline{\rho}\overline{\mathbf{u'} \cdot \nabla \mathbf{u'}}$ is known to be the Reynolds stress.

B

Scaling laws

Two used scaling methods are scaling according Reynolds number (to obtain correct viscous scaling) and Froude scaling (to obtain correct free surface and ventilation number scaling). In scaling derivations subscript f denotes full scale and subscript m denotes model scale.

B.1. Reynolds Scaling

In this section, Reynolds scaling coefficients are derived.

$$Re = \frac{vL}{\nu} \tag{B.1}$$

geometric similarity	$\alpha_L = L_f / L_m$
kinematic similarity	$\alpha_J = 1 \rightarrow J_f = J_m$
dynamic viscous similarity	$\alpha_{Re} = 1 \rightarrow Re_f = Re_m$

The result for the velocity scale factor α_v can be found below. It is applied that α_ν equals 1, as the kinematic viscosity is generally unscaled (although scaling of ν had been used by Shiba [72]).

$$\begin{aligned} Re_f &= Re_m \\ \frac{v_f L_f}{\nu} &= \frac{v_m L_m}{\nu} \\ \alpha_v = \frac{v_f}{v_m} &= \frac{\nu}{\nu}\frac{L_m}{L_f} = \frac{1}{\alpha_L} \end{aligned}$$

Using the obtained result, the scale factor for revolutions and time can be derived.

$$\begin{aligned} J_f &= J_m \\ \frac{v_f}{n_f D_f} &= \frac{v_m}{n_m D_m} \\ \alpha_n = \frac{n_f}{n_m} = \frac{v_f D_m}{v_m D_f} &= \frac{v_f}{v_m}\frac{D_m}{D_f} = \alpha_v \frac{1}{\alpha_L} = \frac{1}{\alpha_L}\frac{1}{\alpha_L} = \frac{1}{\alpha_L^2} \\ \alpha_t = \frac{1}{\alpha_n} &= \alpha_L^2 \end{aligned}$$

B.2. Froude Scaling

In this appendix, one can find the derivation of Froude scaling. This will be done equalling the depth Froude number of both scales, but it is shown that this also leads to an equality in ventilation number σ.

$$Fr = \frac{v}{\sqrt{gL}} \tag{B.2}$$

geometric similarity	$\alpha_L = L_f / L_m$
kinematic similarity	$\alpha_J = 1 \rightarrow J_f = J_m$
dynamic grav. similarity	$\alpha_{Fr} = 1 \rightarrow Fr_f = Fr_m$

The result for the velocity scale factor α_v can be found below. It is applied that α_g equals 1, as the gravity constant is impossible to scale is this application.

$$\begin{aligned} Fr_f &= Fr_m \\ \frac{v_f}{\sqrt{gL_f}} &= \frac{v_m}{\sqrt{gL_m}} \\ \alpha_v = \frac{v_f}{v_m} &= \frac{\sqrt{gL_f}}{\sqrt{gL_m}} = \sqrt{\frac{g}{g}}\sqrt{\frac{L_f}{L_m}} = 1 \cdot \sqrt{\alpha_L} = \sqrt{\alpha_L} \end{aligned}$$

Using the obtained result, the scale factor for revolutions and time can be derived.

$$\begin{aligned} J_f &= J_m \\ \frac{v_f}{n_f D_f} &= \frac{v_m}{n_m D_m} \\ \alpha_n = \frac{n_f}{n_m} = \frac{v_f D_m}{v_m D_f} &= \frac{v_f}{v_m}\frac{D_m}{D_f} = \frac{1}{\alpha_L}\alpha_v = \frac{1}{\alpha_L}\sqrt{\alpha_L} = \frac{1}{\sqrt{\alpha_L}} \\ \alpha_t = \frac{1}{\alpha_n} &= \sqrt{\alpha_L} \end{aligned}$$

B.3. Scaling of ventilation number σ_V

The Froude scaling is applied on ventilation number σ_V. According to the definition given in eq. (2.21) and its derivation, it is given as:

$$\sigma_V = \frac{2gh_{tip}}{C_T v_a^2} \tag{B.3}$$

It can be shown that the ventilation number is equal for model and full scale.

$$\sigma_{v,f} = \frac{2gh_{tip,f}}{v_{a,f}^2} = \frac{2g\alpha_L h_{tip,m}}{(\alpha_v v_{a,m})^2} = \frac{\alpha_L}{\alpha_v^2}\frac{2gh_{tip,m}}{v_{a,m}^2} = \frac{\alpha_L}{\sqrt{\alpha_L}^2}\frac{2gh_{tip,m}}{v_{a,m}^2} = \frac{\alpha_L}{\alpha_L}\frac{2gh_{tip,m}}{v_{a,m}^2} = \frac{2gh_{tip,m}}{v_{a,m}^2} = \sigma_{v,m}$$

C

Experimental results

C.1. Results in OWD

In this appendix, raw data of the experiments can be found for the experimental test found in table 5.1 and fig. 5.4. All data is property of MARIN and may not be used without permission.

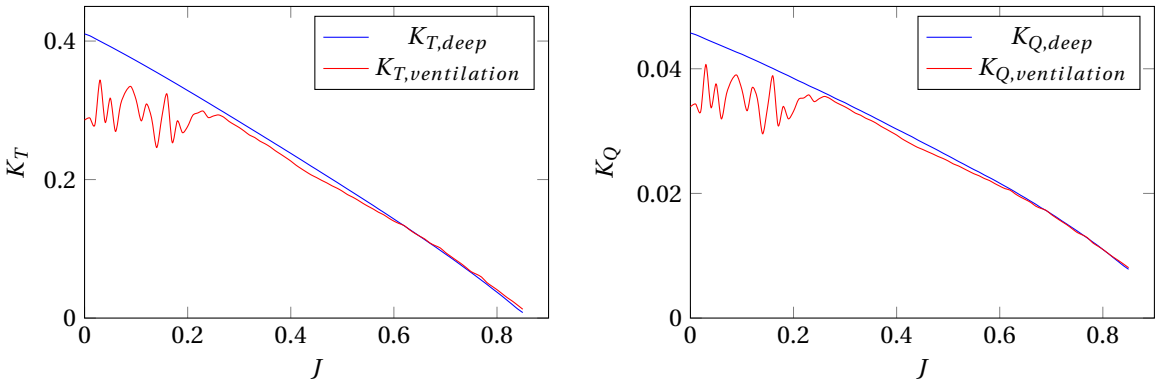

Figure C.1: Run 1: I=0.15[-], N=600[rpm]

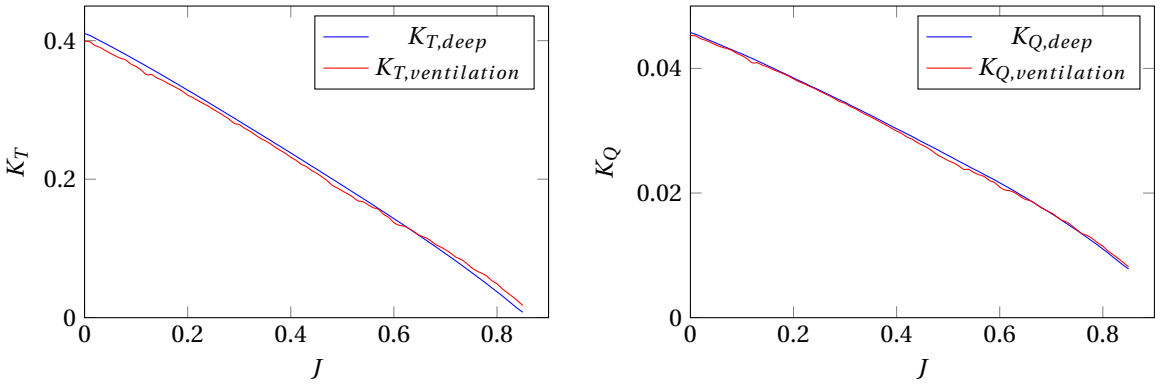

Figure C.2: Run 2: I=0.255[-], N=524[rpm]

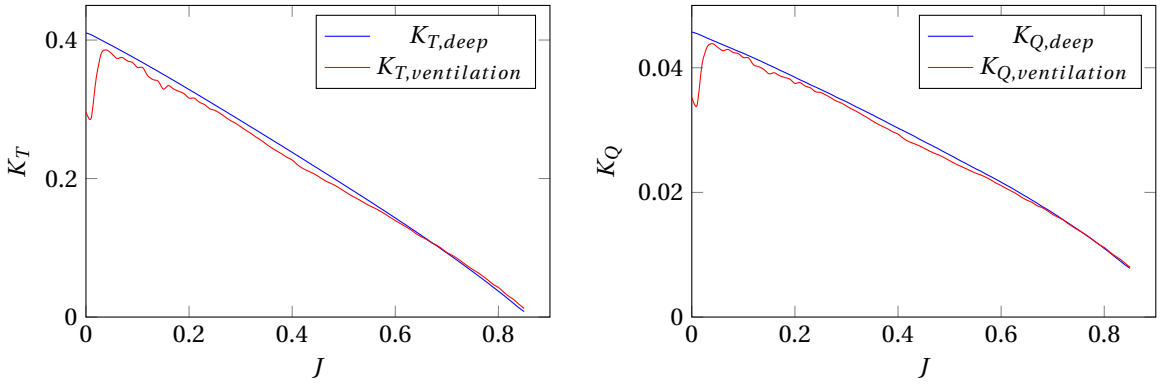

Figure C.3: Run 3 (Re-run of 1): I=0.15[-], N=600[rpm]

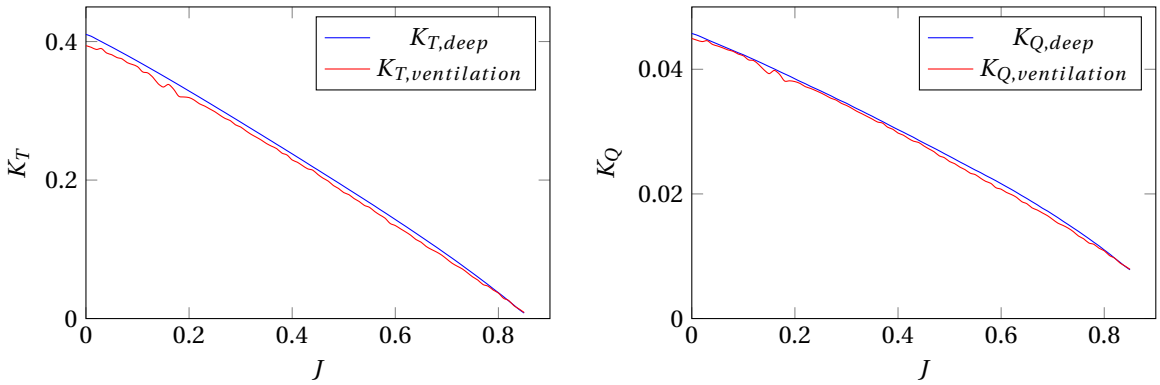

Figure C.4: Run 4: I=0.15[-], N=400[rpm]

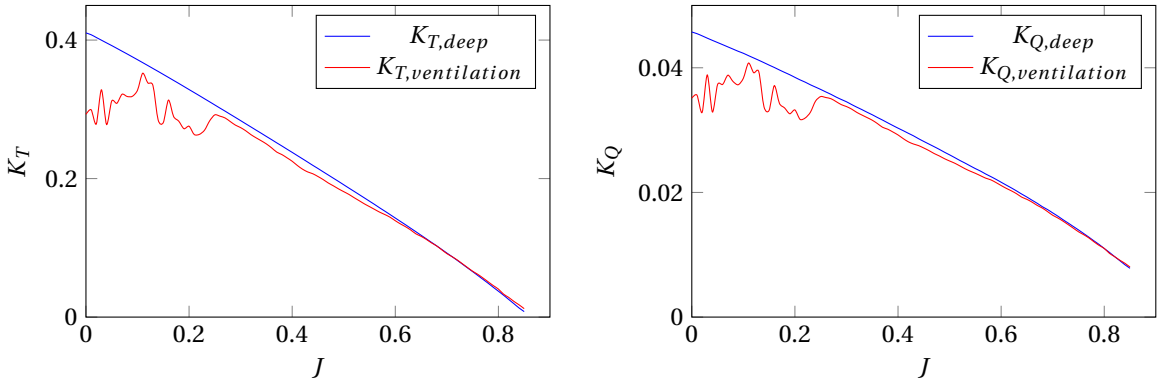

Figure C.5: Run 5 (Re-run of 1): I=0.15[-], N=600[rpm]

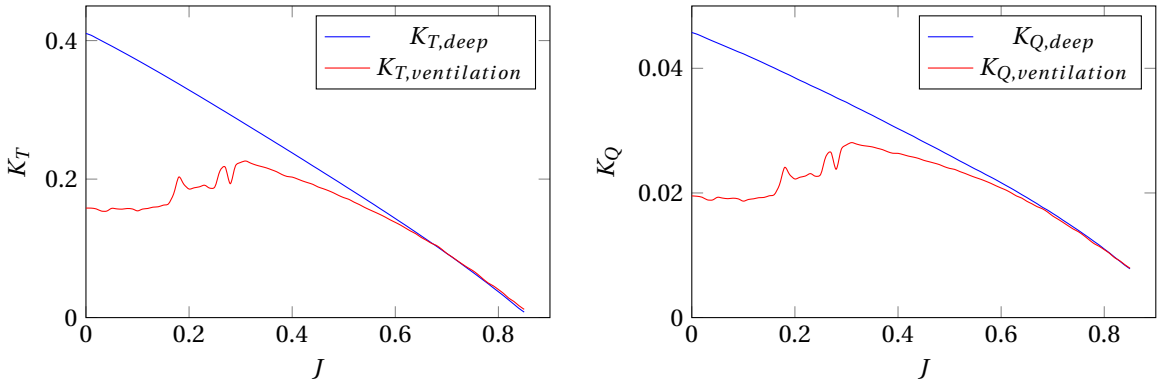

Figure C.6: Run 6: I=0.045[-], N=740[rpm]

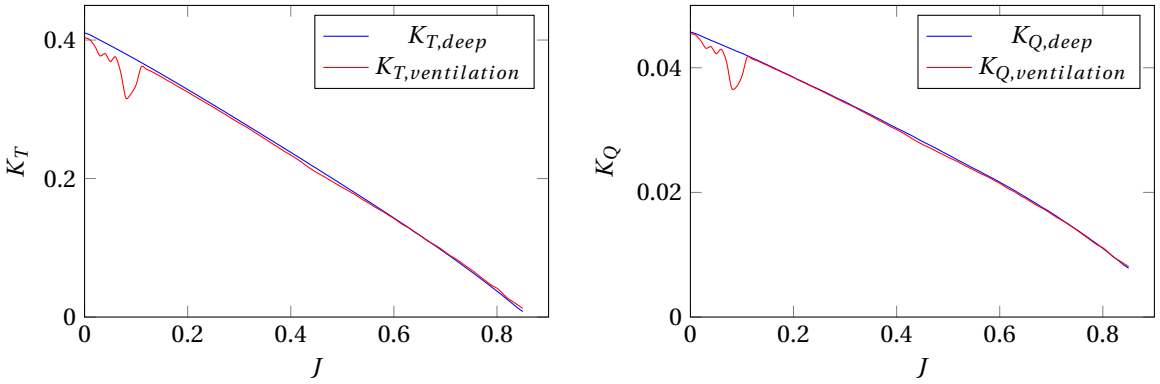

Figure C.7: Run 7: I=0.30[-], N=600[rpm]

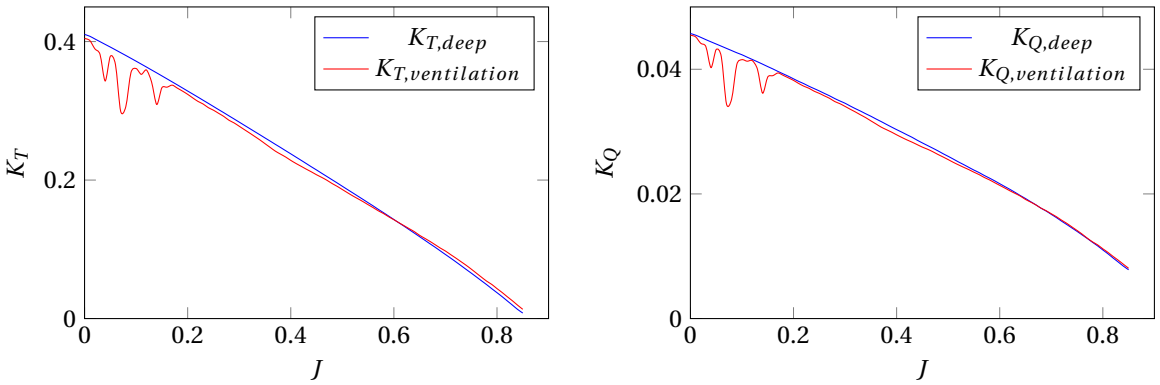

Figure C.8: Run 8: I=0.0255[-], N=740[rpm]

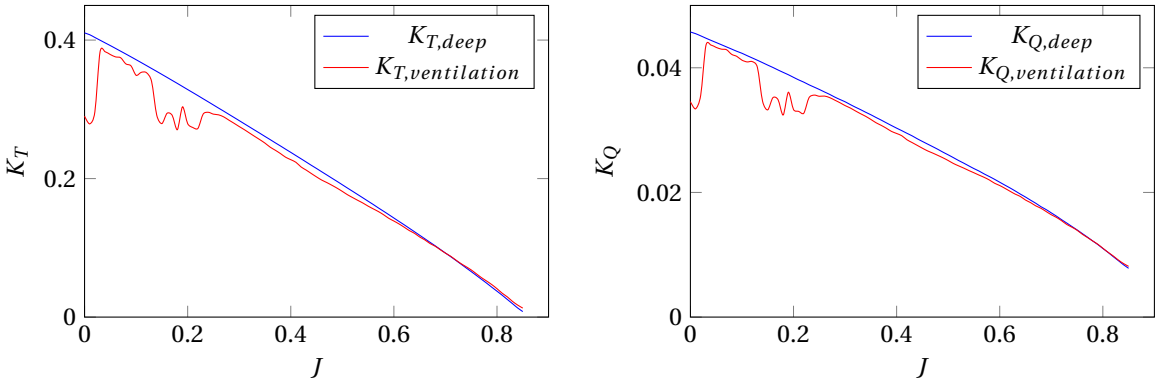

Figure C.9: Run 9 (Re-run of 1): I=0.15[-], N=600[rpm]

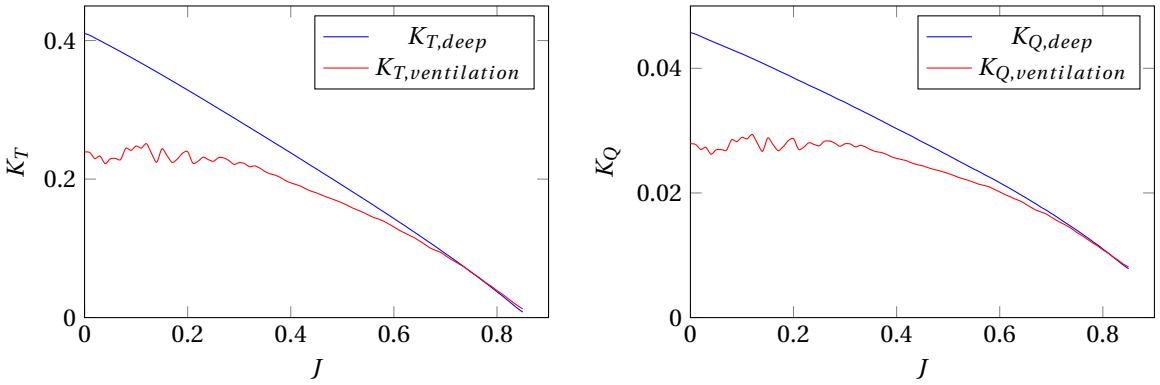

Figure C.10: Run 10: I=0.00[-], N=600[rpm]

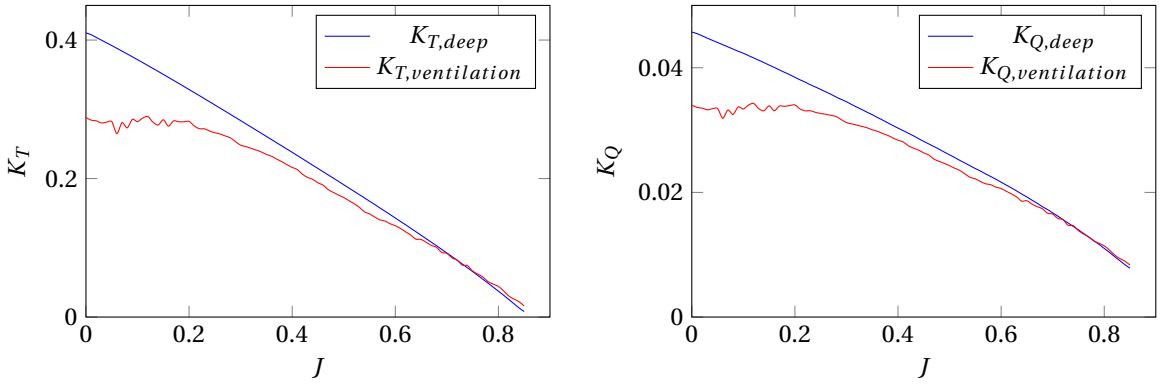

Figure C.11: Run 11: I=0.045[-], N=460[rpm]

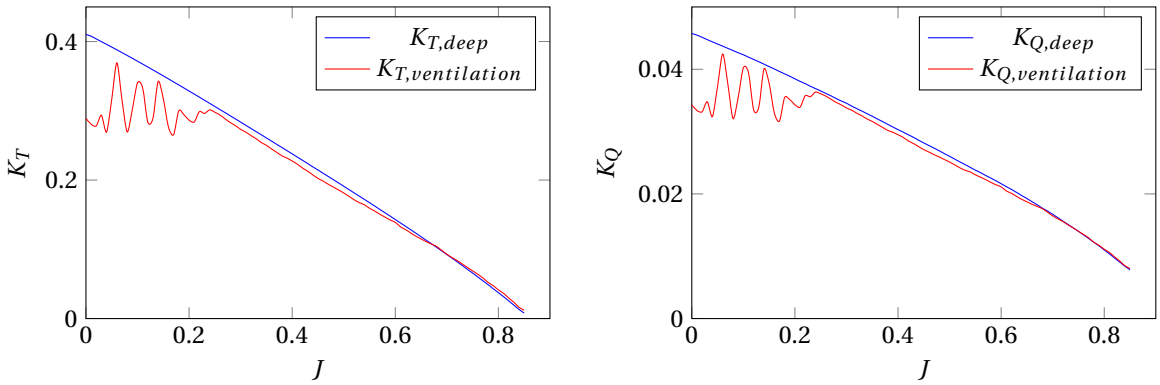

Figure C.12: Run 12 (Re-run of 1): I=0.15[-], N=600[rpm]

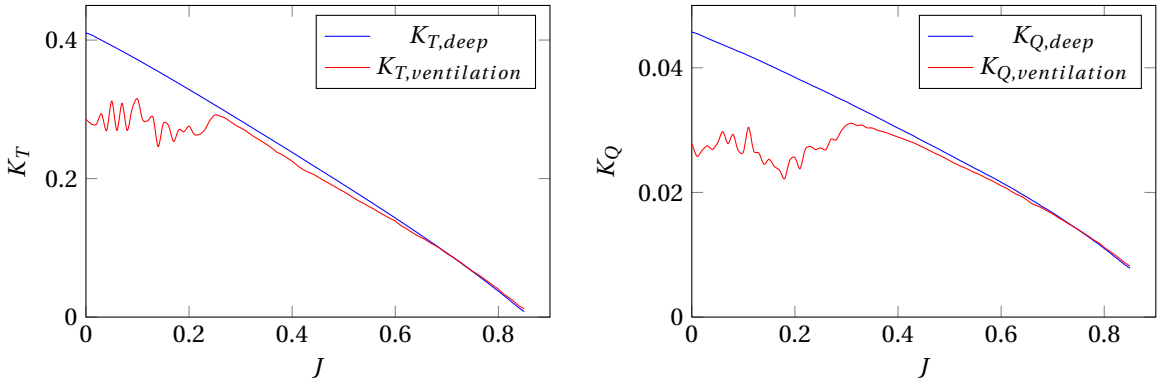

Figure C.13: Run 13: I=0.15[-], N=800[rpm]

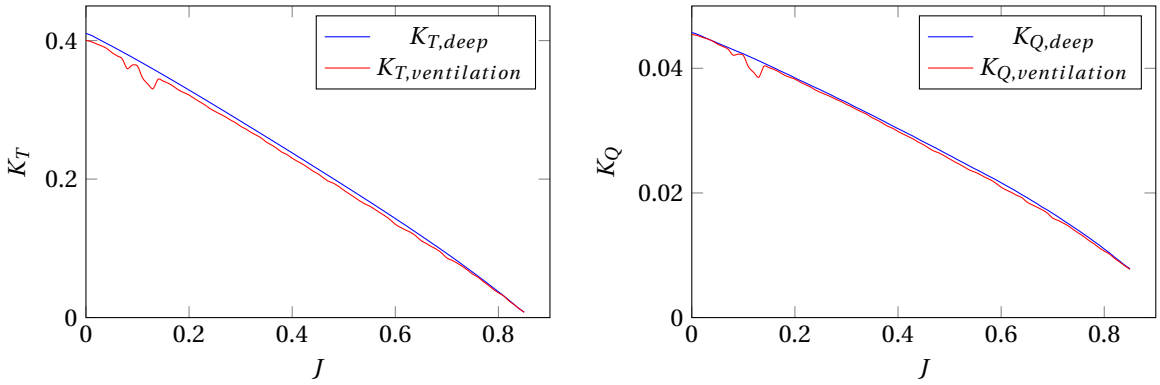

Figure C.14: Run 14: I=0.207[-], N=516[rpm]

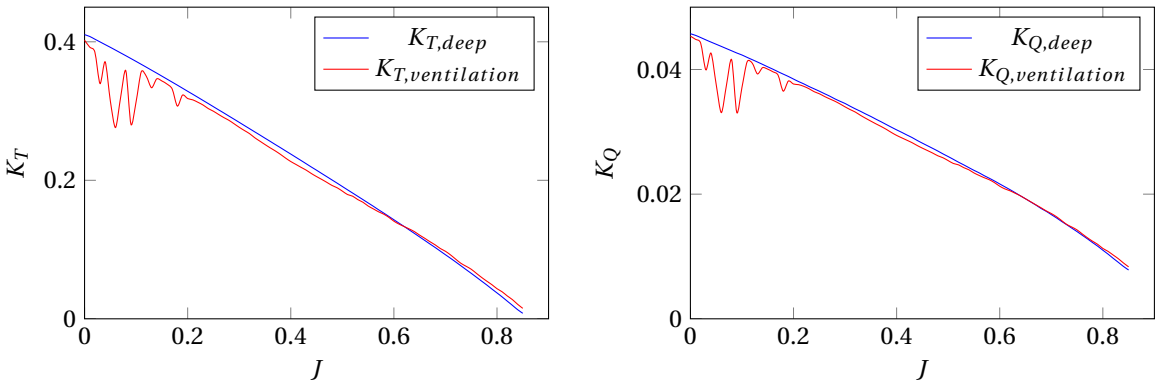

Figure C.15: Run 15: I=0.21[-], N=680[rpm]

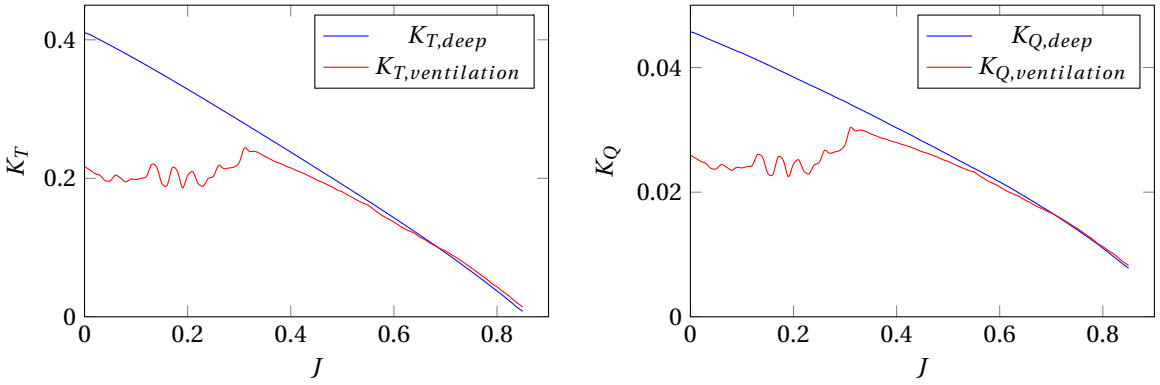

Figure C.16: Run 16: I=0.09[-], N=684[rpm]

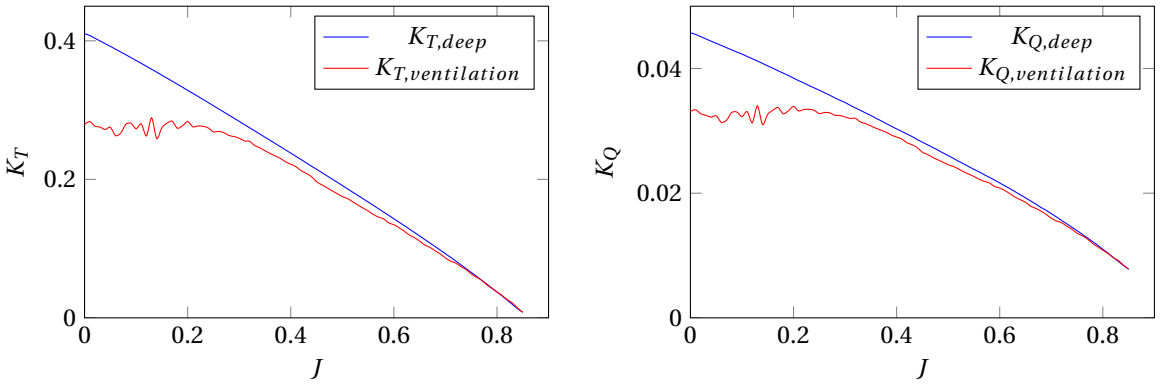

Figure C.17: Run 17: I=0.084[-], N=524[rpm]

D

Numerical results

D.1. List of computations for ventilating actuator disk

Serie	T	h_{tip}	v_a	r	g	ρ	I	C_T	σ_V	Fr_D	$\sigma_V IFr_D$	β
Regular	481	0.05	1.7	0.125	9.81	998	0.20	7.0	0.05	1.07	0.011	91.8%
Regular	721	0.075	2.1	0.125	9.81	998	0.30	7.0	0.05	1.31	0.020	97.5%
Regular	481	0.05	1.4	0.125	9.81	998	0.20	10.0	0.05	0.89	0.009	89.0%
Regular	721	0.075	1.7	0.125	9.81	998	0.30	10.0	0.05	1.10	0.016	94.7%
Regular	240	0.05	1.2	0.125	9.81	998	0.20	7.0	0.1	0.76	0.015	94.6%
Regular	360	0.075	1.4	0.125	9.81	998	0.30	7.0	0.1	0.93	0.028	98.8%
Regular	240	0.05	1.0	0.125	9.81	998	0.20	10.0	0.1	0.63	0.013	93.0%
Regular	360	0.075	1.2	0.125	9.81	998	0.30	10.0	0.1	0.77	0.023	97.5%
Regular	160	0.05	1.0	0.125	9.81	998	0.20	7.0	0.15	0.62	0.019	96.6%
Regular	240	0.075	1.2	0.125	9.81	998	0.30	7.0	0.15	0.76	0.034	99.7%
Regular	160	0.05	0.8	0.125	9.81	998	0.20	10.0	0.15	0.52	0.015	93.9%
Regular	240	0.075	1.0	0.125	9.81	998	0.30	10.0	0.15	0.63	0.028	99.2%
D	308	0.05	1.4	**0.1**	9.81	998	0.25	10.0	0.05	1.00	0.012	91.7%
D	692	0.05	1.4	**0.15**	9.81	998	0.17	10.0	0.05	0.82	0.007	88.0%
D	154	0.05	1.2	**0.1**	9.81	998	0.25	7.0	0.1	0.85	0.021	96.7%
D	346	0.05	1.2	**0.15**	9.81	998	0.17	7.0	0.1	0.69	0.012	93.6%
D	154	0.05	1.0	**0.1**	9.81	998	0.25	10.0	0.1	0.71	0.018	95.2%
D	346	0.05	1.0	**0.15**	9.81	998	0.17	10.0	0.1	0.58	0.010	91.5%
ρ, g	120	0.05	0.7	0.125	**4.905**	998	0.20	10.0	0.1	0.63	0.013	92.9%
ρ, g	180	0.05	1.0	0.125	9.81	**750**	0.20	10.0	0.1	0.63	0.013	93.0%
ρ, g	180	0.075	0.9	0.125	**4.905**	998	0.30	10.0	0.1	0.77	0.023	97.8%
ρ, g	271	0.075	1.2	0.125	9.81	**750**	0.30	10.0	0.1	0.77	0.023	97.5%
$D, C_T = 14$	125	0.04	0.75	**0.1**	9.81	998	0.20	14.0	0.10	0.54	0.01	89.6 %
$D, C_T = 14$	195	0.04	0.94	**0.1**	9.81	998	0.20	14.0	0.06	0.67	0.01	87.8 %
$D, C_T = 14$	125	0.05	0.60	0.125	9.81	998	0.20	14.0	0.19	0.38	0.01	96.7 %
$D, C_T = 14$	195	0.05	0.75	0.125	9.81	998	0.20	14.0	0.12	0.48	0.01	93.3 %
$D, C_T = 14$	281	0.05	0.90	0.125	9.81	998	0.20	14.0	0.09	0.57	0.01	89.9 %
$D, C_T = 14$	281	0.06	0.75	**0.15**	9.81	998	0.20	14.0	0.15	0.44	0.01	95.6 %
$D, C_T = 14$	195	0.06	0.62	**0.15**	9.81	998	0.20	14.0	0.21	0.36	0.02	97.4 %
$D, C_T = 14$	195	0.05	0.62	**0.15**	9.81	998	0.17	14.0	0.18	0.36	0.01	96.0 %

D.2. Numerical Settings

Category	Entry	Value
Timeloop	Solution scheme	IMPLICIT-THREE-TIME-LEVEL
	Timestep	corresponding to 0.5°
Outerloop	Max iterations	100
	Convergence Tolerance	1.00E-05
Boundaries	Walls	BCWall
	Top+Bottom	BCPressure
	Inflow	BCInflow
	Outflow	BCOutflow
	Propeller Blades	BCWall
Materials	Water Dynamic Viscosity	1.00E-03
	Water Density	1002.1
	Air Dynamic Viscosity	1.82E-05
	Air Density	1.118
Grids	MoveGridMethod	MVG
	Grids Interpolation	Nearest cell (zeroth order)
	InterfaceType	Dynamic
	HaloType	HALO-1
UserCode		shipWavePattern by B. Schuiling
Mass-Moment Solver		Segregated Fresco
Momentum eq.	Solver	GMRES
	Preconditioner	BJACOBI
	Convergence Tolerance	1.00E-03
	Max iterations	400
	Explicit relaxation	0.15
	Implicit relaxation	0.20/0.80/100
	Convective Flux Discretisation	Harmonic
	Gradient Calculator	Gauss
	Residual Normalisation	Parnassos-like
	Velocity Initialization	Earthfixed inflow velocity
Pressure eq.	Solver	PETSC-CG
	Preconditioner	BJACOBI
	Convergence Tolerance	1.00E-02
	Max iterations	500
	Explicit relaxation	0.075
	Implicit relaxation	none
	Residual Normalisation	Parnassos-like
Free Surface eq.	Solver	PETSC-GMRES
	Preconditioner	BJACOBI
	Convergence Tolerance	1.00E-02
	Max iterations	500
	Explicit relaxation	0.2
	Implicit relaxation	0.9/0.9/100
	Convective Flux Discretisation	REFRICS
	Gradient Calculator	Gauss
	Residual Normalisation	Parnassos-like

Category	Entry	Value
Turbulence eq.	Solver	PETSC-GMRES
	Preconditioner	BJACOBI
	Convergence Tolerance	1.00E-03
	Max iterations	300
	Explicit relaxation	0.15
	Implicit relaxation	0.20/0.80/100
	Relaxation Eddy Viscosity	0.2
	Convective Flux Discretisation	Harmonic
	Eccentricity Correction	true
	Residual Normalisation	Parnassos-like
	TurbIntensity Initialization	1.00E-02
	Eddy Viscosity Initialization	1
Developer options	faceInterpolation-scheme	INVERSEDISTANCEPOINT
	faceInterpolation-applyMassFluxEccentricityCorrection	true
	pwi-approxInvMomMatnoDT	false
	gradients-limiter	BARTH-JESPERSON
	turbulence-applyOmegaLimiter	true

D.3. Iterative convergence

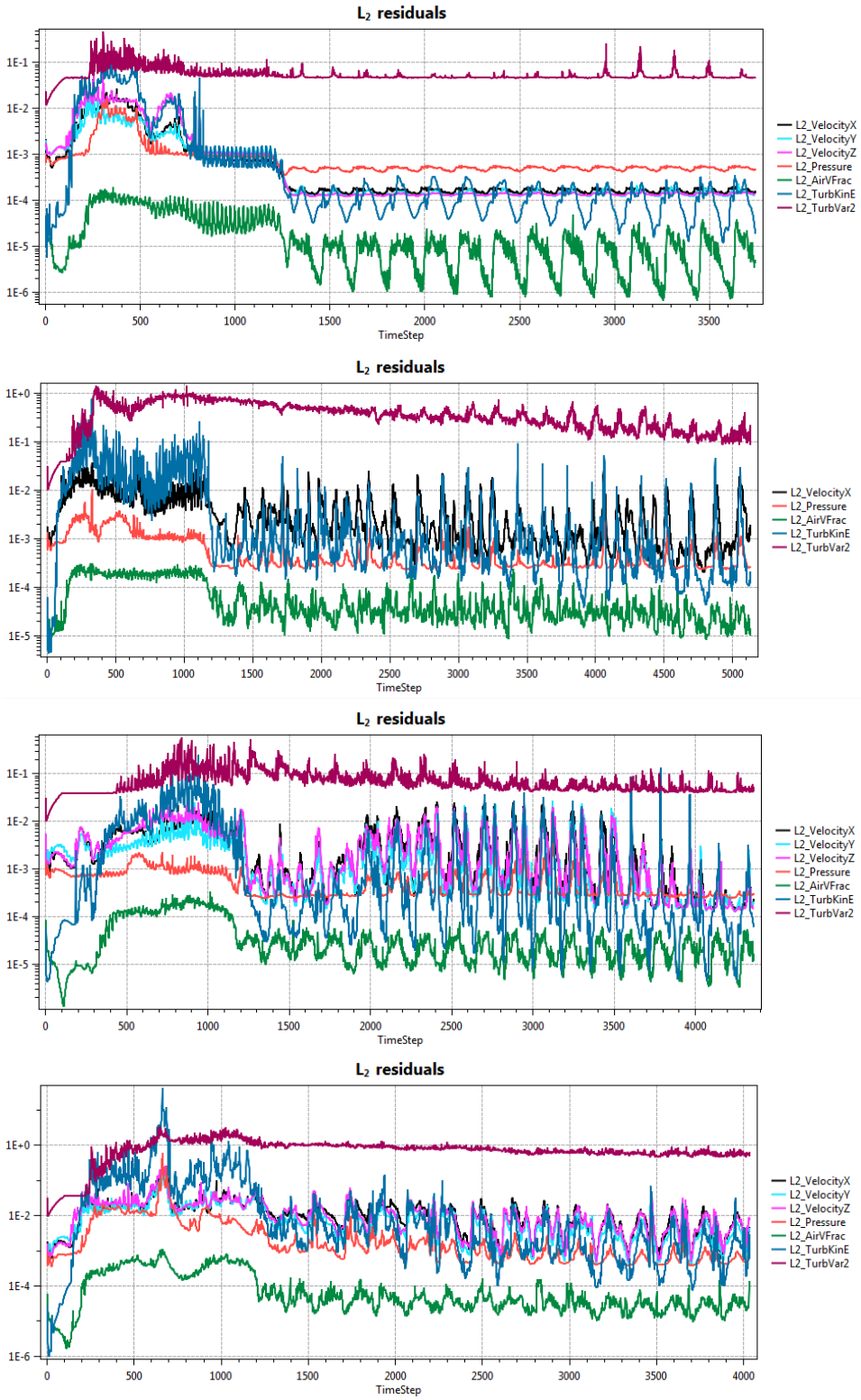

Figure D.1: L_2-residuals of $I = 0.15, J = 0.2, I = 0.084, J = 0.2, I = 0.084, J = 0.1, I = 0.090, J = 0.1$

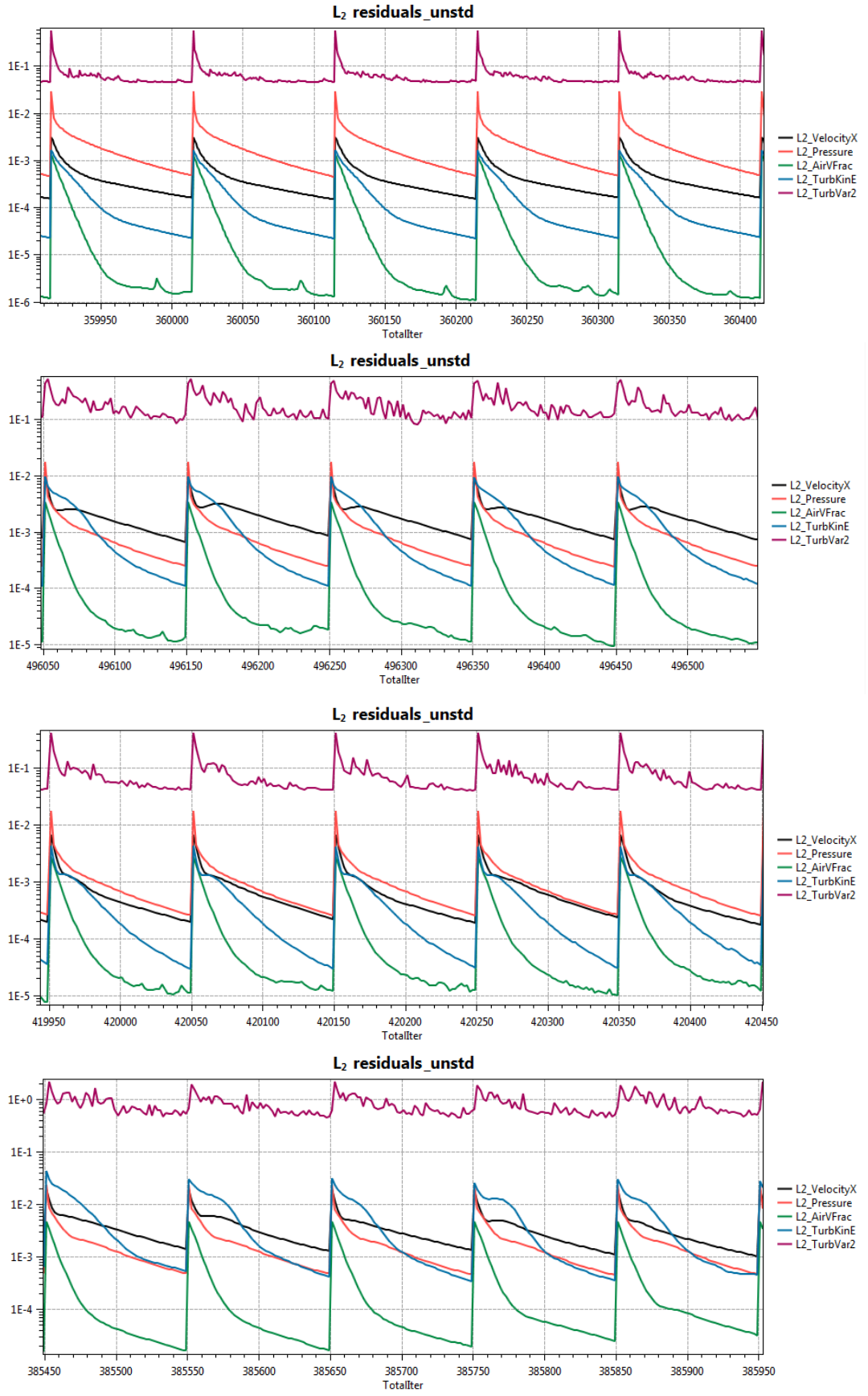

Figure D.2: Unsteady L_2-residuals of $I = 0.15$, $J = 0.2$,$I = 0.084$, $J = 0.2$,$I = 0.084$, $J = 0.1$,$I = 0.090$, $J = 0.1$